Indoor Radio-Wave Behavior at 850 and 1900 MHz with Electromagnetic Compatibility Applications in Hospitals: An Experimental, Theoretical, Statistical and Morphological Characterization

Donald P. Davis

Department of Electrical and Computer Engineering

McGill University, Montreal

October 2003

A thesis submitted to the Faculty of Graduate Studies and Research in partial fulfillment of the requirements for the degree of Doctorate in Philosophy in Electrical Engineering

© Donald Davis 2003

Library and Archives Canada

Published Heritage Branch

395 Wellington Street
Ottawa ON K1A 0N4
Canada

Bibliothèque et Archives Canada

Direction du Patrimoine de l'édition

395, rue Wellington
Ottawa ON K1A 0N4
Canada

Your file Votre référence
ISBN: 0-612-98234-3
Our file Notre référence
ISBN: 0-612-98234-3

NOTICE:
The author has granted a non-exclusive license allowing Library and Archives Canada to reproduce, publish, archive, preserve, conserve, communicate to the public by telecommunication or on the Internet, loan, distribute and sell theses worldwide, for commercial or non-commercial purposes, in microform, paper, electronic and/or any other formats.

The author retains copyright ownership and moral rights in this thesis. Neither the thesis nor substantial extracts from it may be printed or otherwise reproduced without the author's permission.

AVIS:
L'auteur a accordé une licence non exclusive permettant à la Bibliothèque et Archives Canada de reproduire, publier, archiver, sauvegarder, conserver, transmettre au public par télécommunication ou par l'Internet, prêter, distribuer et vendre des thèses partout dans le monde, à des fins commerciales ou autres, sur support microforme, papier, électronique et/ou autres formats.

L'auteur conserve la propriété du droit d'auteur et des droits moraux qui protège cette thèse. Ni la thèse ni des extraits substantiels de celle-ci ne doivent être imprimés ou autrement reproduits sans son autorisation.

In compliance with the Canadian Privacy Act some supporting forms may have been removed from this thesis.

While these forms may be included in the document page count, their removal does not represent any loss of content from the thesis.

Conformément à la loi canadienne sur la protection de la vie privée, quelques formulaires secondaires ont été enlevés de cette thèse.

Bien que ces formulaires aient inclus dans la pagination, il n'y aura aucun contenu manquant.

Canada

Abstract

This thesis aimed to provide a knowledge base and methodologies to help minimize electromagnetic interference (EMI) in healthcare. Two methods were developed, for the first time, to quantify EMI risk due to radio frequency (RF) sources in hospitals. The first method used contour maps and cumulative distributions of field strength to compute the risk of EMI from an RF source of known power operating near a medical device of known immunity. The second method, "minimal separation with risk", used power law models and cumulative distributions of the residuals from such models to compute the risk of EMI from an RF source of known power operating near a medical device of known immunity, both situated in a known electromagnetic environment.

Field structures within a hospital were extensively characterized using straight-line trajectories or planar surfaces, sampled individually or in 3-dimensional arrays. Data was obtained both experimentally (850 and 1900 MHz) and through simulations (850, 1900 and 2400 MHz). Both the structure (morphology) and the statistics of fields were characterized. Field behavior was characterized in corridors (e.g. fields fell more rapidly near walls, but remained unexpectedly constant near the floor) and in clay-block rooms (e.g. extensive standing wave patterns).

The methods permitted computation of the actual risk of EMI for a given hospital electromagnetic compatibility (EMC) policy in a hospital environment, rather than the safe-unsafe recommendations commonly recommended, even in medical device standards. This provides a more realistic assessment of the effectiveness of a particular hospital EMC policy.

Finally, a theoretical development employing scalar theory approach led to an approximate estimate of the average electric field in a room. The relationship between this average field strength and the room's average reflection coefficient provided an approximate gauge useful for rapid preliminary EMI risk assessment within a room.

Résumé

Cette thèse se trait du problem de l'interference electromagnetique (EMI) dans l' environment hospitalier en untilizant deux methodes nouvelles pour quantifier le niveau de risque produits par les sources des frequences radio (RF). La première methode utilize une modele exponentiel et la distribution cumulatif de la difference entre les valeurs actuelles des champs electriques et les quantities produits par la modele pour mieux estimer la risque d'interference et la suceptibilité à une distance fixe d'une source RF. La deuxième methode utilize une carte avec courbes de niveau des champs electriques et la distribution des valeurs des champs electriques pour estimer la risque d'interference sur un plan horizontal.

Cette thèse a examiné la structure des champs electriques dans une edifice en plus particulier les champs dans les couloirs et chambres. Les detailles sur les trajectoires, plans et les structures 3-D des champs electriques etait obtenu pars les measurations et les simulations numeriques. La structure (Morphologie) et les resultants de la grande nombre statistiques de l'investigation etait evalué et après cette evaluation les risques de l'interference était estimé par la probibilité de depasser l'immunité d'une instrument medicale.

Les methods traditionelles utilize une estimation binaire pour la risque, plutôt les deux methods utilize dans cette thèse donne la valeur actuelle de la risque d'interference. Les deux nouvelles methods offre des evaluations plus realiste concernant l'efficacité des politiques de compabilite electromagnetique (EMC) que les methods anciens méthodes. Il a aussi devlopé un paramètre unique pour mieux décriver la moyenne des valeures des champs electriques dans les chambres. Cette paramètre est appliquer pour faire une estimation préliminàire de la risque d'interference dans un chambre.

Acknowledgments

The author would like to express sincere gratitude to Professors T.J.F. Pavlasek, B.N. Segal, C.W. Trueman for their support, guidance and encouragement. Without their supervision, this work would not have been possible.

Thanks are also due to the students who assisted in the measurements performed during the course of this thesis: R. Calzadilla, A. Cinquinno, J.P. Gaspard, K. Hoege, P. Lala, R. Mastrocola, D. Martucci, A. Ngoly, J. Romanski, and G. Tait all of whom put a great deal of time and effort in the task of acquiring field strength data used in this thesis.

Thanks are due to Dr. C.W. Trueman for the large amount of time spent developing the GO_3D code used for simulations in this thesis and for the time spent instructing the author in the use of the code.

Thanks are due to D. Chu whose expertise in robotics allowed for the rapid and successful development of the robotic measurement system from concept to working reality.

Thanks are due to the department heads and staff of the SMBD Jewish General Hospital for allowing the measurements to be performed within the hospital, and for facilitating the work whenever possible.

The support of this work by grants from Bell Mobility, Rodgers Cantel Inc, and NSERC is gratefully acknowledged.

Table of Contents

List of Figures

List of Tables

Chapter 1

Introduction

1.1 Wireless Communication and EMI Risk

The incorporation of wireless technology into medical informatics, the provision of medical information to medical professionals, has the potential to improve healthcare by providing timely access to complete and accurate patient information at all stages of the healthcare delivery process. It has been suggested that the usage of medical informatics can reduce the risk of patient injury or death due to medical errors [30, 51, 74, 93], particularly when wireless technology is used [76, 77].

Wireless technology uses electromagnetic fields to link various devices. In general, the stronger the fields, the better the communication. However, strong electromagnetic fields may cause electromagnetic interference (EMI) with the operation of other devices, such as medical care equipment [60, 62, 73]. Such malfunctions may be non-life threatening, such as a warning light going on incorrectly, or may be as serious as a critical care device malfunctioning, such as an infusion pump not providing correct dosages of medication. A large variety of medical devices that have been affected by EMI, including apnea monitors, anesthetic gas monitors, powered wheelchairs and scooters, to name a few [78, 81]. An EMI incident is a specific case of a device malfunction that endangers a patient.

Although medical informatics potentially improves patient care, the potential for *EMI incidents*, in a wireless environment could offset the benefits. Hospitals and others

would likely be liable for negligence if an EMI-related malfunction caused injury or death [85].

At present, many hospitals have banned wireless technology such as cellular telephones. The ban of wireless technology eliminates the potential benefits of wireless medical informatics, and is often difficult to enforce. Visitors and even staff may bring active cellular phones within hospitals and forget to turn the phones off.

To realize the benefits of wireless informatics in healthcare, it must be possible to design a wireless network meeting conflicting requirements: sufficiently strong fields are required for good communication, but the fields must be weak enough so that the normal operation of medical equipment is not compromised [75, 85]. It may be possible to fulfill these dual requirements if the electromagnetic environment in hospitals is sufficiently well understood. This understanding is achieved through validated models of field behavior within a hospital and is the principle subject of the thesis.

The *immunity level* of a particular medical device is the maximum electric field strength that the device can be exposed to before it malfunctions. Electromagnetic field strength above the immunity level may lead to interference and EMI incidents. Minimum immunity levels for medical devices may be specified by the appropriate standard in the country of manufacture or in the country where the device is used. In the United States, the International Electrotechnical Commission specifies medical device immunity levels in the IEC60601-1-2 standard. These are 10 V/m from 80 MHz to 2.5 GHz. Non life support devices may have immunity levels of 3 V/m for frequencies up to 2.5 GHz [46]. Devices manufactured before these standards came into effect, or devices intended for nations with less conservative EMI policies, may

have even lower immunity levels. Note that these are voluntary standards and are not embodied in legislation.

The minimum field strengths for adequate communication in a digital wireless network depends on the bit error rate that can be tolerated, which in turn depends on the noise present in the electromagnetic environment. For example, a device using the Bluetooth wireless communication protocols requires a receiver sensitivity of –70 dBm with a bit error rate (BER) of 0.1% to be effective [88]. The field strength must be greater than the noise floor in order for the information to be transmitted. The absolute level of the field required for a successful communication link is dependant on both the technology used and the environment where the system operates [47, 52, 67].

Any institution that intends to use wireless medical informatics must adopt an electromagnetic compatibility (EMC) policy that insures the operation of the wireless system will have minimal potential EMI incidents. An electromagnetic compatibility policy (EMC policy) is a set of rules that govern the usage of electronic equipment in order to minimize the risk of EMI during normal operation of the equipment [58]. At present, there is no single widely accepted EMC policy for medical institutions to use. There are some guidelines and recommendations to minimize EMI risk, including recommendations from McGill [73], AAMI [1], the present medical device immunity standard, IEC 60601-1-2 [46] and the ANSI C-63.18 standard [2]. These lead to policies that involve controlling the maximum field strength permissible around susceptible medical devices. Although new medical devices are required to have an immunity of 10 V/m, many older devices have immunities of 3 V/m, or are unknown. Medical equipment tends to be in use for many, perhaps 10 to 15, years. Developing

an EMC policy entails a strategy for managing the EMI risk. The next section will discuss one possible EMI risk management strategy.

1.2 Strategy for EMI Risk Management

The strategy for minimizing EMI risk due to radiated fields suggested by the IEC 60601-1-2 standard is called *minimal separation* (MS). Minimal separation proposes to keep radiating RF sources and susceptible devices separated by a sufficient minimum distance so that the field strength at the susceptible device is less than its immunity level. This minimum distance from the radiating source is computed assuming that the field strength attenuates with distance in the same manner as a spherical wave in free space. An isotropic source radiating in free space has field strength E that is proportional to the square root of the power P of the source and varies inversely with distance between the source and the observer r [61].

$$E = \sqrt{\frac{\eta P}{2\pi}}\left(\frac{1}{r}\right) \qquad \ldots(1\text{-}1)$$

Where η is the intrinsic impedance of free space.

Minimal separations used in the IEC standard assume that in the indoor environment the field strength decreases in the same manner as in free space, proportional to the inverse of the distance between the source and the observer. However, the IEC standard uses a safety factor of 10/3, this factor helps to account for the reflections from walls and other surfaces that may reinforce the radiated field.

The minimal separation is calculated in the IEC standard using

$$MS = \left(\frac{10}{3}\right)\left(\frac{1}{E_I}\right)\sqrt{\frac{\eta P}{2\pi}} \qquad \ldots(1\text{-}2)$$

Where E_I is the immunity level of the susceptible device medical device [46].

For example, a radiating source of power P=600 mW source and a medical device with an immunity E_I =3 V/m must be kept 6.67 meters apart. The minimal separation for free space, obtained by removing the correction factor of $10/3$ from equation 1-2, is 2 meters.

The IEC standard assumes that in an indoor environment, the field strengths for locations further away than the MS distance are uniformly lower than the immunity level of the susceptible device [46]. This assumption implies that if the MS strategy were properly applied, the risk of EMI due to radiated emissions would be zero.

Clearly, the assumption that electromagnetic fields in an indoor environment behave in a manner similar to free space is often not valid. Indoor fields typically have complex interference patterns due to interactions between the fields and the different structural elements within the building. It is often assumed that the fields arriving at an observer have random phase, giving rise to Rayleigh or Rician probability distributed fading [67, 68]. A typical observer sees a *ray* directly from the source, for LOS, and many reflected rays from walls, floor and ceiling. A ray is a piece-wise straight-line path that links two points. The field associated with a particular ray depends on the total distance along the ray path from the source to the observer, and on the reflection coefficients of each surface that the ray path intersects. [7]. The

structure of the field as the observer moves depends on both the amplitude and phase of the fields associated with all the rays [5, 57, 86].

Many authors have investigated the behavior of electric fields in different urban environments such as outdoor [6, 8, 29, 66, 67, 70,90], indoor [14, 15, 28, 43, 44, 71, 72], and tunnels [42, 45, 92]. The consensus is that the average field strength generally has a slower rate of decrease than in free space when there is *line of sight* (LOS) path, but a higher rate of decrease in the field strength for *non-line of sight* (NLOS) paths for both outdoor urban settings and inside buildings or tunnels.

In general, these environments involve interference patterns where the trend or *average field* drops slowly with distance (slow varying) while the *local field* varies rapidly over distances small compared to the wavelength (fast varying). Estimates of the field strength using free space propagation models, which do not model the variability of the field due to the interference patterns or the different rate of field attenuation, may not accurately describe the behavior of urban or indoor fields. Hence the MS criterion, although simple, may not be sufficiently accurate for EMI design of wireless networks.

Measurements of outdoor fields indicated that the slow varying in urban centers varied significantly. Some locations (LOS) had attenuations less than free space, due to guiding of waves by buildings, while other locations (NLOS) had much higher attenuation of field strength, due to fields being blocked or absorbed by buildings. The field strength for LOS locations decreased at rates ranging from close to free space to nearly 65% of the free space rate. By contrast, the field strength for NLOS locations decreased at rates up to 3 times higher than free space. The fast varying was

modeled using Rayleigh or Rician distributions. The Rayleigh distribution is used for NLOS fast varying [6, 8, 29, 65, 79, 92].

Simulations of outdoor fields generally agreed with the findings of the measurements. Slow varying tended to have less attenuation for LOS paths, while the NLOS tended to have higher rates of attenuation. The LOS attenuation rates were comparable with the measured rates, but the NLOS rates were in some cases much higher. This was due to the shadowing effects of buildings or natural obstructions such as trees dominating some locations [8, 48, 53, 70, 84, 90].

Measurements performed in tunnels [31, 54, 64, 92] indicated that the field strength decreased at lower rates than free space. In many cases, the rate of decrease was approximately 70% of the free space rate. However there was significant variability, fast varying, present in tunnels. Measurements in buildings [28, 42, 50, 67, 82] indicated for LOS the field strength attenuated at a lower rate than free space while for NLOS the rate at which field strength attenuated was much higher than free space, up to three times greater than the free space rate. Studies that included penetration through floors and walls, provided information about the amount of field strength lost when an electromagnetic wave crosses a material boundary. The average drop in field strength is material and frequency dependent, but drops over 60 dB are not uncommon for concrete structures [15, 42, 44, 89] with higher drops occurring at frequencies over 20 GHz [83, 91]. The fast varying behavior was treated in the same manner as the urban measurements. The variability of indoor and tunnel environments was measured on smaller scales than the urban environment and so direct comparison is problematical.

Simulations performed on tunnel and building models provided comparable results for slow varying analysis. The simulated fast varying characteristics were close to the measurements. The complexity of the models was limited to features that were larger than a wavelength [26, 43, 45, 72].

The process of designing appropriate strategies to accomplish the dual goals of good communication coverage, field strength high enough for good signal reception over a hospital floor, but fields low enough that there is no risk of EMI, requires that the indoor electromagnetic environment be well understood.

1.3 Measuring the Hospital Electromagnetic Environment

By measuring indoor fields, practical information about the actual field strengths due to RF sources is obtained. This is a key element in understanding the indoor electromagnetic environment. The degree of accuracy and precision required dictates the amount of data and the measurement process used. When a relatively small number of data points are required, point measurements may be performed at a few locations within a building. These measurements typically use both LOS and NLOS locations to obtain data on field strength. Point measurements are used to investigate general behavior of the field within a region. For this study, more detailed measurement approaches were used: *trajectory*, *planar surface* and *volume measurements*. Trajectory measurements obtain the field strength as a function of distance along a path located within a building. Trajectory measurements may be LOS, NLOS or a combination of the two. Unlike point measurements, trajectory measurements allow for more detailed studies of the relationship between the field strength and distance from the source [20, 67, 88]. Planar surface measurements are typically performed on a grid at a constant height above a floor. The grid is composed

of a series of parallel trajectory measurements. While planar surface measurements provide detailed information about the behavior of fields within the measurement region, these measurements require a large commitment of experimental resources and time when compared to the point and trajectory measurements. The most detailed and expensive, in terms of experimental resources and time, measurements are volume measurements. Performing a series of planar surface measurements at different heights and then stacking the resultant data may approximate volume measurements.

This thesis presents many measured field strengths for trajectories, planar surfaces and some preliminary volume measurements. The source was placed in a fixed location for each series of measurements. A robotic measurement system was developed in order to perform a large number of measurements in an efficient and repeatable manner. The robot system carried the receiving antenna along trajectories allowing the field data to be related to position along the trajectory [22]. The electric field behavior as a function of distance from the source as well as slow and fast varying information was obtained from the above measurements. While some authors investigated polarization sensitivity, [32, 63], only the vertical components of the field were measured and used in this thesis.

The measurements were complemented by numerical simulations that duplicated and extended the investigation of indoor fields begun by the measurements.

1.4 Computer Simulation of Fields Within Hospitals

Numerical simulation of the indoor electromagnetic environment provides another avenue for understanding the behavior of fields within a hospital. The most popular techniques are based on *Geometrical Optics* (GO) or *Geometrical Theory of Diffraction* (GTD) [5].

Geometrical optics assumes that the wavelength of the electromagnetic wave is small when compared to the dimensions of the objects being modeled and that the field travels along straight-line paths called "rays" that obey Snell's laws of reflection and refraction. *Ray tracing* is the technique that determines the various paths that link the source and the observer. There can be direct or LOS and paths due to reflection from surfaces such as walls and floor and ceilings. Reflected paths are composed of several straight-line segments. Indoor environments often have many possible paths that link the source and observer. The field associated with each ray has a polarization, magnitude and phase component. The GO field is computed by summing the field associated with all the rays arriving at an observer accounting for polarization, magnitude and phase information [57]. However, shadowing causes discontinuities in the GO field.

The geometrical theory of diffraction incorporates diffraction from edges such as the corners of walls into the GO model to compensate for the effects of shadowing. The sudden appearance or disappearance of a ray is balanced by a diffraction coefficient. This smoothes out the field discontinuities due to shadowing and provides a mechanism for fields to propagate into deep shadow zones of the GO field [5, 34, 57].

Simulations based on GO and GTD models have been used to investigate electric field behavior for various environments. Routines using either *shooting bouncing rays* (SBR) [13,14,48] or *images* [8, 31, 43, 45, 86] were the most common forms of the GO and GTD analysis. Shooting bouncing rays involves launching a large number of rays out from the source and summing the contributions of rays that pass within a region around the source. Images are equivalent sources used to generate reflected or refracted rays from walls. The source and image rays are summed up at the source to compute the total field. Two and three-dimensional models were used in the field strength simulations within urban and indoor environments. For urban environments, two-dimensional models were able to provide data close to the measurements. Indoor simulations had better agreement with measurements when three-dimensional models were used. These simulations are typically used to obtain information relevant to communication coverage within a particular environment, such as path loss, statistics of varying and propagation time information.

While the GO and GTD based modeling techniques are the most popular, modeling using waveguide principles for analysis [38, 39 42, 56] as well as alternate numerical techniques such as finite difference (FD) and finite element (FE) [10, 12, 41, 64, 70] have also been used to estimate field behavior in certain cases. Typically structures with highly reflective boundaries, such as metallic walled chambers or corridors, made the alternate techniques attractive in modeling fields. Overall, the GO and GTD based techniques provide high computational efficiency for urban and indoor modeling for frequencies over 700 MHz.

The large amount of field data obtained from both the measurements and the simulations can be difficult to interpret, hence the need for heuristic models to summarize the indoor field behavior in a simple way.

1.5 Heuristic Characterization of the Hospital Electromagnetic Environment

The minimal separation criterion is based on a heuristic characterization of indoor propagation assuming that the field strength decreases inversely with distance, and that wall reflections may be accounted for by multiplying the free space field by a constant. For example, the IEC standard uses a safety factor of $10/3$ as the constant.

A general heuristic model has two components: 1) A *power law model* to describe the field strength as a function of distance from the source and 2) a *statistical model* to describe the variability of the field [47, 79]. Equation 1-3 shows a common power law model of field strength E as a function of distance from the source r.

$$E = \frac{E_o}{r^n} \qquad \ldots(1\text{-}3)$$

The field strength varies inversely with distance at a rate determined by the path *loss exponent* (n). The path loss exponent is obtained by performing linear regression on the field strength data obtained by either measurement or simulation. The path loss exponent may vary with frequency and environment but is typically $n \leq 1$ for LOS cases and $n \geq 1$ greater than 1 for NLOS cases, for free space n=1. The reference field strength E_o is proportional to the source power [52, 67, 80].

The power law model of equation 1-3 replaces the slow and fast varying behavior of the field with a uniform decline. The amount of variation of the field strength depends on the environment and frequency of the source. A location with a strong interference

pattern would produce large variability in the field strength. The difference between the actual field strength data and the power law model is called the *residual*. The statistics of the residual are a measure of the variability of the field. A heuristic model that describes both the field strength as a function of distance from the source and the variability of the field is shown in equation 1-4 [67]. The structure or "morphology" of the field strength is approximately modeled using this relationship.

$$E(r) = \frac{E_o}{r^n} + X(\mu, \sigma) \qquad \text{... (1-4)}$$

The electric field strength E varies inversely as r^n. The field strength varies about the power law model by an amount X, a random variable with mean μ and variance σ [67]. The residual, X, is difference between the raw electric field data E and the trend relationship in equation 1-3. The residual relationship as a function of distance, r, separating the source and the observer is given by equation 1-5.

$$X(r) = E(r) - \frac{E_o}{r^n} \qquad \text{...(1-5)}$$

Subdividing the full range of residual values into a discrete number of sub-ranges approximates the probability distribution of the residual. Each sub-range, (or bin), contains a portion of the total number of residual values. The number of entries in each bin approximates the probability associated with that range of residual values. The residuals are sorted in ascending order and each entry is given a probability p_k, where $p_k = \frac{M_k}{M}$, where M_k is the number of residual values occurring within a small range and M is the total number of residual values used in the distribution [27]. The

bin values are sorted in ascending order. The associated probability values p_k are used to compute the cumulative distribution from the probability distribution of the sorted residuals using 1-6.

$$CDF(E_k) = \sum_{n=1}^{k} p_k \qquad \ldots (1\text{-}6)$$

The distribution indicates the probability of encountering a residual equal to or less than the value E_k. The same process may be applied to the distribution of field strengths instead of residuals.

This treatment of the variability is not compatible with the power law model of field strength. The models based on data obtained from either point measurements or trajectory measurements, for indoor environments usually have higher variability and smaller n values than models of the outdoor environment [52, 67, 80].

In the indoor environment, there is often no LOS path between the source and the observer because a wall blocks the path. A heuristic approach is to use *insertion loss* to account for drops in field strength when the path penetrates a wall. The insertion loss, typically given in dB, provides an average value of the drop in field strength associated with the transmission of the wave through a material boundary. These are typically frequency and material dependent. As the insertion loss is an average value, it ignores angle dependence of transmission and the true transmitted field may vary significantly from the average value.

1.6 Objectives of this Study and Rationale

At present, there is no quantitative measure of EMI risk available for medical institutions to use in developing an EMC policy. The risk of EMI must be quantified so that practical, meaningful assessments of the effectiveness of different EMC procedures become possible. A principle objective of this thesis is to quantify EMI risk.

The basis for developing an effective EMC policy is a good understanding of the behavior of the electromagnetic fields produced by wireless devices in a hospital environment. Therefore this thesis will start with an extensive survey of the field strengths in corridors and rooms by measurements. The survey will include trajectory measurements, planar surface measurements and volume measurements.

The next stage will be to perform simulations that can duplicate the measured results. The simulations must be able to reproduce the morphology of the measurements reasonably. The simulated data must have good agreement with the measured data, as this is necessary to have a good understanding of the indoor propagation of fields. Once the ability to reproduce the morphology and good agreement is achieved, simulations will be performed to expand the investigation of indoor field behavior to configurations not covered by the measurement survey.

Both the measurements and simulations will aim to develop heuristic models of indoor propagation. Field strengths of the heuristic models will be obtained from regression on the measured data and the variability of the fields is obtained from the residuals. The parameters of the heuristic models will be used to compare the results

of the indoor measurement and simulation surveys of: trajectory, planar surface and volume field data.

The minimal separation criterion uses a pass-fail assessment of the risk of EMI. If the minimal separation is applied, the risk of EMI is intended to be zero according to the IEC standard recommendations. This simplistic model, based on a power law model in free space, is not sufficient for accurate assessments of the risk of EMI in different environments and is not practical when comparing different policies or designing wireless networks in hospitals. This thesis aims to develop a better measure of EMI risk with: the concept of minimal separation with risk (MSR), where the risk of EMI is quantified based on the variability of the data as well as the power law model, thereby providing a more realistic assessment of the probability of an EMI incident [20,25].

The heuristic models will use both the power law and the variability of the field, equation 1-4, to quantify the risk of EMI, based on known immunity levels of medical devices and known source power. This will be done by computing the probability of exceeding a given immunity level at a known distance from the source. This novel technique provides for the first time a quantifiable measure of the probability of an EMI incident based on distance from the source. MSR will provide a tool for the design of wireless networks that includes coverage information as well as EMI risk information.

Overall, this thesis aims to build a framework for a better understanding of the hospital electromagnetic environment by quantifying the EMI risk. The techniques in this thesis will provide tools for the development of an EMC policy for wireless

networks in hospitals by allowing the quantitative comparison of different policies and implementations in terms of EMI risk.

Figure 1.1 shows a schematic representation of the treatment of the data and the steps to be used to characterize indoor fields to obtain heuristic models and to compute the EMI risk. Trajectory data will be analyzed using power law models and distributions of the residuals of power law models and actual field strengths. Planar surface data will be plotted on contour maps to determine structure and cumulative distributions are used to characterize field strength on planar surfaces. Three-dimensional data sets will be analyzed in the same manner as planar surface data.

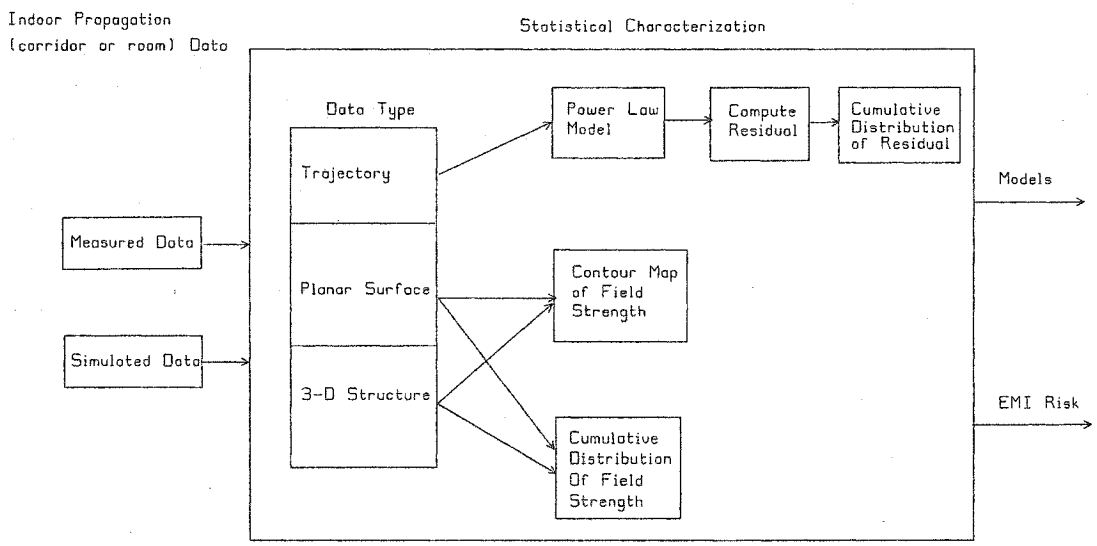

Figure 1.1 Schematic representation of treatment of data in thesis.

1.7 Thesis Organization

Chapter 2 discusses the methods used in the measurements and simulations. The chapter next discusses the heuristic modeling techniques used to characterize the data.

The chapter finishes with a discussion on the process of computing the EMI risk for different minimal separations.

Chapter 3 contains the results of the trajectory measurements performed within hospital corridors. Centerline trajectories are the first covered. The results of 850 and 1900 MHz measurements are presented and discussed. The power law parameters and variability of the field strengths are discussed along with the EMI risk assessments for different minimal separations. Next, volume measurements at 1900 MHz are presented, the behavior of the power law parameters and the variability as a function of location within the volume is discussed. The EMI risk due to various minimal separations is compared at the end of the volume measurement section. The results of the simulations for corridor centerline trajectories at 850, 1900 and 2400 MHz are presented after the measurements. The simulated and measured fields are compared using the power law and variability models and the EMI risk was assessed. After the simulated centerline trajectory data, the volume simulations are compared with the analogous measured field data using power law models and variability models. As in the previous sections, the EMI risk is computed for various minimal separations.

Chapter 4 presents the results of planar surface simulations of fields within a corridor at 850, 1900 and 2400 MHz and for three different source locations within the corridor. Unlike trajectory measurements, the structure of the field is not modeled using a power law; rather the field structure is presented using contour plots. The variability of the field strength is modeled using the distribution of the field strength rather than the distribution of the residuals. The risk of EMI using this alternate approach is presented at the end of the chapter.

Chapter 5 is concerned with the field behavior within rooms. Trajectory measurements within a room are presented first and planar surface measurements within a room are presented next. The risk of EMI for both trajectory and then planar surface data are presented at the end of the measurement section. The risk of EMI for planar surfaces is computed using the distribution of field strengths rather than the distribution of residuals. The second half of the chapter is concerned with simulated fields within a room. Simulations are used to reproduce the measured fields and the results are compared with the measurements. The EMI risk for the simulated fields is compared in the same manner as for the measured data.

Chapter 6 introduces an alternate statistical approach where the average field within a room is used as an EMI risk indicator. The average field within a room for measured and simulated fields is compared to the average field strength computed from steady state power within the room. The steady state power is computed from an average transmission coefficient based on the wall, floor and ceiling properties of the room.

Chapter 7 summarizes results and contains a discussion of relevant field behavior. The EMI risk assessments from the previous chapters are summarized and this summary is used to evaluate different EMC policies and possible network design parameters. The utility of the novel techniques and the importance of the results of the survey are summarized. The last section of the chapter contains a summary, contributions to knowledge, conclusions and suggestions for future work.

1.8 Contributions to Knowledge

One of the primary contributions of this thesis is the development of methods to quantify EMI risk within hospital corridors and rooms. This was accomplished using

two different techniques, minimal separations with risk (MSR) and from the distributions of the field strength values.

Heuristic models were developed that described the field strength, both measured and simulated, along trajectories. These models used power law models to describe the slow-varying or deterministic behavior of field strength along a path and statistical models to describe the fast-varying or variational behavior field strength along a path. These models were used to develop a novel technique for quantitative assessment of EMI risk based on the distribution of measured or simulated field strength (MSR). The second approach used the distribution of field strength values directly to compute the risk of EMI on planar surfaces rather than on trajectories.

These techniques were used to refine the present EMC guidelines suggested by the IEC standard so that the variation of indoor field strengths is included in the EMI risk assessment. By providing a numerical value for the risk of EMI in a given situation, this technique also allows for the direct comparison of the performance of different EMC policies. The novel approaches to EMI risk assessment replaces the pass/fail approach to risk of EMI with objective quantification of risk based on data.

This thesis provides an extensive measurement and simulation survey of indoor electromagnetic fields due to 850 and 1900 MHz sources. The simulation work was extended to 2400 MHz in order to investigate field behavior beyond the measurements.

The measurements produced previously unreported behavior, low nearly constant field strength, of fields near the floor of a corridor. Geometrical optics based simulations did not reproduce this behavior, but otherwise had strong agreement with measured data. This indicates that an additional level of simulation complexity beyond GO is required to reproduce this behavior. This provides information on the refinement of indoor simulations based on GO.

A "hotness criterion" was developed to assess whether the MS method is appropriate in a given room. This is an alternate approach to rigorous analysis and was developed using theoretical considerations along with multiple reasonable assumptions that characterized the "hotness" of rooms and related the average electric field to source location and wall properties, complex fields within a room were reduced to a single parameter. This parameter indicated whether the room contained strong interference patterns, which would make minimal separations less effective in reducing EMI risk. This choice was made based on how much larger the average field was above a free space datum value. While not as precise as the previous technique, the hotness criterion provides a quick "rule of thumb" approach to estimating the risk of EMI within a room.

Chapter 2

Methods

2.1 Introduction

Extensive measurements and simulations of the field strength in corridors and rooms were conducted at the Sir Mortimer B. Davis Jewish General Hospital. This chapter describes the measurement method, using an RF source at a fixed frequency and location and a receiver antenna mounted on a moving robot. The measurements were paralleled with computer simulations. This chapter summarizes the GO method used in the simulations. Examples of results for both measured and simulated data are shown. Later in the thesis, extensive measurement and simulation results are presented, obtained by methods described in this chapter.

This chapter describes the methods used to derive the reference field strength E_o and the path loss exponent n of the power law model in equation 1-4 for both the measurements and simulations. The residual of the measured or simulated field strength from a power law model is obtained using equation 1-5. The cumulative distribution, computed using equation 1-6, is used to model the variance of indoor fields.

Finally this chapter describes the methodology used throughout this thesis to assess the EMI risks, based on either the heuristic model or directly from the measured or simulated data.

2.1.1 The Hospital Environment

The hospital used in this study is a tertiary-care urban hospital. The measurements were taken in corridors and rooms, including the furnishings and equipment usually found there. Measurements were done on weekends and at night when staff and patients were absent [19]. The hospital has an old wing and a new wing, and measurements were done in both. The interior walls of the old wing are of clay-block construction while the exterior walls are of concrete block construction. The interior walls of the new wing are steel stud frames with gyp-rock facing, the exterior walls of the newer wing are of reinforced concrete with metallic vapor barriers. Measurements were made in nine corridors of the hospital, six in the old wing and three in the newer wing. The details of the corridor measurements are presented in Chapter 3. Room measurements are presented in Chapter 5.

2.1.2 Corridor Measurements

The older wing corridors used in this study were 50 meters long, 3 meters high and 2 meters wide. A schematic floor plan of a corridor is shown in figure 2.9. There were doors along the length of the corridor leading to rooms and fire exits. The interior

walls were of clay-block construction; there was a suspended foam tile ceiling 2.5 m above the reinforced concrete floor. The end walls, (located at A and B in figure 2.1), of the corridor were of glass block construction. Figure 2.1 is a plan of the corridor on the ninth floor used for some of the measurements presented in this thesis.

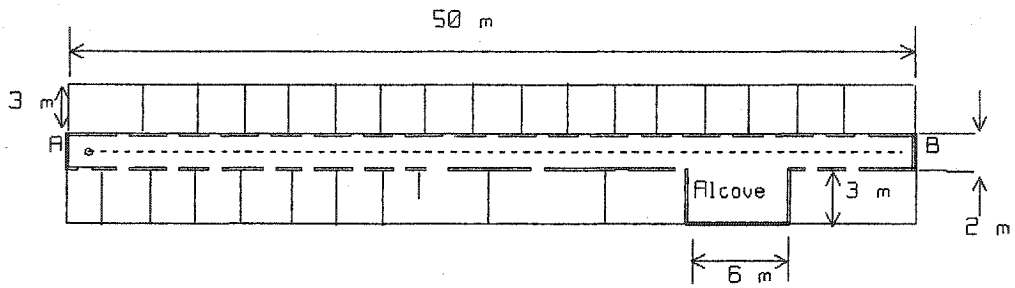

Figure 2.1 Schematic of corridor used in measurements. A and B indicate the location of the glass-block end walls, dimensions rounded in captions.

The behavior of the field propagating along the corridor will be studied by setting up a transmitter near one end of the corridor, location A in figure 2.1, and measuring field strengths in intervals along a straight line path such as the dashed line linking locations A and B. Figure 2.2 shows a typical result obtained by the methods described in section 2.2. The measurements are calibrated to 600 mW using a method discussed in section 2.2.5. The measured field strengths in the figure are called "pre-calibration data" while the "calibrated data" is representative of the field strengths used in this thesis. The calibration factor is used to show the field strength if the source radiated 600 mW without any losses.

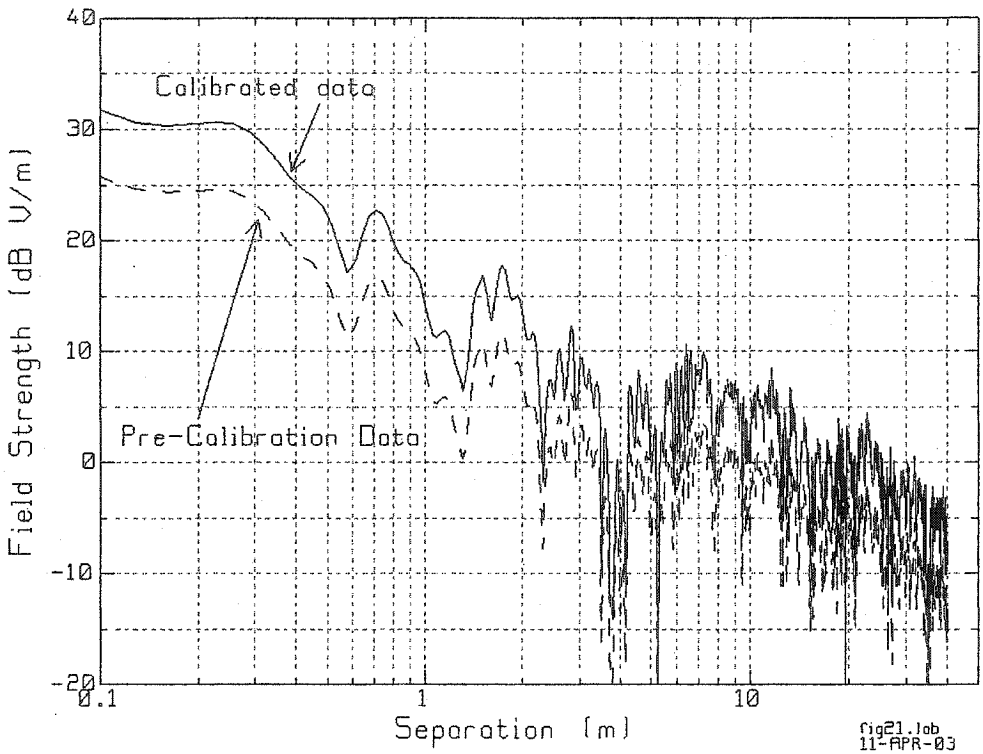

Figure 2.2 Measured field strengths before and after calibration factor applied. The source, a 0.6-watt dipole, was operating at 850 MHz.

Very near the source, 10 to 30 cm, the field strength attenuates inversely with distance from the source. From 30 to 58 cm, the field declines monotonically, slightly more rapidly than 1/distance. Further than 58 cm, the field strength attenuates less rapidly than 1/ distance. From 50 to 200 cm, the field has a structure of widely spaced nulls and peaks. Beyond 200 cm the field strength exhibits rapid variation with distance (*fast varying*) superimposed upon a gradual decline in average field strength (*slow varying*).

2.2 Measurement Methods

In order to measure the fields effectively along the 50-meter path in the corridor of figure 2.1, a robot measurement system was built. This system is described in the following section.

2.2.1 Transmitter and Receiver

The source or transmitter of the RF field for the 850 MHz measurements was a analog cellular telephone (Motorola SLF1690C) shown in figure 2.3. For the 1900 MHz measurements a RF signal generator (HP616A) connected to monopole transmit antenna, figure 2.4, was used as the source [23, 24].

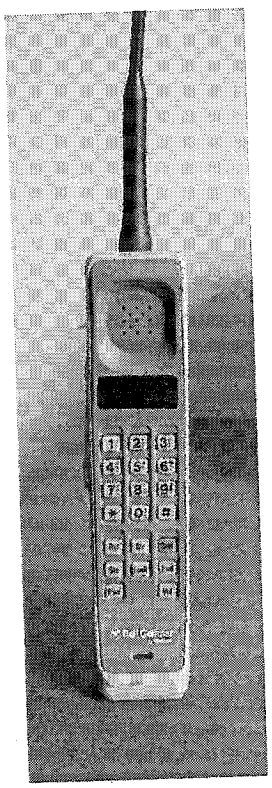

Figure 2.3 Motorola Handset

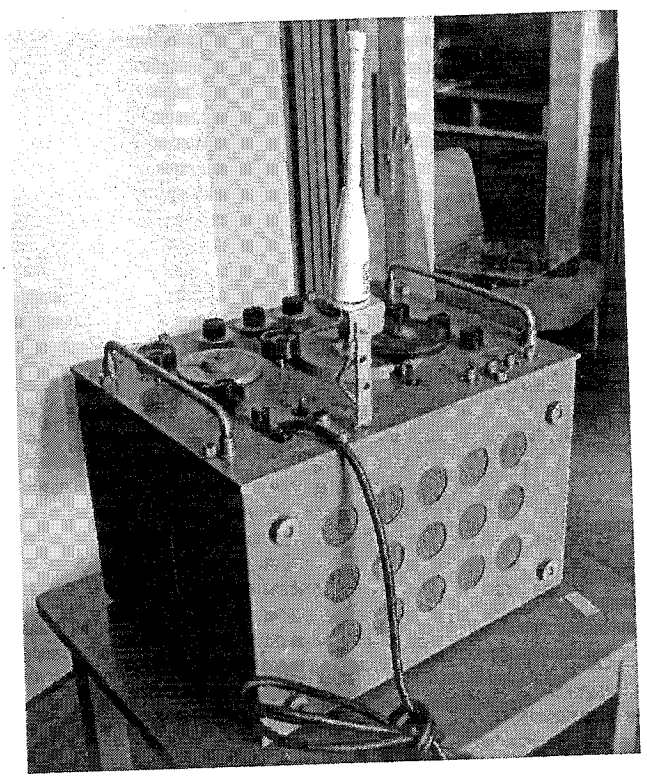

Figure 2.4 RF signal generator and monopole

The source was placed at a fixed location for the duration of a measurement. The power of the transmitter was monitored during the survey in order to insure consistency in the measurements. This was done by recording the received power of an antenna in a fixed location or reference point at different times of the study, also the power meter on the source was monitored at fixed intervals during the measurements. The field strengths were later scaled to 0.6 watts radiated power as described below. The measurements were usually repeated three times in order to confirm results and to evaluate time invariance. For both 850 and 1900 MHz measurements, the transmit and receive antennas were oriented vertically. The 1900 MHz source used a 20 x 20 cm^2 square ground plane mounted at the feed point of the monopole. The ground plane is not shown in figure 2.4.

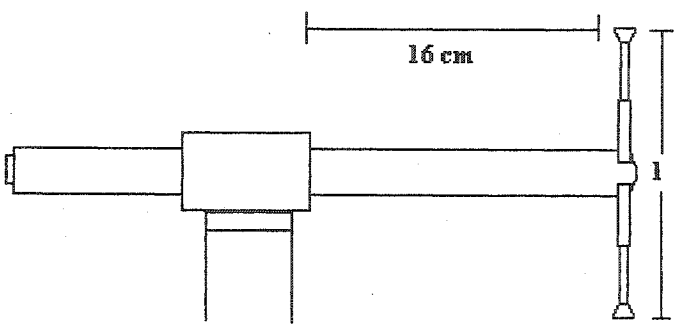

Figure 2.5 Schematic of receive antenna

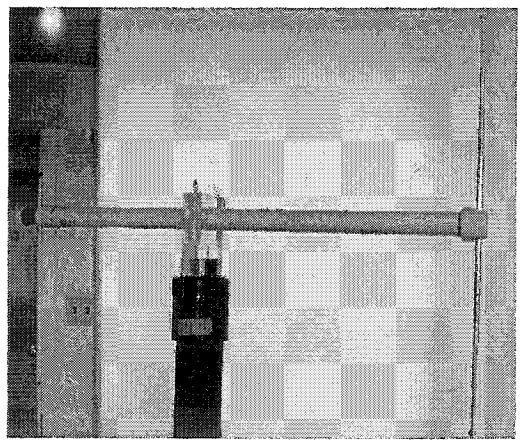

Figure 2.6 Photograph of Rx antenna

The receiver was a vertical dipole, Electromechanics 3121C-db4, shown in figures 2.5 and 2.6. At 850 MHz the dipole arms were extended to l = 17.65 cm. For 1900 MHz, the arms were extended to l = 14 cm. The antenna was fixed to the pole approximately 16 cm from the receiving arms of the antenna.

Mr. David Chu developed a microprocessor-controlled robot, figures 2.7 and 2.8, according to the author's specifications. The robot carries the receive antenna along the straight-line path or "trajectory". The robot travels along the trajectory stopping every 3.2 cm, for high-resolution measurements, for sampling of the field strength. Coarser sampling at multiples of 3.2 cm was also used for some measurements. The robot permits measurements to be made with greater efficiency and with greater repeatability. Figure 2.7 shows a sketch of the robot with the dipole measurement antenna; the dipole is sketched in figure 2.5. The height of the antenna center (h2) and the total height of the robot and antenna (h1), are adjusted using the pole mounted into the base of the robot. This height was adjusted prior to measurements. Field readings were taken at fixed intervals along a trajectory. The spacing between consecutive measurement points was fixed at the beginning of each measurement, from 3.2 cm to 1 meter between measurement points. The 3.2 cm spacing was needed to reveal the fine structure of the fields and provided 1,563 data points per trial in a 50-meter corridor [22].

The robot used infrared sensors to follow paths placed along the floor prior to measurements. This feature allowed the robot to follow a complex scan pattern without direct human intervention. The displacement of the robot along a path was measured by the counting of marks along a wheel with an infrared sensor. The smallest displacement interval was 3.2 cm with an averaged error on the order of one twentieth of a millimeter. This level of accuracy was obtained by using a code wheel and infrared sensors to measure the displacement of the robot along the path.

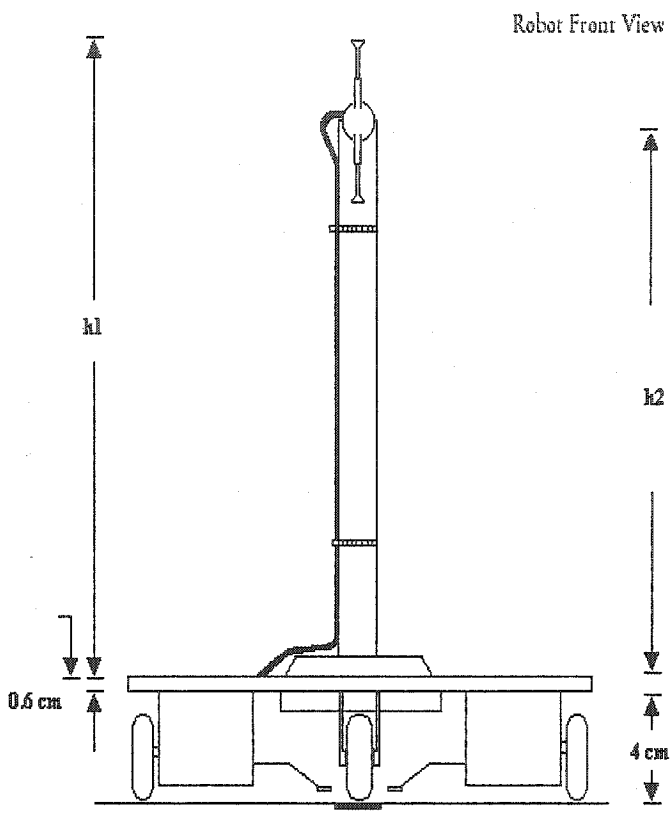

Figure 2.7 Robot schematic

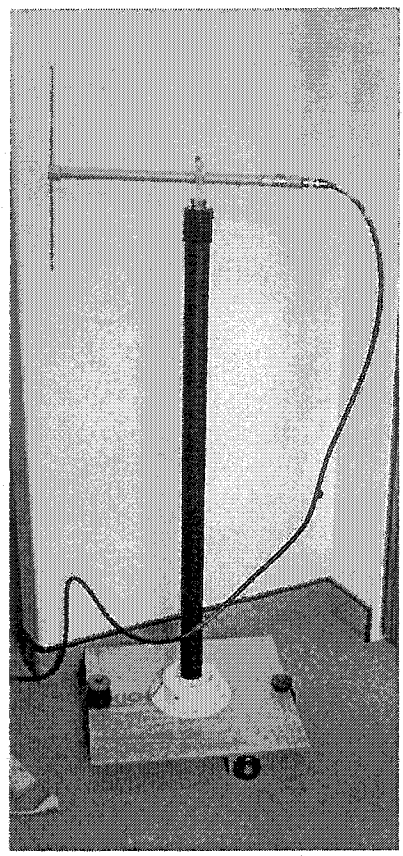

Figure 2.8 Photo of robot

2.2.2 Sampling Intervals

As discussed above, the robot allowed a maximum sampling resolution of 3.2 cm between sample points; this corresponds to about one tenth of a wavelength between samples at 850 MHz and one fifth of a wavelength between samples at 1900 MHz. Larger sample spacing were multiples of 3.2 cm. The resolution of the sampling will be discussed in more detail in the section about trajectory measurements in Chapter 3. The separation between transmit and receive antennas was computed as the three

dimensional distance between the feed point of the transmit antenna and the center of the receive dipole.

The antenna was moved along the trajectory in 3.2 cm steps that produced 1,563 samples per trajectory in a 50-meter long corridor. The power readings from the spectrum analyzer that was connected to the antenna were converted to field strength using the calibration data for the antenna that was supplied by the manufacturer.

2.2.3 Calibration of Measured Fields to 600 mW

The task of comparing in-building measured fields with simulations requires that some practical concerns be dealt with. The first issue is that the assumption of waves propagating in free space, which is the foundation of many of the relationships used in field measurements [3, 4, 80], was not valid within buildings. The second concern is that a practical wireless source does not radiate the full power sent to the antenna, due to mismatch and absorption of energy by nearby structures. With these factors in mind, the measurement process adopted a calibration process to address some of the concerns about the indoor measurements [23].

Before and after a series of measurements, the antenna was calibrated by performing measurements within a large open room, a gym, within the hospital. This room was 18.1x15 square meters in cross section and over 4 meters from the floor to ceiling. The transmitter was placed approximately in the center of the gym as shown in figure 2.9.

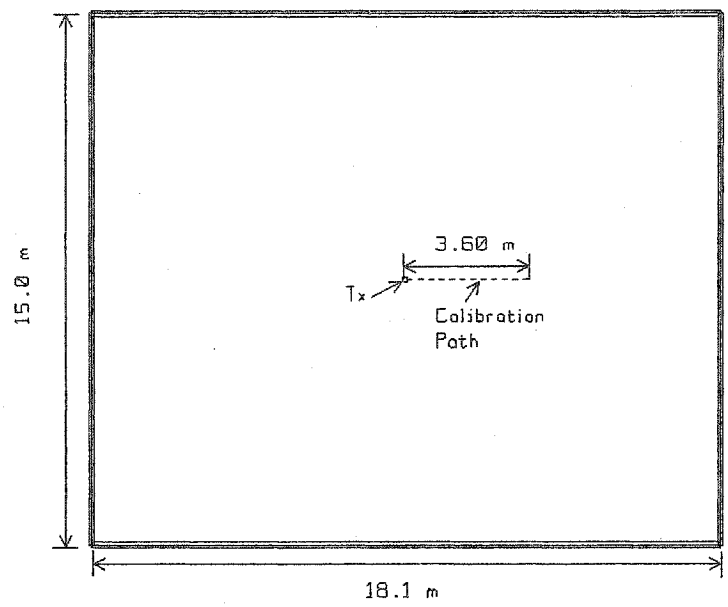

Figure 2.9 Schematic of large room used in the calibration of measured data to 600 mW radiated power.

Near the transmitter, the field strength in the large room decreases as 1/distance, the same rate as free space. Close to the transmitter, the field associated with the direct ray going from the transmitter to the receiver dominates, that is, it is much larger than the field of the rays reflecting from the distant walls. Field measurements were performed on a straight-line trajectory with 10 cm spacing between points. Simulations were then performed in a model of the gym with 10 cm spacing between points. The measured field strengths near the source were compared to the simulated field strengths near the source, illustrated in figure 2.10. The difference between the expected field from the simulations and the actual radiated field was determined. This difference, 10 dB in the case of figure 2.10, was used as a calibration factor to scale the measured fields to a radiated power of 600 mW. The measured data was adjusted with the calibration factor before comparison with the simulated data. The calibration

factor was varied from 6-12 dB in this thesis. The calibration only affects the magnitude, not the structure, of the measured fields.

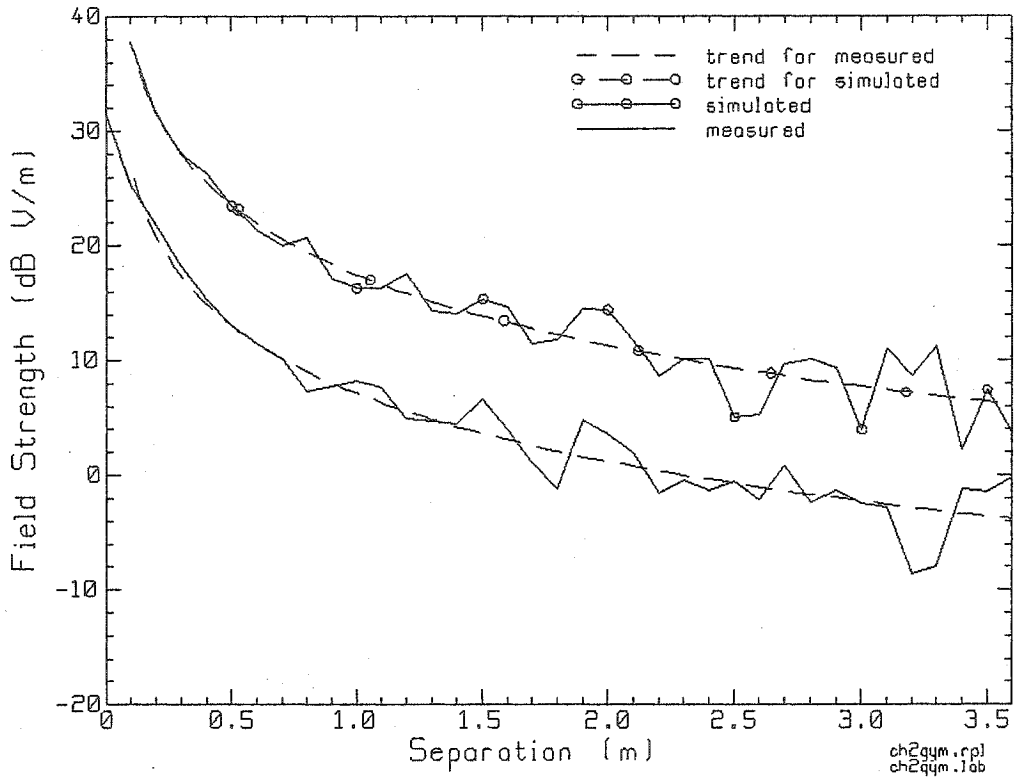

Figure 2.10 Measured and simulated data used for 600 mW calibration of fields.

Both the measured and simulated field strengths decrease with distance at approximately the same rate (1/distance). The simulated field strength assumes that the source is radiating 600 mW, this is the worst-case scenario in terms of EMI risk. By calibrating the source to the maximum radiated power, the EMI risk estimates based on the calibrated fields are worst-case estimates of risk.

2.2.4 Measurement Formats

The basic measurement format was the trajectory measurement. An example of the field strength data obtained from a centerline scan within a corridor is shown in figure 224. The horizontal axis is the separation between the receive and transmit antenna, using a logarithmic scale, while the vertical axis is field strength at the receiver in "dB V/m", meaning that 0 dB V/m corresponds to a field strength of 1 V/m. The calibrated data, solid line, was used in this thesis as explained above. Since the calibration only scales the magnitude of the data, the structure of the fields remains intact as seen in figure 2.2. The structure of the field, an interference pattern due to the ray arriving directly from the transmitter and rays arriving via reflections from walls, became more complex with increasing distance from the source. This might be explained by the fields nearer to the source being dominated by the "direct ray" from the source; the reflected rays are weaker and unable to cause large variations in the field strength. Further from the source, the sum of the field contributions of the reflected rays is strong enough to cancel the direct ray, causing deep minima. The field strength drops faster near the source and slower further from the source as interference cancellation leading to sharp nulls, rapid drops of more than 10 dB, occurred at locations further than 2 meters from the source.

Trajectory measurements were made in the 50-meter corridor of figure 2.1 along trajectories that ran parallel to the corridor centerline but passed through different portions of the corridor volume, e.g. above or below the corridor centerline or to the left or right of the corridor centerline, called *off-centerline trajectories*. These

measurements were used to construct a *volume scan* of the fields within a corridor. The volume scan was obtained by performing multiple off-centerline trajectories within the corridor volume in order to measure the field strength within the corridor volume. The spacing of the off-centerline trajectories determines the *cross-sectional or lateral resolution* of the volume scan while the spacing between samples on the trajectories determines the *longitudinal resolution* of the volume scan. The results of a volume scan are trajectories in figure 2.11.

The volume scan used three heights, 30, 120 and 207 cm above the floor and four distances from a reference side wall, 60, 77, 92 and 160 cm from side wall, to generate 12 cross-sectional locations [24]. Each cross-sectional location was the starting point for one measurement trajectory. The plot used the same axis format as in the centerline trajectory measurements.

The volume scan data used in this thesis was a preliminary investigation into the field structure within a corridor volume and as such used lower resolution than the centerline scans discussed previously. The longitudinal resolution was 32 cm between samples, producing 158 samples per trajectory, along the trajectory and the lateral resolution varied from 20 to 90 cm between adjacent off-centerline trajectories. The source was a signal generator set to produce a 1900 MHz sine wave that drove a vertical monopole antenna with a square ground plane with a side length of 20 cm. The measured fields were calibrated in the same manner as in the centerline

trajectories. Figure 2.11 shows some of the off-centerline trajectory measurement data used to construct the volume scan.

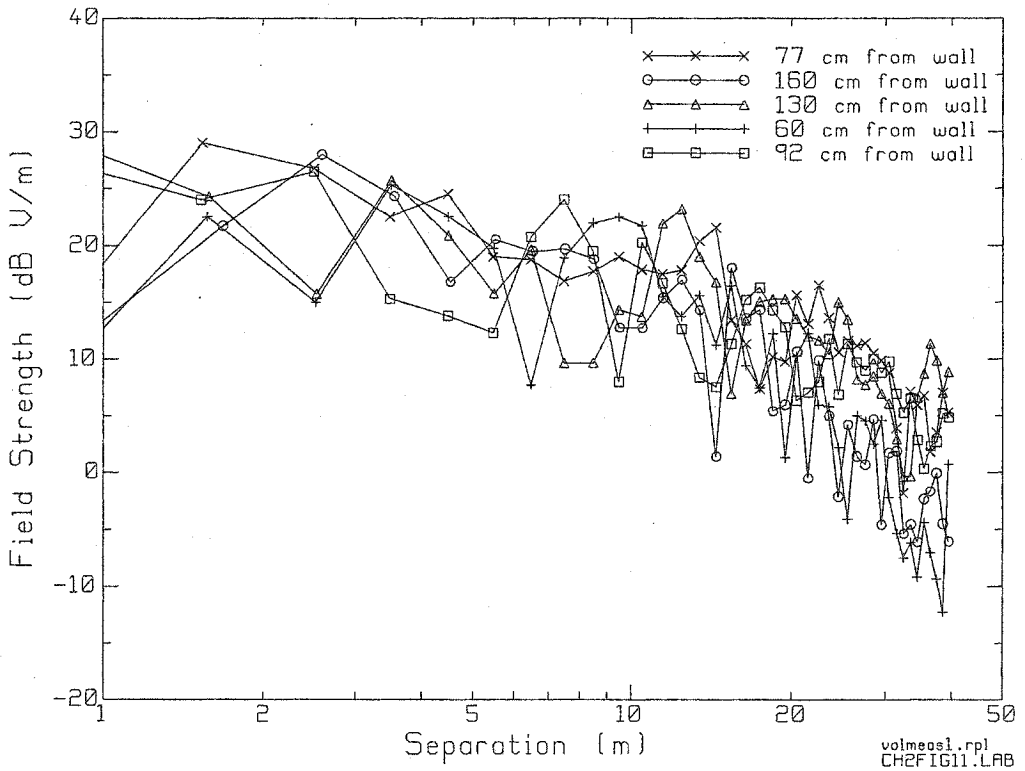

Figure 2.11 Measured fields taken at different distances from side wall at 120 cm height at 1900 MHz. Source 600 mW monopole over a 20x20 cm ground plane.

The measurements taken at 120 and 207 cm above the floor tended to be high near the source and decrease with distance from the transmitter at different rates. In contrast, the field strength at 30 cm did not substantially decrease as the receiver was moved further from the transmitter, but rather varied about constant level. This lead to field measurements taken 30 cm above the floor having the lowest field strengths when close to the source, but the highest field strengths near the end of the corridor. The measurements taken at 30 cm above the floor were remarkable in that the field

strength decreased at such a slow rate as to appear constant for the entire trajectory. This previously unreported behavior suggested different propagation mechanisms dominated the fields at 120 and 207 cm above the floor than the fields at 30 cm above the floor.

The interference patterns in figure 2.11 did not have the same amount of detail as the highly sampled centerline trajectory; the curves lacked the smoothness of the centerline trajectory measurements. The deep nulls occurred, as in the higher resolution centerline trajectory measurements, after 2 meters separation.

2.3 Room Measurements

The room used most in this study was constructed of the same materials as the corridor discussed above and is representative of a small single-bed hospital room. The room main space was 3x3 meters of floor space, with a 1 meter wide and 0.8 meters long alcove leading to the connecting corridor. The hanging ceiling was 2.5 meters above the floor. There was a metallic screen covering a window located opposite the entrance to the room. A schematic of the room is shown in figure 2.12.

The source was placed 2.5 meters from the left wall, 0.5 meters from the bottom wall and the center of the source, where the antenna joins with the body of the cell phone, was 1.3 meters above the floor. The field in the small room was measured as a planar surface measurement. A planar surface measurement was composed of a series of closely spaced parallel trajectory measurements on the planar surface. The spacing of the trajectories is the same as the spacing of the measurement points on each

trajectory. Then the data formed a grid of uniformly distributed data points on a planar surface. The trajectories followed the horizontal axis of figure 2.12 with measurements every 3.2 cm apart. Each trajectory was 3.2 cm from the adjacent trajectory. This format provided a grid of data with 3.2 cm separation between adjacent data points along the horizontal or vertical path and 4.5 cm between diagonal adjacent points: this produced a planar surface data set of 6,103 points per trial.

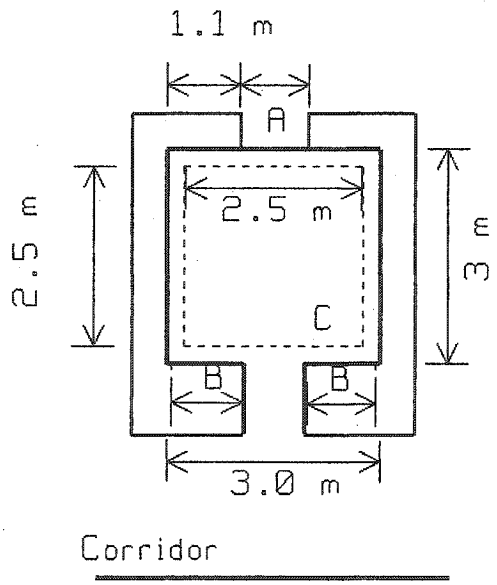

Figure 2.12: Schematic of room used in measurements at 850 MHz. A= window+ screen 0.9 m wide, B= concrete wall + shelving 1 m square, C= source location, dashed line boundary of measurement region 2.5x2.5 square. Dimensions are rounded.

An illustrative example of planar surface measurements is the 2.5-meter x 2.5-meter measurement room measurement, divided into a grid composed of 3.2 cm x 3.2 cm squares, shown in figure 2.13. The electric field was measured at the center of each

grid square; this measurement was used to approximate the field strength for the entire square. The source was located near one corner, but off of the diagonal, of the square planar surface in figure 2.12. Due to limitations in the experimental set-up, a region the in upper right hand corner of the grid in figure 2.13 was not measured as the robot was unable to approach close enough.

The regions with the highest field strength, red and orange, are located around the source, near the bottom right corner of the surface. The intermediate field strengths, yellow, occur throughout the planar surface, even in regions furthest from the source. Weaker fields, blues, are found in regions further than 30 cm from the corner closest to the source. The complex structure of the interference patterns on the planar surface exhibit behavior that may initially be counter-intuitive: moving further from the source does not always insure weaker field strengths.

The data was also plotted, figure 2.14, in an oblique three-dimensional view in order to appreciate the structure of the interference patterns. This presentation format provides insight into the structure, or morphology, of the fields on the planar surface. However, the highly structured interference pattern made the oblique view less useful for quantitative analysis due to the large amount of information. The contour plot format is used for corridor planar surface data was for evaluation of planar surface data. The same data set plotted using contour mapping is found in figure 2.15

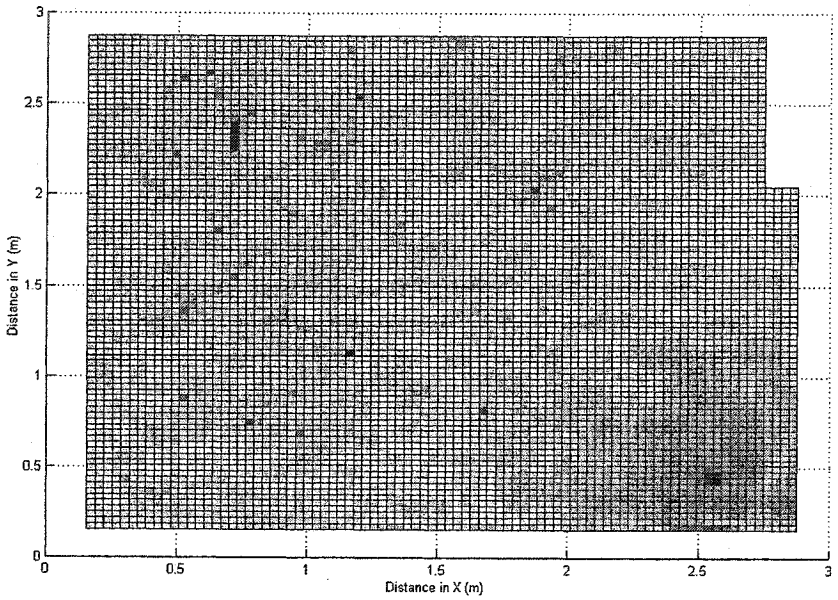

Figure 2.13 Grid of Measurement points with associated field strengths. White regions indicate where no measurements were performed. Source located near bottom right corner.

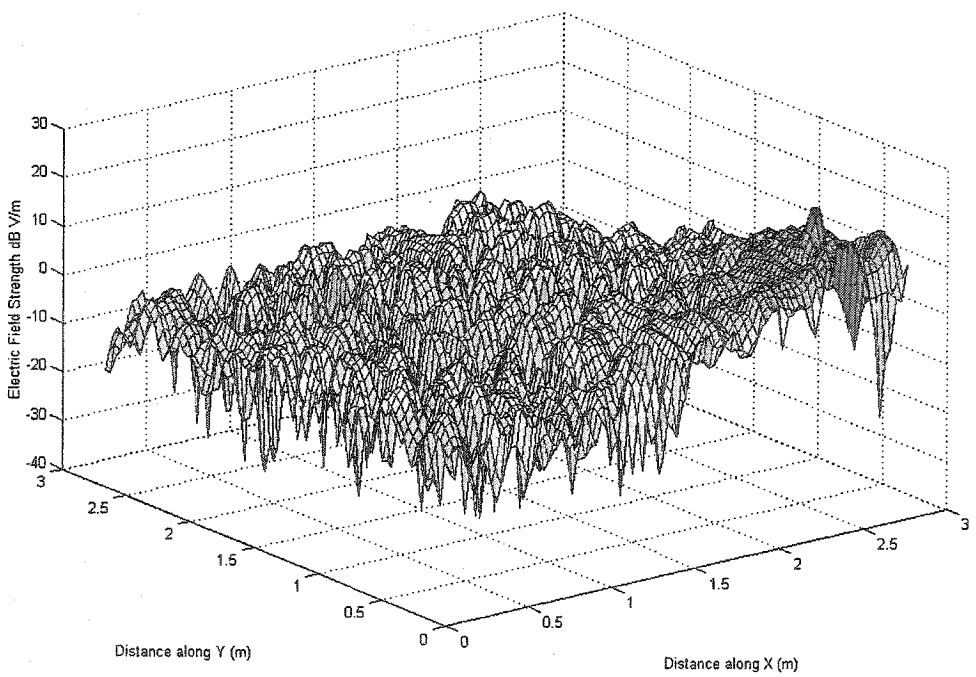

Figure 2.14 Oblique three-dimensional surface plot of 850 MHz measured room fields

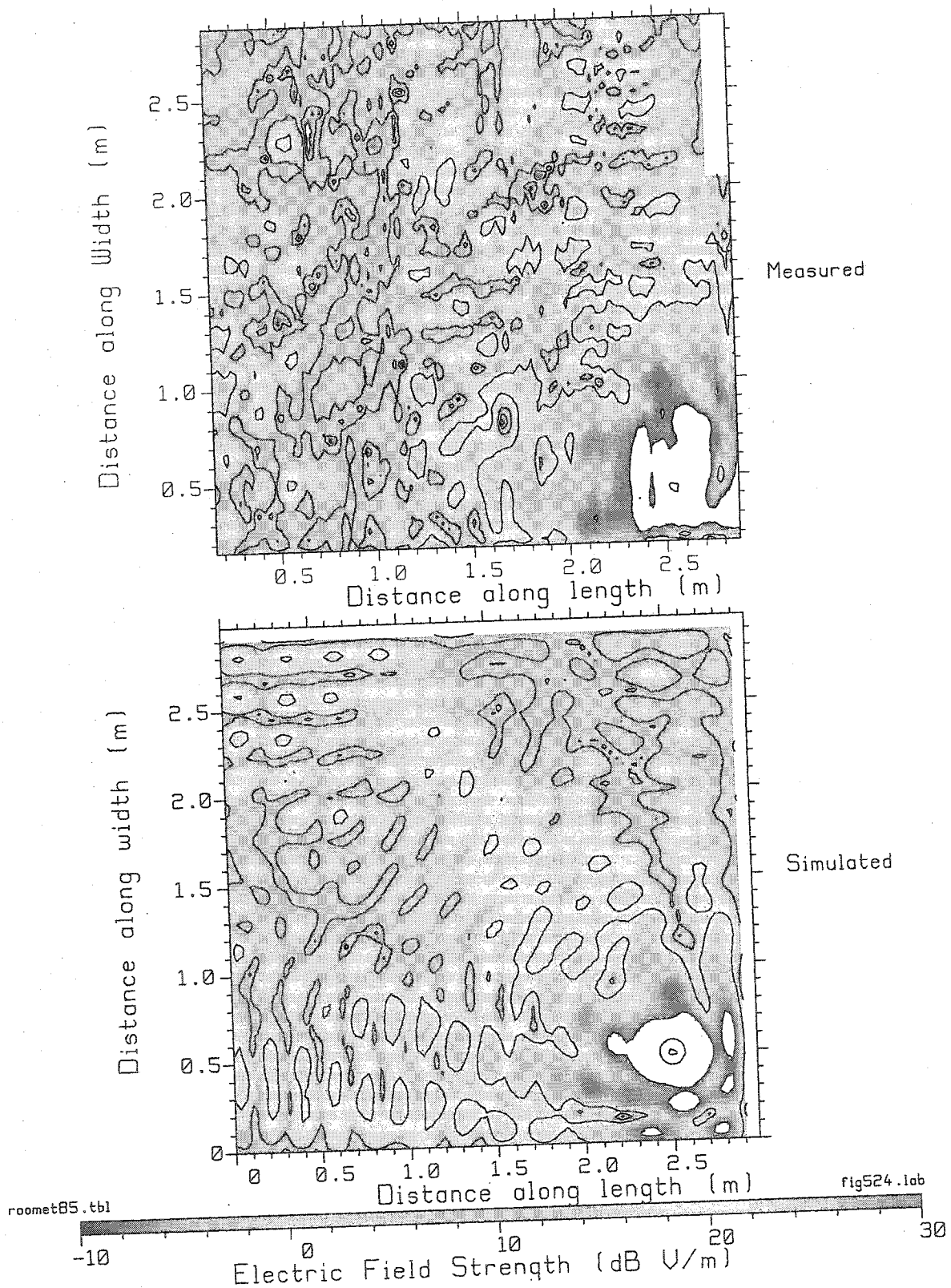

Figure 2.15 Measured and simulated field strength in clay-block room at 850 MHz.

The changing contours represent 10 dB differences in field strength using 1V/m as the reference field strength. The source is located near the bottom right hand corner of the plot. The high field strengths are distributed throughout the room, even in the corner furthest from the source. The interference pattern is not symmetric, which may be explained by the fact that the source is off the diagonal of the room. The interference pattern shows some alignment with the upper and left hand walls, with respect to the source.

2.3.1 Room Trajectories

Trajectory information was obtained from the planar surface data by extracting points on the surface that fell on the trajectory. An example of two room trajectories is shown in figure 2.16.

The trajectory labeled path A in figure 2.16, traveled from the bottom right corner of the room to the upper left corner of the room. This path passed through the location of the source and ended at the corner furthest from the source. Path A was used to investigate the rate of field drop as a function of separation between transmit and receive antennas.

A second path, labeled path B in figure 2.16, was selected to travel from the bottom left corner to the upper right corner of the room. The points along this trajectory were selected to very approximately give the mid-point values of the field within the room. This path was chosen to investigate interference patterns at a roughly constant distance from the source.

The simulated data was validated by the measurements whenever possible. The next section will discuss the methods used to obtain simulated field data in a corridor.

The measured and simulated electric fields along the trajectory path A, figure 2.17 (a), displayed prominent interference patterns along the entire path. The field strength within 50 cm of the source decreased as distance from the source increased. Further than 50 cm from the source, the field strength varied about the 10 dB V/m level.

The field strength along path B, figure 2.17 (b), displayed a non-uniform interference pattern; this was expected, as the source was located off the diagonal of the room. The field strength varied about the 10 dB V/m level.

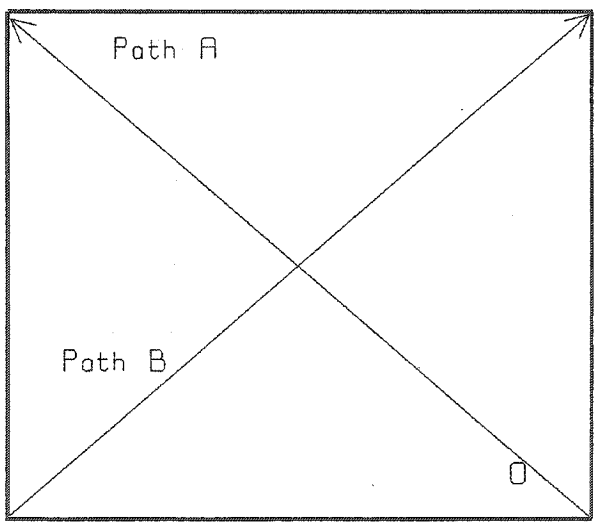

Figure 2.16 Plan View of 2.5 x 2.5 measurement area with trajectories indicated. Source located near corner with a rectangle as marker.

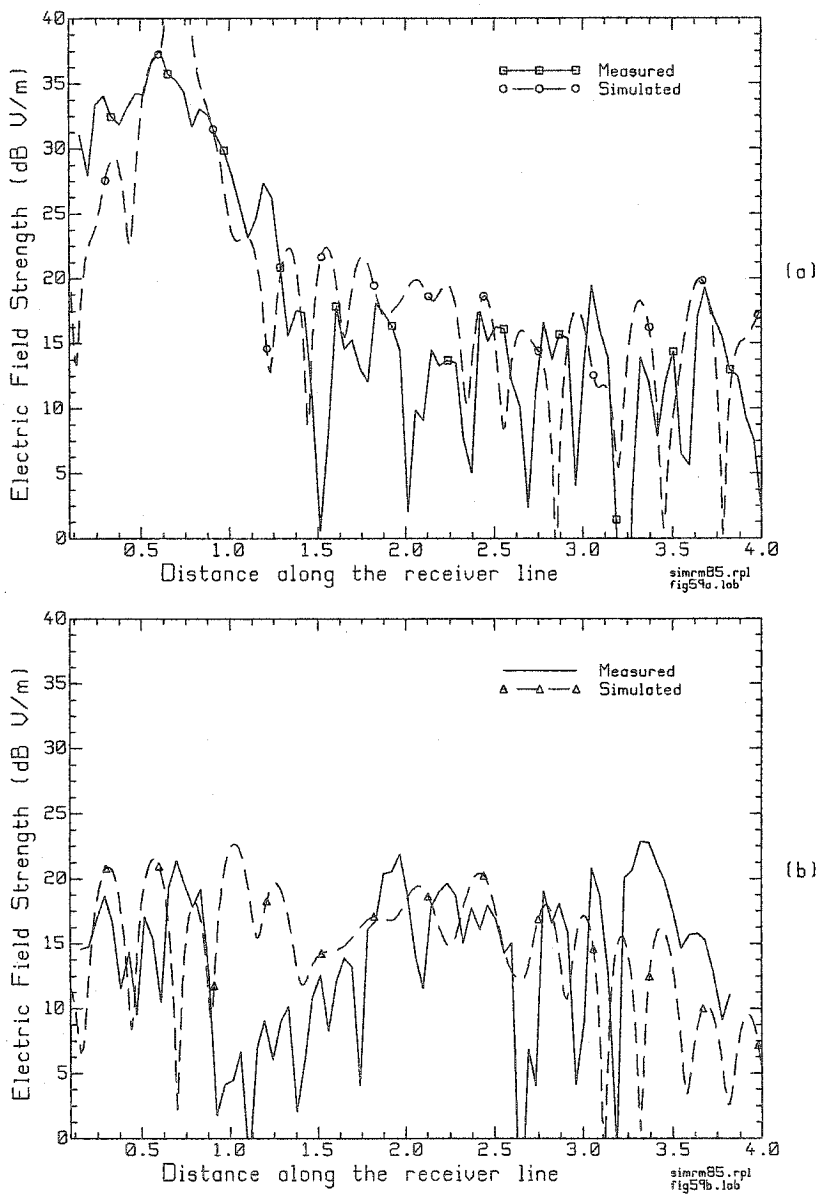

Figure 2.17 (a) Field strength along path A and (b) along path B (2.15 B), for measurements and simulations at 850 MHz in clay-block walled room. Source location indicated in figure 2.16.

Evaluation of propagation characteristics such as rate at which field strength drops with distance along a particular trajectory requires caution. If the trajectory follows contours of constant distance from the source or constant phase surfaces on an

interference pattern, propagation characteristics obtained from such a trajectory may be misleading. For example, movement along path B does not produce large differences in the distance between the source and the observer, and consequently the change in field strength is due to interference patterns rather than attenuation of field strength.

2.4 Indoor Propagation Simulations

The numerical simulation of electromagnetic fields, performed by Geometrical Optics based code GO_3D [34, 57, 86] developed by Dr. C.W. Trueman, was validated where possible by the author with measurements. Geometrical Optics (GO) assumes that an electromagnetic field travels along straight-line paths called "rays". The field associated with each ray is a quasi-plane wave. The ray has two vector components perpendicular to the direction of propagation. The source launches rays in all directions; the polarization and field strength associated with a particular ray depends on the source's radiation pattern as well as the radiated power of the antenna. This ray-optical technique offered several advantages; the environment was electrically large with dimensions on the order of tens or even hundreds of wavelengths. Ray-optical codes are more computationally efficient for larger structures than moment method or finite difference based codes. Different wall properties or source locations can be easily accommodated in such a code. In this thesis, the source was a vertical half-wave dipole radiating 0.6 watts.

The coordinate system used for the antenna is shown in figure 2.18. In the simulations, a half wave dipole transmitter was used. The phase center of the antenna corresponds to the axis origin of the figure. The ray (R) radiates out from the phase center of the source towards some point in space. The electric field is polarized in the theta (θ) direction.

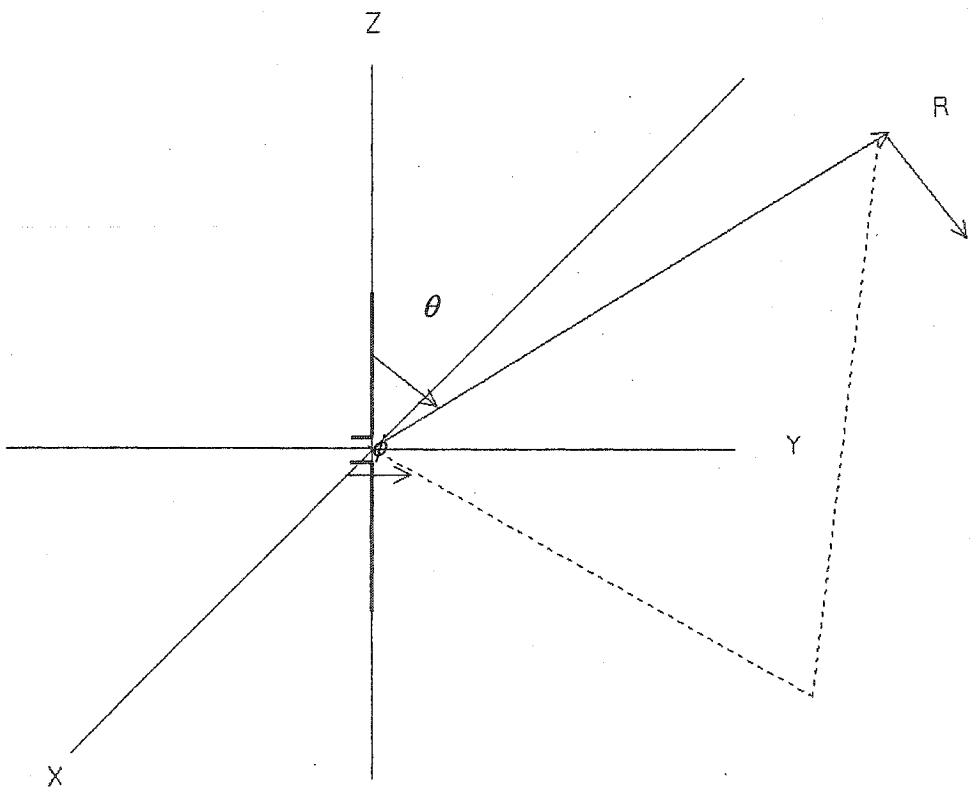

Figure 2.18 Coordinate system for GO models

The equation for the electric field strength radiated by the source is:

$$E_\theta(R) = \sqrt{2\pi\eta P}\,\frac{F(\theta)}{r}, \qquad \ldots 2\text{-}1$$

where P is the power radiated by the source and $F(\theta)$ is the radiation pattern of the source. In the case of a half wave dipole, the radiation pattern is: $F(\theta)=\frac{\cos\left(\pi/2\cos(\theta)\right)}{\sin(\theta)}$. The rays may arrive at the observer directly or through reflections. Figure 2.19 shows some of the possible paths that can link the source and observer.

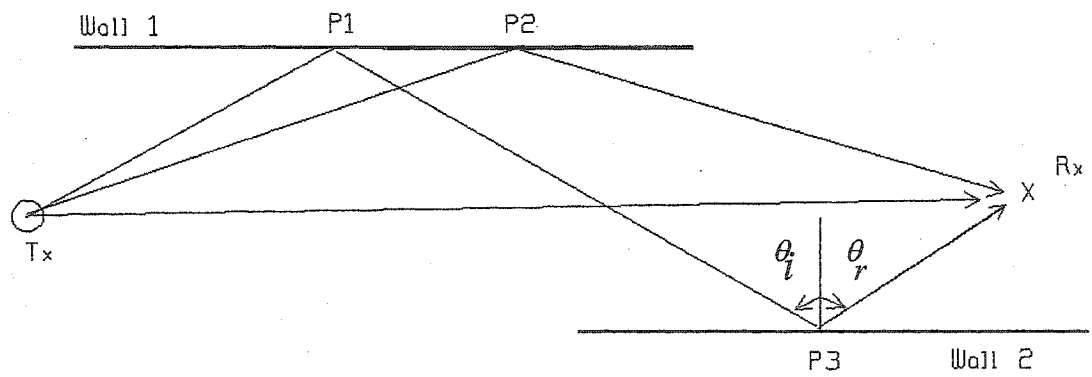

Figure 2.19 Ray paths linking source (Tx) and observer (Rx).

A ray may travel directly from the source, located at Tx, towards the observer, located at Rx. The rays may follow a path that reflects once from surface and then propagates to the observer. An example of a single reflection path is: A ray travels from Tx to P2, located on wall 1, reflects from wall 1 and then travels to Rx. Rays may follow paths with multiple reflections. An example of a path with two reflections is: A ray travels

from Tx to P2, located on wall 1, reflects and travels to P3 on wall 2. The ray then travels to Rx. All reflections obey Snell's law of reflection that states that the angle of incidence (θ_i), angle between the normal vector of the surface and the ray path of the incident ray, must be equal to the angle of reflection (θ_r), the angle formed by the normal vector of the surface and the ray path of the reflected ray.

Reflected fields and their associated ray paths are computed using *images*. Images are equivalent sources that generate reflected rays to account for the presence of walls. If the ray produced by the image source passes through the actual surface of the wall the ray is used in the computation of the field. However, if the ray does not pass though the actual wall surface, the ray is discarded. The rays from images may also reflect from surfaces. These reflections are handled by producing additional images. The number of possible images depends upon the maximum number of reflections allowed for a particular ray path.

The reflected field is computed by decomposing the incident field into *parallel* $\Gamma_{||}$ and *perpendicular* $\Gamma_{\perp}$ components. The magnitude and phase both the parallel and perpendicular reflection coefficient are then computed. The reflection coefficient for multi-layer structures is used in these simulations [59]. The electric field phasor is multiplied by the appropriate reflection coefficient for both parallel and perpendicular polarizations. The X,Y,Z components of the reflected field are then reconstructed from the parallel and perpendicular polarizations.

Walls in this thesis are modeled as multi-layer structures where each layer has an individual permittivity, conductivity and permeability [88]. The most common building materials were clay-block (walls), wood (doors) and glass-block (walls). The clay-block wall has a layered construction; an inner section of hollow clay-blocks are covered with a concrete plaster. Supports, as well as wires and piping are fitted, through the interior air gaps but these cannot be included in the simulation because their locations are unknown. A schematic of the cross-section of a clay-block wall is shown in figure 2.20.

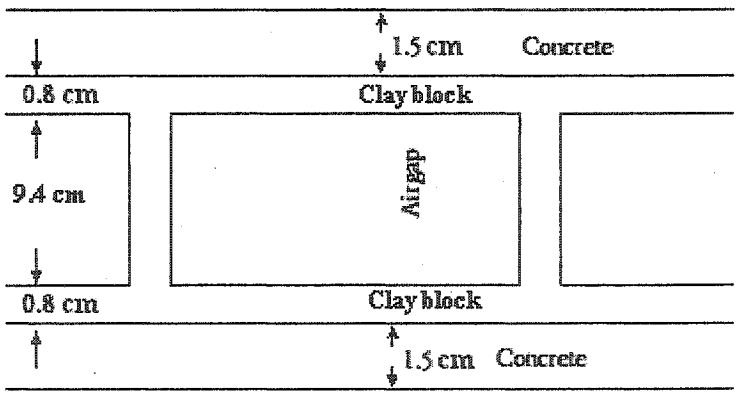

Figure 2.20 Schematic of clay-block wall cross-section

The electrical properties of the various materials used in the simulations are shown in table 2.1. Any layered structures used in the simulations are composed of the materials in table 2.1.

The material properties used are for 850 MHz and their use at 1900 MHz may introduce some inaccuracy in the simulations. All of the materials have relative permeability of 1. Brick is a lossy dielectric with a relative permittivity of 5.1 and a

conductivity of 10 S/m. Concrete has a relative permittivity of 6.1 and a conductivity of 60.1 S/m. Dry wood, used to model the interior doors, has a relative permittivity of 2.5 and a conductivity of 1.18 S/m. Metallic structures have a relative permittivity of 1 and a conductivity of 10^7. Glass, for the end walls of the corridor and for windows, has a relative permittivity of 6.0 and a conductivity of 10^{-9} [88].

Table 2.1

Electrical properties of materials used in simulations

Name	ε_r	σ	μ_r
Brick	5.1	10	1
Concrete	6.1	60.1	1
Wood	2.5	1.18	1
Metal	1	10^7	1
Glass	6.0	10^{-9}	1

The reflection coefficient of the different building materials, i.e. clay-block, wood and glass block, is an incident angle dependent quantity. The magnitude of the reflection coefficients for both polarizations as a function of incidence angle is plotted in figure 2.21.

The layered clay-block wall has a high reflection coefficient for normal incidence, nearly 0.8, which is much larger than the normal reflection coefficients for the wood (0.41) and glass-block (0.18). This causes the clay-block walls to dominate the

reflections near the source where the incidence angles tend towards normal incidence (0 degrees).

As the angle of incidence tends towards grazing incidence (90 degrees), the magnitude of the reflection coefficients tend towards 1, total reflection, for all materials and polarizations. This implies that all of the materials used in the simulations would act as strong reflectors for grazing incidence. Grazing incidence is particularly important for the 50-meter corridor of figure 2.1, where the distance between the source and the observer are large [23, 88].

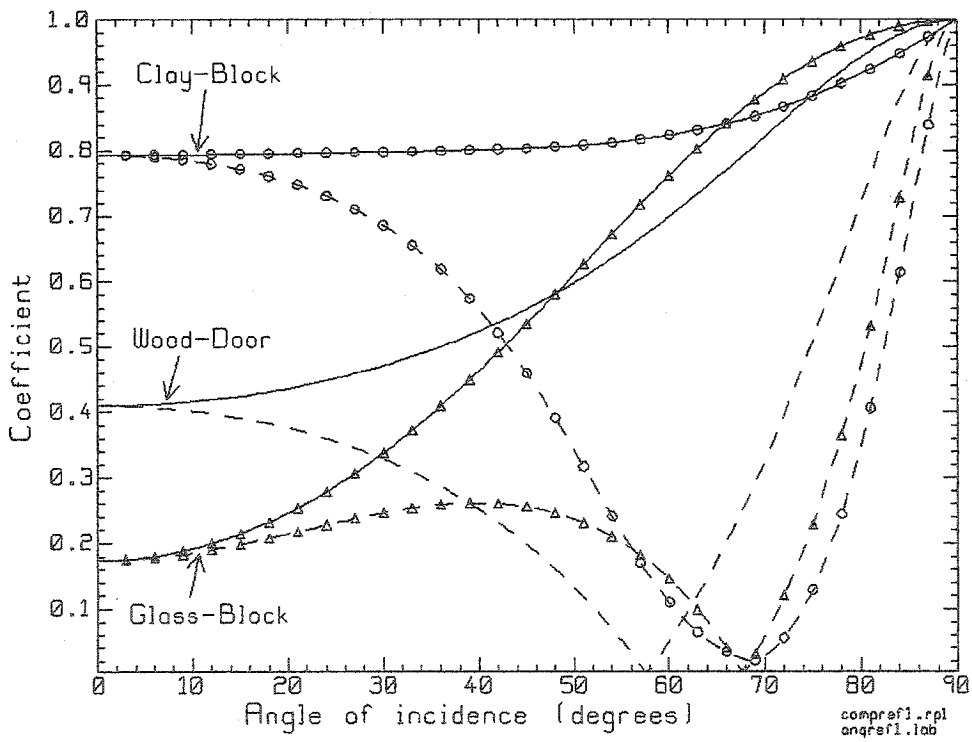

Figure 2.21 Parallel and perpendicular reflection coefficients for building materials at 850 MHz. Parallel polarization: Clay-block (dashed-circle), wood (dashed) and glass-block (dashed-triangles). Perpendicular polarization: Clay-block (solid-circle), wood (solid), and glass-block (solid triangle).

There are conditions where for certain polarizations (parallel) and angles (Brewster angle) of incidence most of the field is transmitted through the wall or door. This transmission occurred for an incidence angle of 58 degrees for wood, 68 degrees for glass-block and 70 degrees for clay-block. Regions where the ray strikes the surface at the above incidence angles will have very small reflected-field strengths.

The reflection coefficient is also a frequency-dependent quantity. At some frequencies the normal reflection coefficient will be relatively large and at others the normal reflection coefficient will be smaller. This behavior, called the radome effect [61], can change the character of the simulated fields. The magnitude of the normal reflection coefficient is plotted in figure 2.22.

The normal reflection coefficient can be used to estimate the reflectivity of a particular structure. At 850 MHz, clay-block walls were substantially higher reflectors than the glass-block walls or wood-doors. The same was true for 1900 MHz simulations, but the glass-block walls had higher reflection coefficients and wood-doors had smaller reflection coefficients. At 2400 MHz, the glass-block wall is a more substantive reflector than the clay-block wall.

This implies that clay-block walls tended to be strong reflectors for normal incidence when performing 850 and 1900 MHz simulations, but that glass-block walls tended to be stronger reflectors at 2400 MHz. Since strong reflectors produce strong images, strong reflector surfaces often require larger number of images. It should be noted that

when computing fields in regions where grazing incidence occurs, all materials have strong reflection coefficients and a larger number of images may be required.

The generation of images is handled using an image tree approach. The source generates first level images. These images produce second level images; in turn these images produce other images. While the number of possible images is large, the number of images required for accurate reproduction of field strength is often much less than the maximum number of possible images. The reason for this is that each generation of images is typically weaker than the parent generation. At some point, the contributions of many images becomes negligible. There are different techniques to limit the number of images used in field computation.

Some authors impose a hard limit on the number of image sources used for field computation [14, 44, 47], this thesis uses the strength of the image sources to limit the number of images used. The code will continue to generate images until the contribution of the image drops below a particular threshold, 20 dB below the isotropic level as computed using equation 2-1. Once the image strength is below a given threshold, it will not produce any more images. This technique has the advantage of using as many images as necessary to compute the field strength, since it is often difficult to know prior to simulation the number of images required to obtain accurate reproduction of the field.

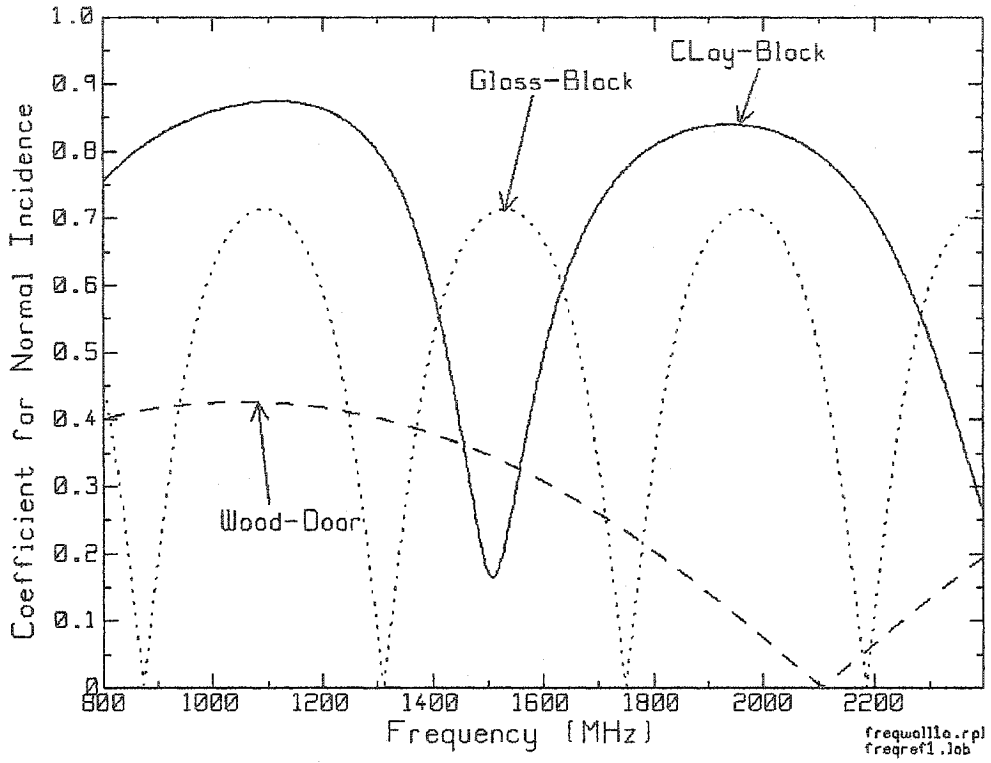

Figure 2.22 Magnitude of the normal reflection coefficient for clay-block (solid), wood (dashed) and glass-block (dotted) for 800 to 2400 MHz.

All three polarizations, E_x E_y and E_z, of the electric field were computed as well as the total field, which is the vector sum of all three polarizations. This is a worst-case field level that would occur if all three components were in phase. The transmitter was assumed to be radiating at full power with no loss factors. This was taken to be the worst-case scenario for EMC purposes. Note that when the source and receive antenna are close but at different heights, the total field strength differs from the actual field strength. The actual power radiated by mobile sources is normally much less than the maximum power [33].

A practical concern when comparing simulated and measured fields is that the measurement antenna will average the field while the simulations compute the field at a point. This difference will cause some differences in the details of the structure of the interference pattern of the electric field. In geometrical optics, rays can suddenly disappear or appear in the computation due to shadowing. These sudden changes in the number of rays can cause discontinuities in the simulated fields which would appear as sharp spikes in field strength found in field strength plots. This is a feature of geometrical optics and might be resolved by incorporating diffraction into the computation to smooth out the discontinuities [57]. Since the simulation work in this thesis is concerned with line of sight situations where shadowing is typically not as important factor in field computation, diffraction was not incorporated into the modeling process.

2.4.1 Typical Corridor Simulations:

The corridor of figure 2.1, modeled with geometrical optics and used in the simulation, was approximately 50 meters long and 2 meters wide. The ceiling was 2.5 meters above the floor. The side walls of the corridor were layered clay-block walls 14.5 cm thick, while the floor and ceiling were reinforced concrete 30 cm thick. The end walls were glass-block walls 14 cm thick. The source was a 0.6 watt vertical dipole that was located in a position along the centerline of the corridor some distance from the left end wall, please refer to figure 2.1 for more detail. The fields were

simulated on a planar surface that was parallel to the floor. The height of the planar surface above the floor was fixed for a particular simulation. The simulated fields on a planar surface were displayed using contour plots. The field strength was plotted on dB scale using 1 V/m electric field strength as the reference level, is shown in figure 2.23. Since the corridor is about 25 times longer than it is wide, the figure is a narrow strip of data.

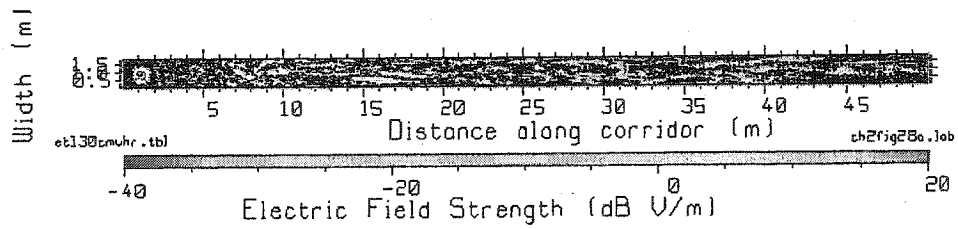

Figure 2.23 Field strength on planar surface at 1900 MHz due to 0.6-watt dipole source located 1.2 m from end wall using a 1-1 aspect ratio.

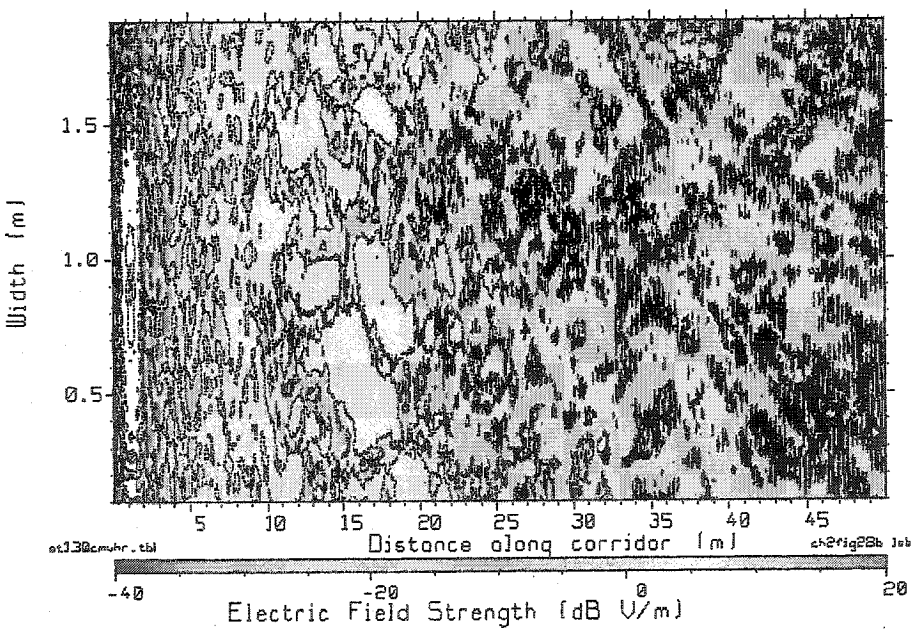

Figure 2.24 Field strength on planar surface at 1900 MHz due to 0.6-watt dipole source located 1.2 m from end wall using a 25-1 aspect ratio.

When using a 1-1 aspect ratio, the structure of the field was difficult to discern. To improve the presentation of the field structure for the entire corridor, the aspect ratio was changed to 25-1 as in figure 2.24. For smaller surface areas, the aspect ratio of 1-1 was used.

The simulated field strength is plotted using a dB scale with 1 V/m as the reference level. Field strengths above 1 V/m are in light green to red on the color scale. The source is located 1.2 meters from the left end of the plot. The white regions indicate where then field strength is above 20 dB V/m or 10 V/m. The field map indicates that the field strength within the corridor may vary significantly on the planar surface. Field strengths tended to be higher near the centerline of the corridor for most of the corridor length. The structure of the interference patterns tended to become more complex as the distance away from the source increased.

The regions around the source exhibit an interference pattern that is oriented along the side walls, *lateral patterns*, rather than along the length of the corridor, *longitudinal patterns*. As the distance from the source increases, the interference pattern tended to shift from a lateral pattern to a longitudinal pattern. This change started after 5 meters from the source, 6.2 meters along the corridor. When regions further than 20 meters from the source, further than 21.2 meters along the corridor are considered, the interference pattern is mostly aligned along the length of the corridor, i.e. mostly longitudinal patterns. While field strengths tend to be weaker near the side walls than

near the centerline of the corridor there are some regions near the centerline that have relatively weak field strengths.

Trajectory information was obtained by extracting all of the points in the planar surface data file that fall on the trajectory path. The resulting data set has position data and field strength data. An example of the simulated field strength for a centerline trajectory at 850 MHz is shown in figure 2.25. The vertical axis is the electric field strength with a dB scale using 1 V/m as a reference level. The horizontal axis is the distance separating transmitting and receiving antennas, the units are meters and the scale is logarithmic.

While the simulated centerline trajectory data did not exhibit the same deep nulls found in the measured data 2.11, the general behavior of the measured and simulated fields is very close to the measured data. The rate of decrease in simulated field strength is close to that of the measurements.

While the locations of the peaks and nulls differ between the simulated and measured centerline trajectory data, the level of the field strength is close for the measured and simulated centerline trajectory data. The largest differences between the measurements and simulations are found at the nulls, where the measured nulls may be lower than the simulated nulls by more than 20 dB.

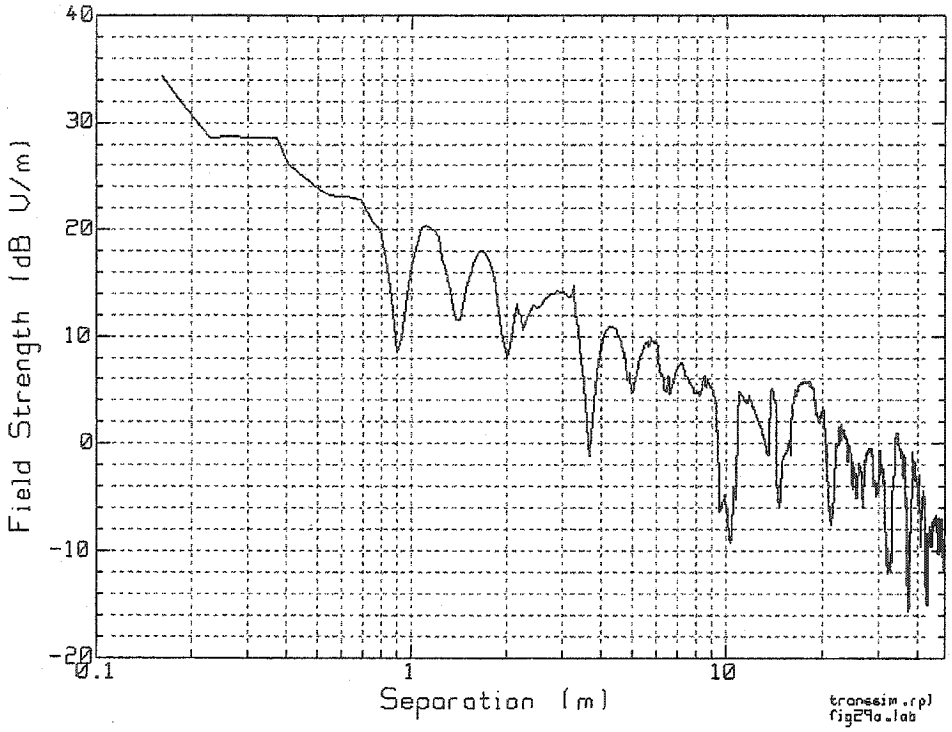

Figure 2.25 Simulated centerline trajectory field strength data for a 600 mW source operating at 850 MHz in 50-meter corridor

2.4.2 Room Simulations

Computer simulations complemented the measurements of fields within the room of section 2.4. Fields within rooms were simulated using the same code as in the corridor simulation. The measurement room was modeled with the source located in the same relative position. The field strength was computed on a planar surface that was analogous to the planar surface in the measurements. The planar surface was divided into a grid of 3.2 cm length squares. The field strength was computed at the center of each square of the grid. The field strength of at the center of the square was used to approximate the field strength for the entire square.

The resulting field data was displayed in the lower plot in figure 2.15 using contour plots with 10 dB between contours. The general structure of the interference pattern of the fields was similar to the measured room fields in the upper plot in figure 2.15. The interference patterns were more clearly defined than in the measurements, possibly due to the averaging of the measurement antenna as well as the rough surfaces of the measurement room. The orientation of the interference patterns with the walls of the room was most pronounced for the walls furthest from the source, which was located near the bottom right hand corner. High field strength regions occurred near the corner of the room furthest from the source as well as other locations within the room.

As in the case of the planar surface measurements, trajectory information may be extracted from planar surface data sets. The same trajectories A and B were extracted from the simulated planar surface data set. The results were plotted in figure 2.17 (a) and 2.17 (b). In the case of the path that moves away from the source, the field strength tends to vary about 12 dB V/m when further than 80 cm from the source. As expected, the field strength increases as the distance from the source decreases. The second path, which is roughly equidistant from the source, has a field strength that varies about 12 dB V/m for most of the length. The interference pattern is not symmetric on path B, perhaps due to the fact that the source is not on an axis of symmetry of the room.

The methods discussed above were used to obtain measured and simulated field strength data that provided information on the behavior, fast and slow varying, of indoor electromagnetic fields. In the following section, the methods used to characterize the data will be described.

2.5 Data Analysis and Characterization Methods

This thesis focuses on medical-device EMI risk assessment, which is the risk of field strength exceeding an immunity level of a medical device. EMC policies based on minimal separations use simplified power law models, such as equation 1-3, to estimate how far medical devices and RF sources must be kept apart so that EMI risk is minimal. However, power law models do not account for variability of the indoor field strength. This implies that the minimal separations based solely on power law models do not account for the variability of indoor fields. In order to correct this shortcoming, the concept of minimal separations with risk (MSR) was developed to include the variability of field strength in minimal separation computation.

2.5.1 Finding the Power Law Model

The power law model, or trend line, is obtained by performing linear regression curve fitting to trajectory data. The process of fitting the curve is as follows: The power law model is converted to logarithmic format shown below [67].

$$E = \log(E_o) - n\log(r)$$

... (2-2)

where E is the logarithm of the electric field strength of the power law model E_o is the reference field strength The relationship in equation 2-2 is fitted to the measured or simulated data by least mean square regression. The square of the difference between the power law model of equation 2-2 and the logarithm of the data points is minimized by the appropriate selection of E_o and n. The difference relationship is shown below:

$$\sum_{i=1}^{M}\left(E' - E\right)^2 = difference$$

... (2-3)

where E' is the measured or simulated data in logarithmic form and M is the number of data points in the set.

The parameters E_o is obtained from

$$E_o = \frac{\sum_{i=1}^{M}\log(E_i') + \sum_{i=1}^{M} n\log(r_i)}{M}$$

... (2-4)

and n is obtained from [27]

$$n = \frac{M\sum_{i=1}^{M}\log(r_i)E_i' + \sum_{i=1}^{M}\log(r_i)\sum_{i=1}^{M}E_i'}{M\sum_{i=1}^{M}(\log(r_i))^2 + \left(\sum_{i=1}^{M}\log(r_i)\right)^2}$$

... (2-5)

The parameters obtained using the above relationship produce a power law model that has the minimum square error, or difference, for the data E'.

Figure 2.26 shows measured 850 MHz data and the trend line obtained using the above process. The parameters of the trend line are: path loss exponent n=0.634 and the reference electric field strength E_o=5.71 V/m. The field strength within two meters of the source, separation of 2 meters or less, tended to be larger than the trend line.

The residual of the measured data and the trend line was then computed. The residual, figure 2.27, was largest near the source and tended to vary around 0 V/m further from the source. While this power law mode is obtained using a least mean square fitting algorithm, the deviation from the data further from the source was less than data near the source.

Further from the source, the field strength tended to vary about the trend line. This behavior was found in the measurement and in the simulation data, the field strength near the source tended to behave according to a different power law model than data

further from the source. The difference in power law models near the source will be discussed in the EMC section later.

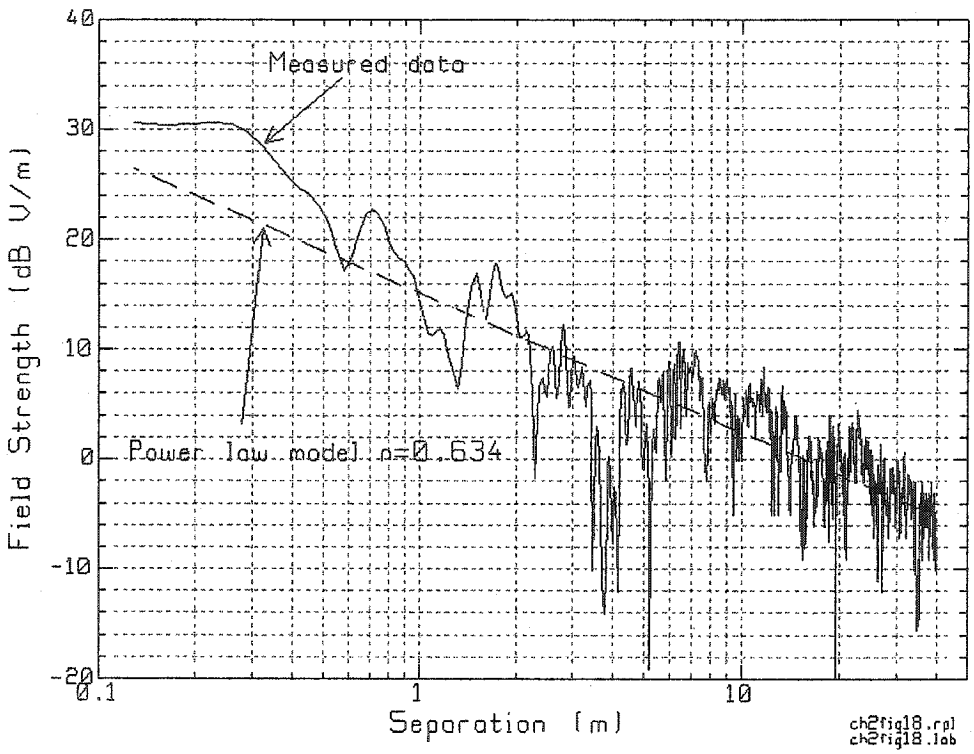

Figure 2.26 Calibrated measured data and associated trend line, regression line, fitted to the data using least mean squares regression. (Location 50-meter corridor)

2.5.2. Characterizing the Residual

Once the trend line has been found, the residual is computed for M data points using [67]

$$X_k = E_k - \frac{E_o}{r^n} \qquad \ldots (2\text{-}6)$$

where E_k is the measured or simulated electric field at point k, k=1,2,...M, and the residual at point k is given by X_k. In this thesis the residual will be in V/m unless otherwise specified.

The residual from the measured data and trend line of figure 2.26 is plotted in figure 2.27. The difference between the data and the trend was largest near the source and smallest near the end of the corridor. The residual tended to vary about 0 V/m, this is due to the fitting process which used least mean square error criteria.

The variability of the residual is greatest near the source; the largest deviation is over 25 V/m. The variability of the residual decreases as the distance from the source increases and for distances greater than 25 meters, the variability is less than 1 V/m.

The residual format used above does not provide EMI risk information in a useful format; the cumulative distribution of the residual data provides a more efficient format for EMI risk computation. The cumulative distribution indicates how many members of the set $\{X_k\}$ are less than a particular value.

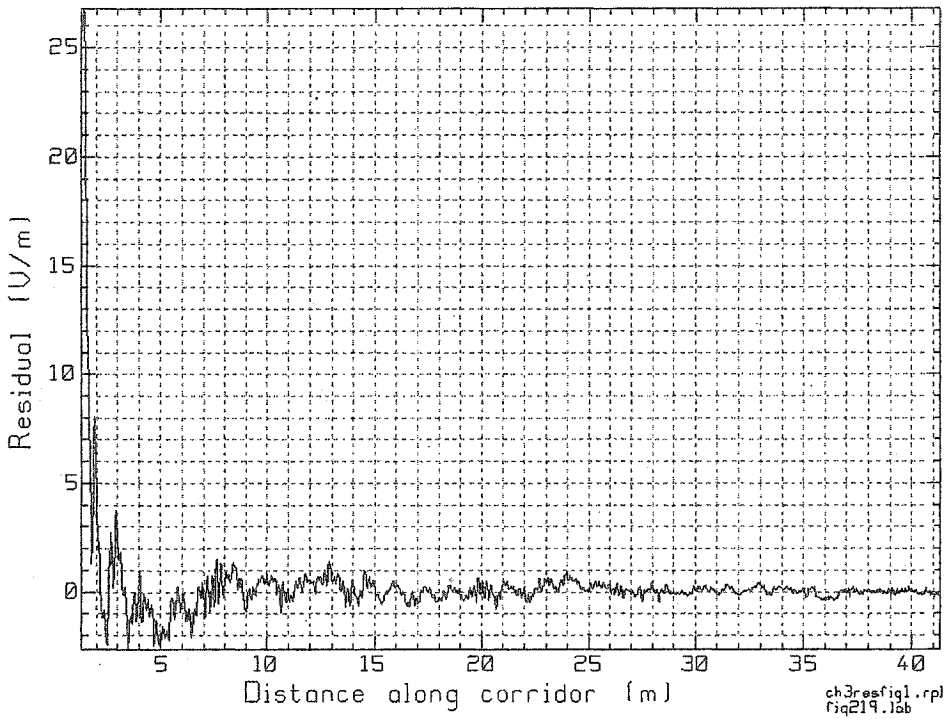

Figure 2.27 Residual of measured data from trend line for 850 MHz measured fields

Using the statistical characterization of fields discussed in chapter 1, the variability of residual field strength is described as a cumulative distribution. This cumulative distribution associates residual field strength with a probability. The distribution of the residual, figure 2.28, indicates that over 95% of the residuals were less than 1 V/m. In field strength terms, the power law model overestimates the field by less than 1 V/m 95% of the time.

2.5.3 Minimum Separation With Risk

The calculation of the minimal separation distance uses the immunity level of the device [46]. This thesis recommends that instead of the immunity level of the device, the separation should use a modified immunity level that accounts for the variability of the field strength. To compute the modified immunity level equation 2-7, the device immunity level is reduced by an amount corresponding to the field variability. The level of risk defines the amount of variability allowed.

$$E_m = E_I - E_{rl} \qquad \ldots (2\text{-}7)$$

Where E_m is the modified immunity level in (V/m), E_I is the nominal immunity level of the equipment and E_{rl} is the risk field strength based on the distribution of the residual.

The following example will illustrate the process: Given a device with a $E_I = 3$ V/m immunity level, compute the minimal separations based on the power law model of figure 2.26. What is the risk of exceeding the immunity level of the device if the field strength varies according to figure 2.28? How far must the device be separated from an RF source so that the risk of exceeding immunity is 5%?

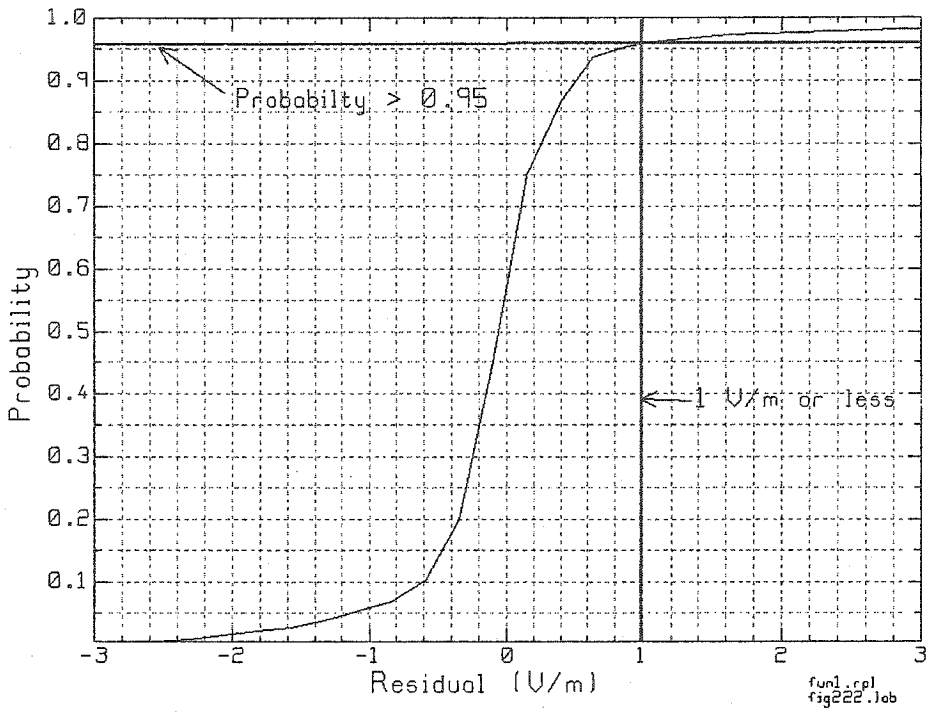

Figure 2.28 Cumulative distributions of residuals from 850 MHz data and associated trend.

The minimal separation distances are obtained using the power law model, or trend line, in figure 2.29. According to the power law model, the source must be kept at least 2.8 meters from the susceptible device in order to insure that the field strength is less than the immunity level. This model does not account for the variation of field strength that is common for indoor environments.

According to the distribution in figure 2.28 residual varies above 0 V/m, the field strength of the trend, approximately 50% of the time. This translates to a 50% risk of exceeding immunity when using the power law model alone. In order to reduce the risk from 50% to 5%, the device immunity level used to compute the minimal

separations must be reduced. From the distribution, the residuals are 1 V/m or less 95% of the time, or above 1 V/m 5% of the time. The minimal separation with risk (MSR) computes the allowed distance between the source and susceptible device using an immunity level reduced according to the variability of the field for a given risk level. In this case, 5% risk is equivalent to $E_{rl} = 1$ V/m variability of field. The immunity level of $E_I = 3$ V/m is reduced by $E_{rl} = 1$ V/m to produce a modified immunity level of $E_m = 2$ V/m. The minimal separation with risk (MSR) of 5% distance is 4.85 meters, according to figure 2.28. At this distance, the risk of exceeding immunity level of the device is 5% since the field strength is 2 V/m according to the trend and the field will exceed 1 V/m only 5% of the time.

By incorporating risk into the minimal separations technique, quantitative evaluation of the potential of EMI is made workable. The older pass/fail criterion fails to address the variability of indoor fields and does not allow for the choice of acceptable levels of EMI risk in hospital EMC policies.

The IEC standard uses an alternate power law model, based on free space propagation. The field strength estimated by a free space model is plotted with measured data in figure 2.30 (a). The residual in figure 2.30 (b) shows that while free space trends provide somewhat better agreement with fields near the source, the residuals for regions farther from the source tend to vary about 1 V/m rather than 0 V/m. This shift in field strength is dependent upon the choice of power law model and the raw data [18].

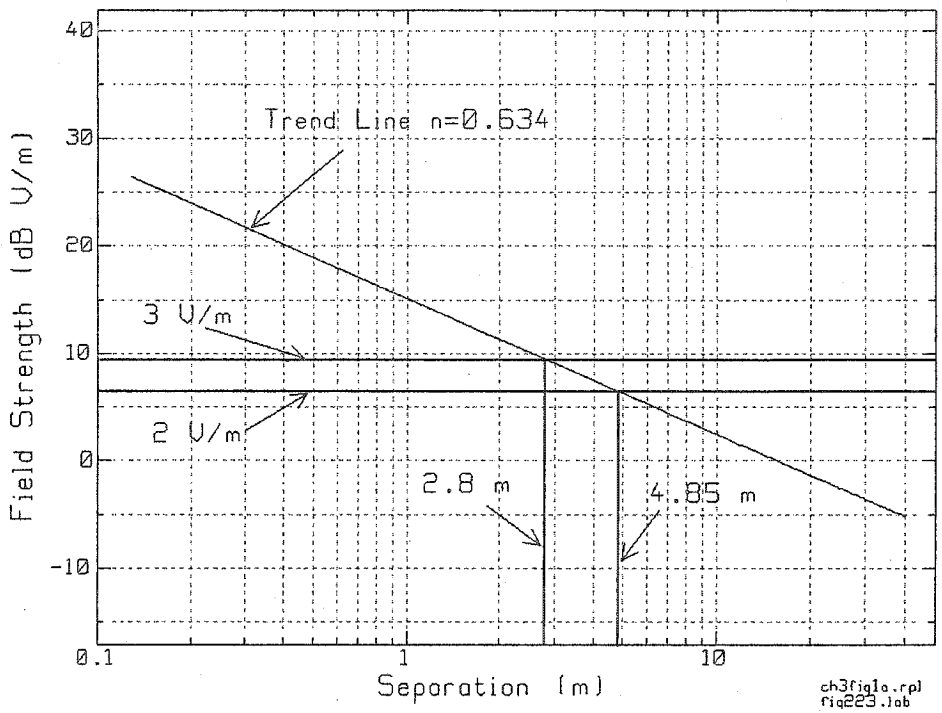

Figure 2.29 Trend line used to determine minimal separation distances for 850 MHz, 0.6 W source.

The shift represents a mean error between the data and power law model, the residual distribution would have a non-zero mean. This mean error must be accounted for in the MSR computation.

In order to better fit the field strength near the source and to maintain as close to zero mean error as possible, a *bi-linear model* was used for MSR computations [23,67, 91]. The bi-linear model used free space power law for locations within one meter of the source and the power law model based on the trend line parameters when further than one meter from the source. The relationship is given by equation 2-8 where the

path loss exponent n and the reference field strength E_o are obtained using the relationships of section 2.6.1.

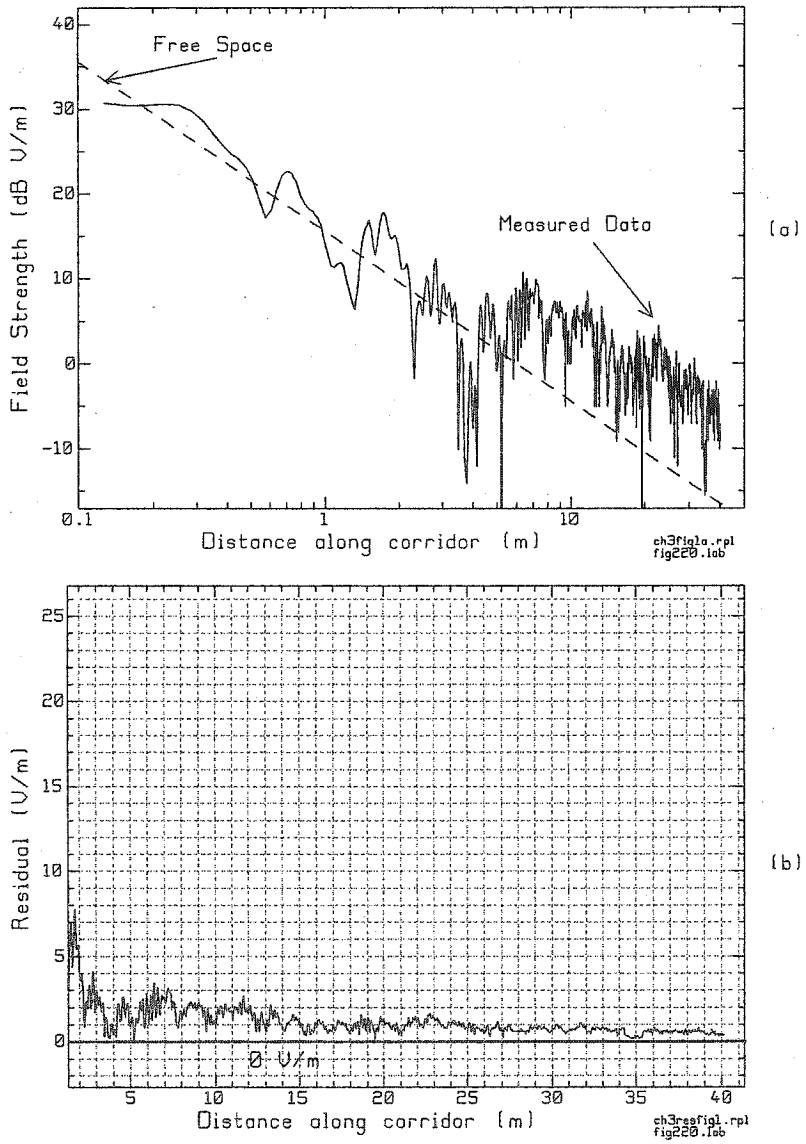

Figure 2.30 Comparison of power law based on free space propagation and measured data (a), residual of measured data and free space based power law (b).

$$\begin{cases} \frac{E_o}{r} & r \le 1 \\ \frac{E_o}{r^n} & r > 1 \end{cases}$$

... (2-8)

The single segment and the bi-linear model are plotted in figure 2.31. The field strength of the bi-linear model is closer to the field strength within 1 meter of the source, further than one meter the two models are the same. This maintains the zero mean error for locations further from the source while providing better agreement with measured data when within 1 meter of the source.

The MSR computations discussed previously will use the 1/distance portion of the model when the separation is within 1 meter of the source and the trend line when the separation is further than 1 meter from the source.

The distribution of the residuals from the trend is used for both segments of the bi-linear model. While the variability of the field is dependent upon distance from the source, most EMI risk locations will be closer to the source where the high variability distribution is required. For this reason the residual of the entire trajectory is used for all MSR and EMI risk computations based on trajectory data.

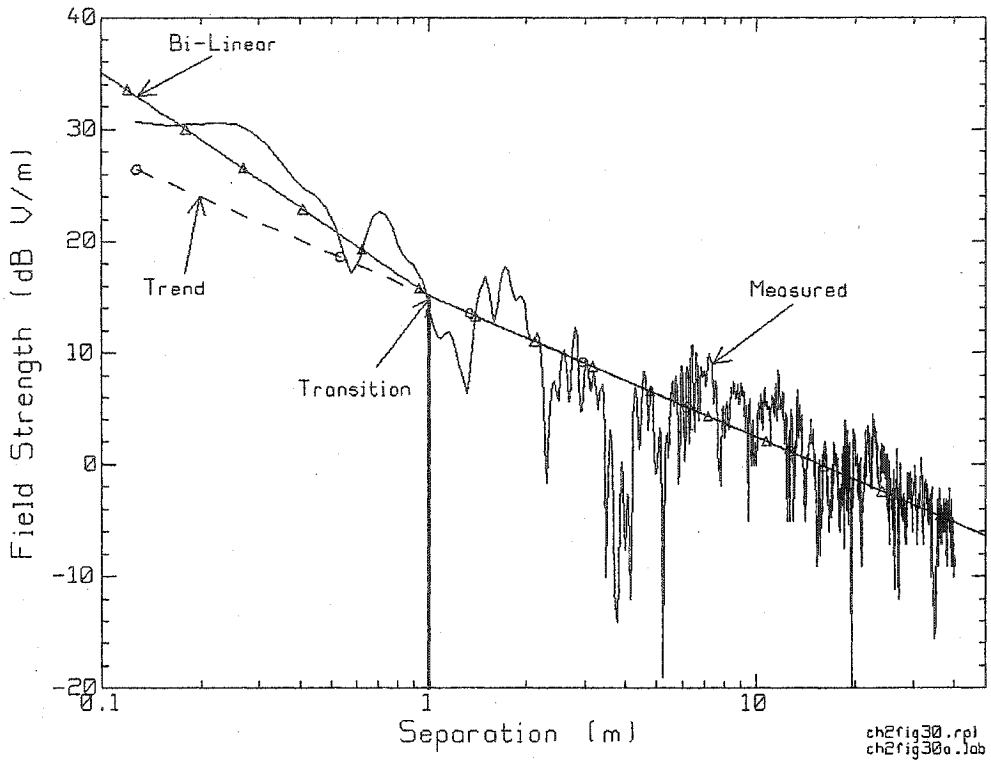

Figure 2.31 Single segment trend line (dashed circles) and bi-linear model (solid triangles) based on measured data (solid). The transition point for the bi-linear model is at 1 meter from the source.

The MSR with 5% risk distance for a device with 3 V/m immunity in the presence of a 600 mW source at 1900 MHz was computed in the following manner. When the actual field strength equals the power law prediction, the residual is zero. The actual field strength is greater than the power law prediction about 50% of the time, as illustrated in figure 2.32. When using an EMC policy with separation distances based only on the power law, not taking into account the field distribution, the actual field strength will exceeding the device immunity 50% of the time. In order to reduce the risk below 50% the minimal separation distance must be larger than that given by the power law. Thus in figure 3.32, for 3 V/m immunity (9.54 dB), the "power law

distance" is 2.5 meters, and it is expected that the field at 2.5 meters will exceed 9.54 dB in about 50% of cases.

Section 3.9.2 presents an example of the computation of an MSR distance for a risk level of 5%, and will be summarized here. Figure 3.21 shows the cumulative distributions of the residuals for trajectory simulations in the 50-meter corridor. By using the cumulative distribution of the residuals, such as figure 3.21, it was determined that 5% of the actual field strength exceeds the power law prediction by 1 V/m or more.

The immunity level of 3 V/m must be modified to account for the variability of the actual field strength. From the distributions in figure 3.21, 5% risk is related to risk field strength of 1 V/m or higher. The modified immunity level is the difference between the actual immunity level and the risk field strength; of 1 V/m. Hence, in this case the modified immunity level is 2 V/m. The MSR distance is computed using this modified immunity level. Figure 2.32 shows the bi-linear power-law field strengths increased by 1 /m as the dashed curve. The MSR distance was found to be 4.85 meters from the source for fields of 9.54 dB or less. At this distance from the source, the actual field strength exceeds the power law only 5% of the time. Thus the field strength is larger than the MSR 5% curve in figure 2.32 at only a few points. The modification of the immunity level is equivalent to adding the risk level to the power law curve, effectively scaling the curve upwards along the Y-axis.

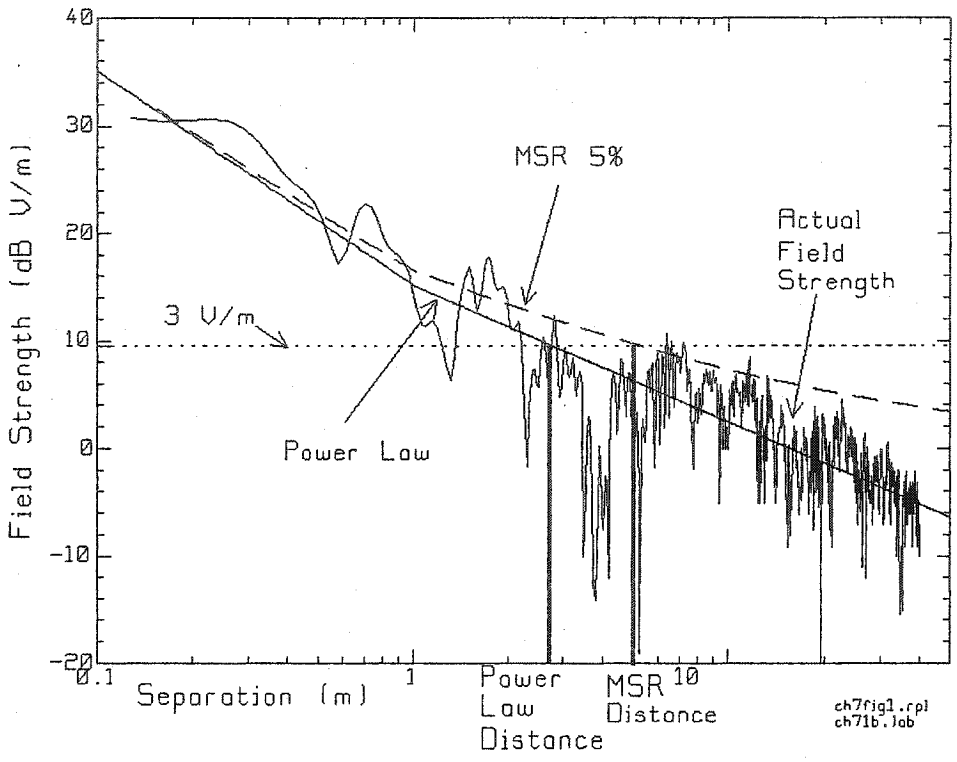

Figure 2.32 MSR with 5% risk and power law separation distances for a device with 3 V/m immunity and an RF source radiating 600 mW at 1900 MHz.

The unmodified power law model crosses the 3 V/m (9.54 dB V/m) immunity level at about 2.5 m. When comparing the power law model to the actual field strength, the actual field strength values are above the power law model about 50% of the time and exceed the immunity level up to 8 meters away from the source. The modified power law curve or MSR curve gave a distance of 5.85 meters; the actual field strength exceeds this curve much less often (5% of the time). The MSR with 5% risk overestimates the actual field strength 95% of the time; providing a more conservative EMC policy that uses more realistic estimates of risk than a binary pass-fail system. The MSR separation distances were from 3-6 meters for 3 V/m immunity and from 0.6 meters to 0.67 meters for 10 V/m immunity from a 600 mW source. The field strength decreased more rapidly near the side walls than near the centerline of the corridor, as a consequence of this behavior the MSR for the same risk level distances

were larger near the centerline of the corridor than near the side walls. It is important to note in order to account for the behavior of the field strength within the corridor volume, the MSR distance also varied with location within the corridor volume. The usage of MSR techniques allows for quantitative comparisons of different EMC policies in terms of effectiveness in quantifying EMI risk in corridors and provides a tool for the biomedical or EMC engineer to decide on the usage of wireless technology within an institution based on quantified risks. This technique might also be used in the design and construction of wireless communication friendly medical institutions by quantifying the EMI risk for a particular structure and policy.

2.5.4 EMI Risk Using Field Distributions

An alternate approach is to compute the risk of EMI directly from the distributions of field strength for the data [19, 20]. This approach was used for planar surface data sets. The distribution was obtained by determining the fraction of the total surface area that contained field strengths within a given range. These fractions were paired with associated the range of field strength. The data set was then sorted in ascending order of ranges of field strength. The cumulative distribution was approximated by this sorted data set.

An example of the distributions obtained using this approach is displayed in figure 2.33, this distribution was computed from the data in figure 2.23. The distribution shown in figure 2.33 indicates that approximately 20% of the surface area, based on the grid of 3.2 cm length squares, has field strength over 10 V/m. The contour plot of field strength, such as figure 2.23 or 2.24, is used to determine the location of regions with a particular field strength range.

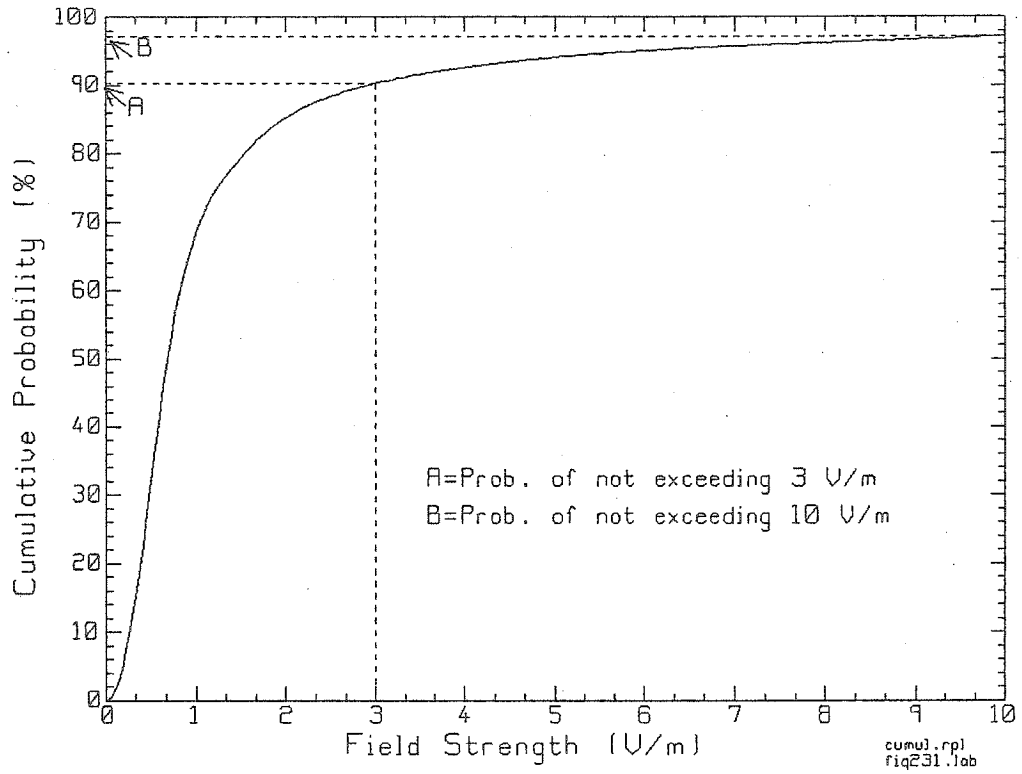

Figure 2.33 Cumulative distribution of simulated fields within corridor at 1900 MHz near wall "A" in figure 2.23

For example, according to the distribution, approximately 88% of the planar surface has field strength in excess of 3 V/m. This information, combined with the planar surface plot of figure 2.23, allows for a numerical value to be assigned to the EMI risk, 88%, and to locate the highest, yellow to white, and lowest risk, blues, regions using the contour plot.

2.6 Relation to Results

In the following chapters, the results the measurement and simulation surveys will be used to produce simplified heuristic models that are used to estimate the hospital

electromagnetic environment. The risk of EMI for different EMC policies is investigated using the novel approach described above. Chapter 3 investigates the EMI risk based on trajectory measurements and simulations within corridors. Chapter 4 uses planar surface simulations to investigate the risk of EMI for more complex data sets. Chapter 5 uses both trajectory and planar surface data to investigate EMI risk within rooms. Chapter 6 uses statistical parameters to approximately determine if a room is electrically "hot" and assess a general EMI risk parameter based on average electric field strength.

Chapter 3

Corridor Trajectories, Path Loss and Statistical Residual Analysis

In this chapter, trajectory data is used to model the rate of field attenuation as a function of the separation distance between the transmitter and receiver. The variability of the data and the distributions of the residuals are examined. The path loss exponent "n" and the reference field strength "E_o" are found. Heuristic models based on these values were used to compute the EMI risk for various minimal separation policies. The dependence of the model parameters on frequency is investigated.

Due to the large number of measurements carried out during the experimental phase of this study and the large data sets computed from the simulation part of this study, a selection of the total data set will be presented in this chapter. The field strengths presented in this thesis were, unless noted otherwise, calibrated using the procedure outlined in section 2.1.2 and normalized to 600 mW. The antennas were vertically polarized for these experimental surveys as described in section 2.2.1. The robot positioner was used for all measurements in this section.

3.1 Centerline Trajectories at 850 MHz and 1900 MHz

The vertical electric field strength due to an RF source radiating 600 mW at 850 MHz and 1900 MHz was measured along the centerline of the corridor. The measurement in figure 3.1 was representative of the results of measurements taken on nine floors of the hospital data for 850 and 1900 MHz. The vertical axis of the graph shows the electric field strength in dB relative to 1 volt per meter. The horizontal axis of the

graph is the separation distance between the transmit and the receive antenna in meters on a logarithmic scale.

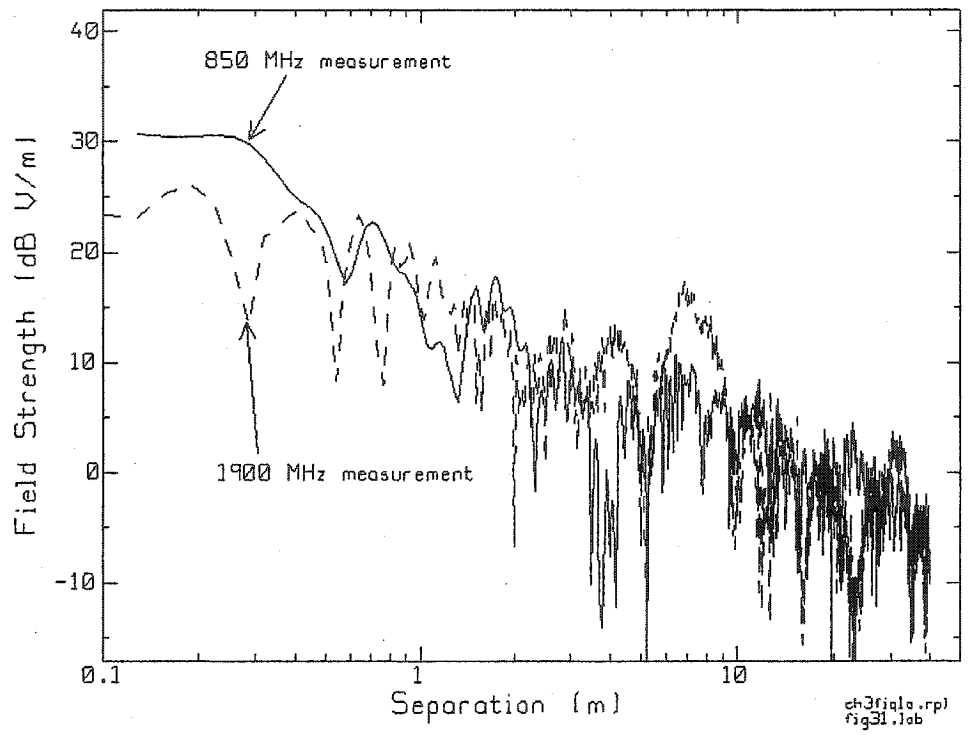

Figure 3.1 Corridor centerline trajectory on the 9th floor of the old wing at 850 and 1900 MHz.

The field strength decreases with separation at somewhat different rates for the two frequencies. As might be expected, interference patterns at 1900 MHz generally exhibit more structure than at 850 MHz measurements. The location of the peaks and nulls of the interference pattern was different for the various corridors but the rate of attenuation of the field strength with distance was consistent for the various corridors at each frequency.

3.1.1 Trends of Fields for 850 MHz and 1900 MHz

The term "trend" will be used to describe the rate of decrease in the field strength with distance from the source, and is quantified by the path loss exponent "n" of equation 2-5. For each trajectory measurement or simulation the value of the path loss was found by linear regression using the methods of section 2.6.

The trends for the two curves of figure 3.1 are plotted in figure 3.2. At 850 MHz, the path loss exponent is 0.63 while at 1900 MHz it is 0.71. While the path loss exponents are different for the two frequencies, the range of field strengths is close, within 5 dB for most of the corridor length. The value of the path loss exponent is not strongly sensitive to the spatial sampling rate [22], but may vary with the frequency as demonstrated by this figure.

The path loss exponent differs by about 14 % for the 850 MHz and 1900 MHz centerline trajectories. It is interesting to note that while the 850 MHz trajectory data in figure 3.1 has higher field strength values within 40 cm of the source, when compared to the 1900 MHz measurements, the 850 MHz trend has lower field strength estimates than the 1900 MHz trend when within 40 cm of the source. This is an artifact of the regression fitting for the entire corridor length with a single line. The regression line fit is better when further than 1 meter from the source.

The field strength within 1 meter of the source tends to attenuate at the same rate as in free space. This behavior will be used later in the EMC analysis section.

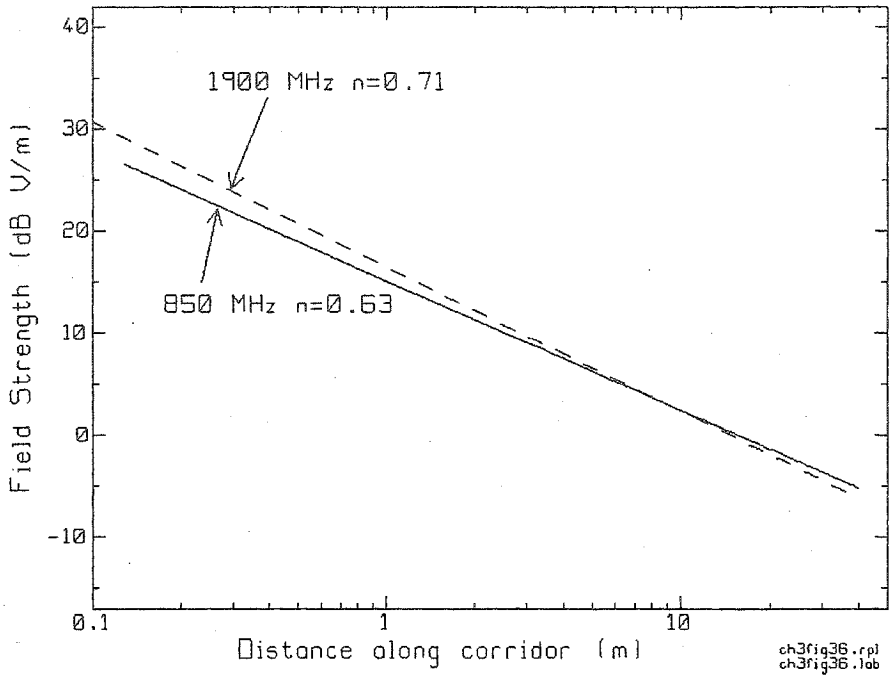

Figure 3.2 Comparison of the trends for measured data at 850 (solid) and 1900 (dashed) MHz for single trajectory along the centerline of corridor

Table 3.1 suggests that densely sampled points lead to a smaller range of path loss exponent values than widely spaced data points. But this might be misleading because the 1562-point data set was all taken on the same floor, whereas the sparser data sets were taken on various floors of the hospital. In almost all of the cases, the path loss exponent is smaller than n=1 for free space, indicating that the average value of the field strength declines more slowly than in free space. Also the range of values for the path loss exponent for the data sets taken on more than one floor is quite large.

Table 3.1

Path loss exponents for centerline measurements within 50-meter hospital corridors at 850 and 1900 MHz. * Denotes measurements on one floor only.

Frequency (MHz)	n	# Trials	Number of data points per trial
850	0.6-0.7	8 *	1562
850	0.55-1.0	27	160
850	0.6-0.9	18	50
1900	0.7-0.9	4*	1562
1900	0.8-0.9	12*	160
1900	0.26-0.64	18	50

3.1.2 Residuals of Fields at 850 MHz and 1900 MHz

Once the reference field strength E_o and the path loss exponent n have been found using linear regression, the residuals are computed using equation 2-6. The cumulative distribution of the residuals is found using the methods outlined in section 2.6.2. The cumulative distributions of the residuals of the measured data at 850 MHz and 1900 MHz are plotted in figure 3.3. The differences between the distributions at these two frequencies are most pronounced in the portion of the residual that is between 1 and 2 V/m. The greatest difference between these residuals is approximately 8%. The 850-MHz residual is less than 1 V/m for roughly 95% of the data, while the 1900-MHz residual is less than 1 V/m for roughly 90% of the data. In both cases, over 95% of the residual data is less than 3 V/m.

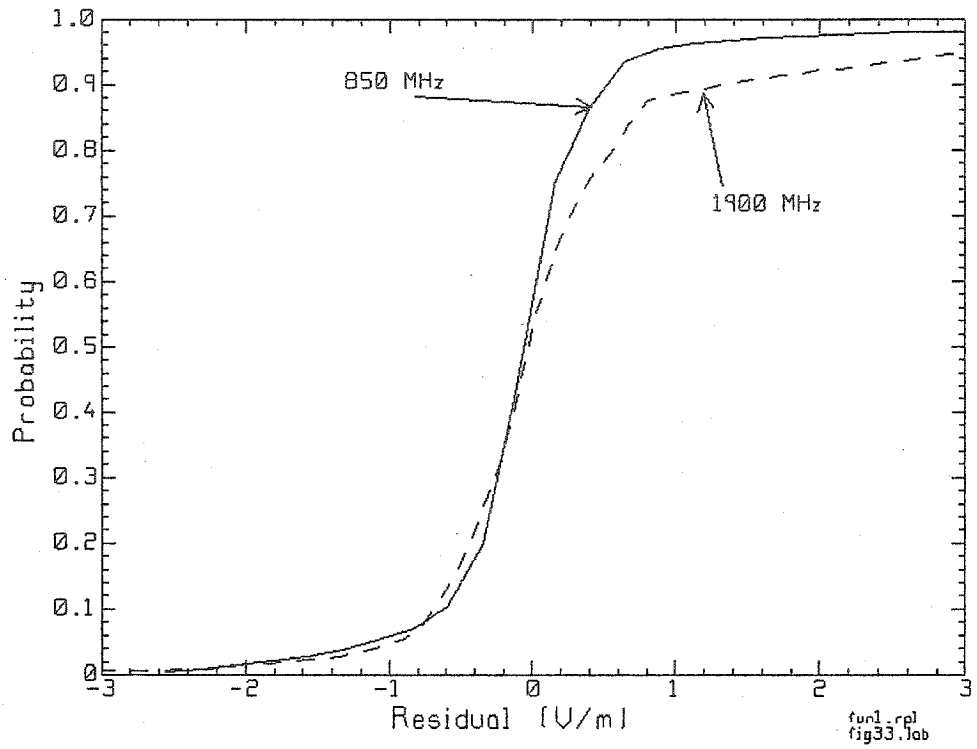

Figure 3.3 Distribution of residuals for corridor centerline trajectories at 850 MHz and 1900 MHz.

The trend can estimate the field strength along the corridor centerline as a function of separation between the source and the transmitter. This relationship will be used in the next section to compute minimal separations. The residual distributions will be used to predict the probability that the field strength will exceed the value provided by the trend. This probability is related to the risk of radiated EMI based on the immunity level of a victim device.

3.2 EMI Results for Centerline Trajectories at 850 and 1900 MHz

The field strength was estimated using equation 2-8. The field strength for locations within 1 meter of the source were estimated assuming free space propagation while locations further than 1 meter from the source were estimated using the trend of the

data. These relationships are plotted in figure 3.4 in comparison of the free space and IEC based models. The field strength predicted by free space propagation is lower than the other trends at all points along the corridor. The field strengths predicted assuming the IEC standard are higher for the entire length of the corridor, because of the $^{10}/_{3}$ factor in the IEC model. The rate of attenuation for the measured trends is less than that of free space and the IEC relationship.

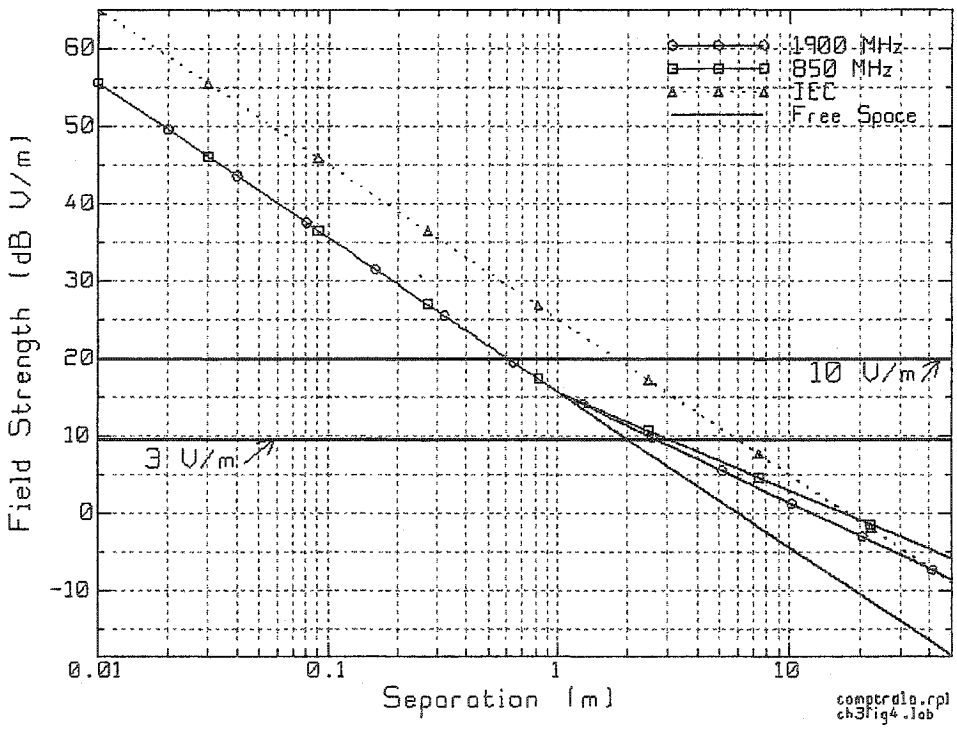

Figure 3.4 Bi-linear relationships used to compute minimal separations for a 600 mW source based on measured data compared with free space and IEC relationships used to compute minimal separations.

For a device with immunity of 3 V/m, 9.54 dB V/m, the minimal separation distance at 850 MHz is listed in table 3.2. While the minimal separation distance at 1900 MHz is listed in table 3.3. These distances were computed from figure 3.4. Assuming free

space propagation, the minimal separation distance is 1.8 meters from the source. Using the IEC standard, the device must be kept further than 5.9 meters from the source at both frequencies. Using the path loss exponent n=0.63 for 850 MHz, the minimal separation in figure 3.4 is 2.2 meters. Since about half of the measured data lies above the trend line derived by linear regression and about half lies below the trend line, there is a 50% risk that the field will exceed the immunity level of the device at 2.2 meters separation. Hence the term "minimal separation with risk" or MSR will be used for this distance. Given the risk of 50%, the MSR distance is 2.2 meters. To get a MSR distance with a 5% risk, consider the distribution of figure 3.3.

The 95% level on the distribution of the residual intersects the 1 V/m level, hence there is only a 5% risk that the field exceeds the trend by 1 V/m or greater. Modify the immunity level of the device by subtracting the "risk level" of 1 V/m to get the "modified" immunity level of 2 V/m or 6.02 dB V/m. The solution to the power law relation of equation 2-8 provides a separation of 5.7 meters, as shown in figure 3.4. Thus if the equipment is 5.7 meters from the source there is only a 5% or smaller risk that the field will exceed the trend line. The "minimal separation with risk" MSR at 5% risk is 5.7 meters. For the 1900 MHz data set, using a 2 V/m modified immunity level corresponded to a 10 % risk of exceeding the immunity level. The MSR depends on the risk level, the device immunity and the frequency.

From table 3.2, the IEC standard required that the minimal separation be 4.2 meters from a transmitter radiating 300 mW; which is about 2 meters further than the MSR predicted distance of 2.3 m at 5% risk. When the power level was increased to 600 mW, the minimal separation distance recommended by the standard is 5.9 meters; this was again greater than the MSR distance of 5.7 meters at 5% risk. In all cases the minimal separations based on free space were smaller than those produced by the

other models. The distances computed using free space recommendations have more than 50% risk of exceeding the device immunity level. Figure 3.4 suggests that the risk associated with the large IEC MS distances is much smaller.

Table 3.2

MS and MSR distance assuming 3 V/m immunity device using 850 MHz data.

Transmitter Power	MS Distance		MSR Distance	
	Free Space	IEC	50% risk	5% risk
300 mW	1.3 m	4.2 m	1.7 m	3.0 m
600 mW	1.8 m	5.9 m	3.0 m	5.7 m

Table 3.3

MS and MSR distance assuming 3 V/m immunity device using 1900 MHz data

Transmitter Power	MS Distance		MSR Distance	
	Free Space	IEC	50% risk	10% risk
300 mW	1.3 m	4.2 m	1.7 m	2.9 m
600 mW	1.8 m	5.9 m	2.7 m	4.6 m

The same process was used to compute the MS and MSR distances for a device with 10 V/m immunity level. The 850-MHz results are in table 3.4 and the 1900-MHz results are in table 3.5. The resulting separations are of the order of a half-meter for both the MS and MSR. The IEC-based distances are three to four times larger than the separations computed using the other models. When within 1 meter of the source, all of the models use n=1 for the path loss exponent. With the 10 V/m immunity associated with newer hospital equipment, the separation distances of tables 3.4 and 3.5 are much smaller than those of 3 V/m when wireless devices are intended to be

used closer to patients and critical care equipment. Distances for 5% risk are about 40 cm.

Table 3.4

MS and MSR distance assuming 10 V/m immunity device using 850 MHz data.

Transmitter Power	MS Distance		MSR Distance	
	Free Space	IEC	50% Risk	5% Risk
300 mW	0.38 m	1.26 m	0.38 m	0.43 m
600 mW	0.6 m	1.8 m	0.6 m	0.68 m

Table 3.5

MS and MSR distance assuming 10 V/m immunity device using 1900 MHz data

Transmitter Power	MS Distances		MSR Distance	
	Free Space	IEC	50% risk	10 % Risk
300 mW	0.38 m	1.26 m	0.38 m	0.43 m
600 mW	0.6 m	1.8 m	0.6 m	0.68 m

In this section the centerline trajectory-based model has been used to predict field strength and EMI risk within a corridor. The question of whether centerline measurements are representative of field behavior over the entire corridor volume must now be addressed. Measurements along multiple trajectories within the corridor volume will now be presented.

3.3 Volume Scan Measurements

A volume scan was performed using off-center trajectories with 30 cm sample spacing and a 1900 MHz source. The results of the scan are shown in figure 3.5. While the general trends are observable in figure 3.7, the density of the data and the structure of the field make the identification of the behavior of any particular trajectory problematical. In order to investigate the behaviors of particular trajectories, the data was plotted according to height above the floor.

The data from trajectories taken at 207, 120 and 30 cm above the floor are plotted in figure 3.5 (a), (b) and (c) respectively. While the location of maxima and minima differed between individual trajectories, the general behavior of fields at each height was similar.

For the measured fields taken at 120 and 207 cm, figure 3.5 (b) and 3.5 (a) respectively, above the floor, certain common characteristics were observed. Field strengths further from the source tended to display greater variability and to decrease at a slower rate with separation. The field strength dropped more rapidly when close to the source and tended to have less variability when close to the transmitter. This behavior was similar to that of the corridor centerline trajectory measurements in figure 3.1. Since the spacing between measurement points along a particular trajectory was 32 cm, as opposed to 3.2 cm for the centerline trajectories, the figures 3.5 (a), (b), and (c) lacked some of the detail and smoothness of the centerline trajectory measurements.

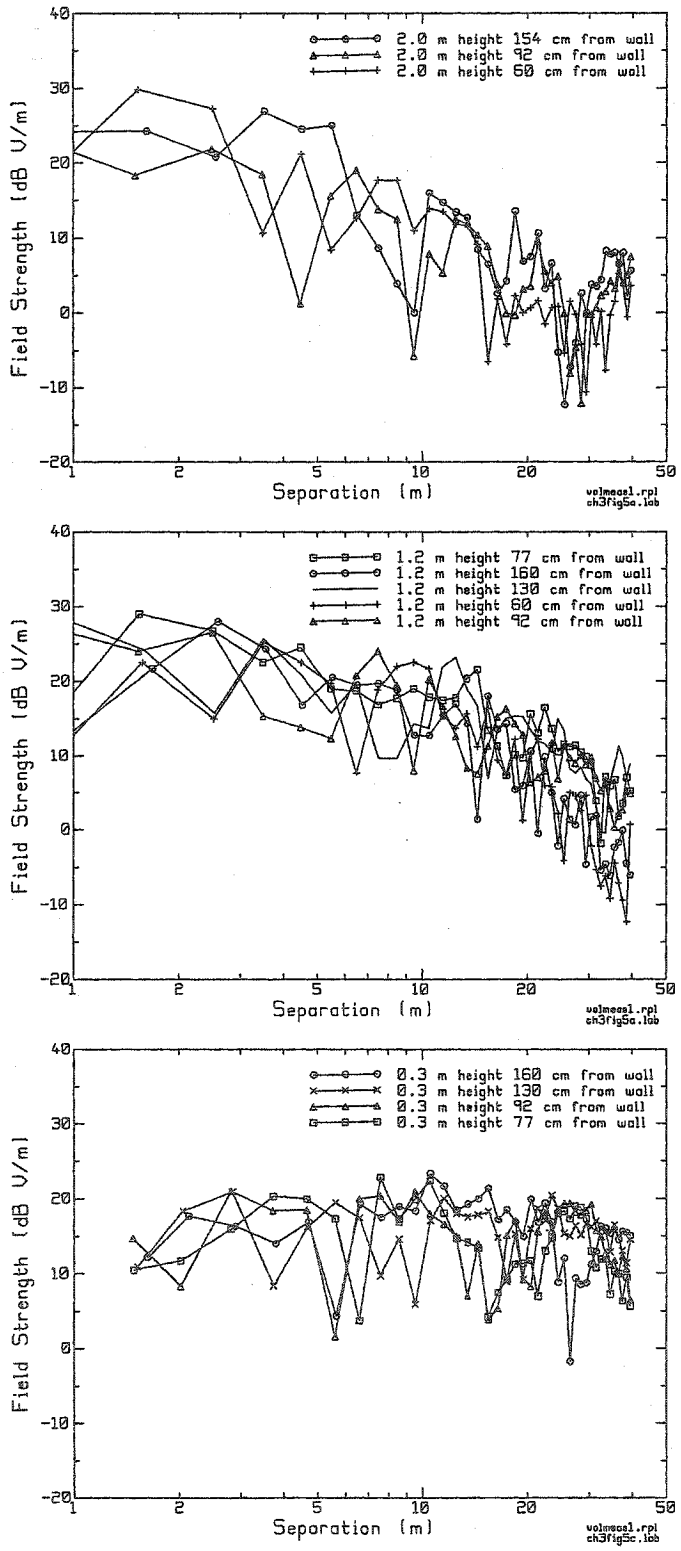

Figure 3.5 (a)-(c) Field strength measurements at 1900 MHz in 9th floor corridor.

The field measurements for the region 30 cm above the floor are shown in figure 3.5 (c). Unlike the previous measurements, the fields at 30 cm above the floor varied around a level that was nearly constant. The variation was around 10 dB. The fields tended to be weaker than the previous measurements when close to the source and varied around the 15 dB V/m level for the entire length of the corridor. This behavior occurred when both the source and receive antennas were vertically polarized. When the receive antenna was aligned parallel to the floor, to receive horizontally polarized field components, the rate at which the field strength decreases is comparable to rate of measured fields at 120 and 207 cm above the floor. Figure 3.6 compared the field strength and respective trends of trajectory measurements taken at 30 cm above the floor parallel to the corridor centerline.

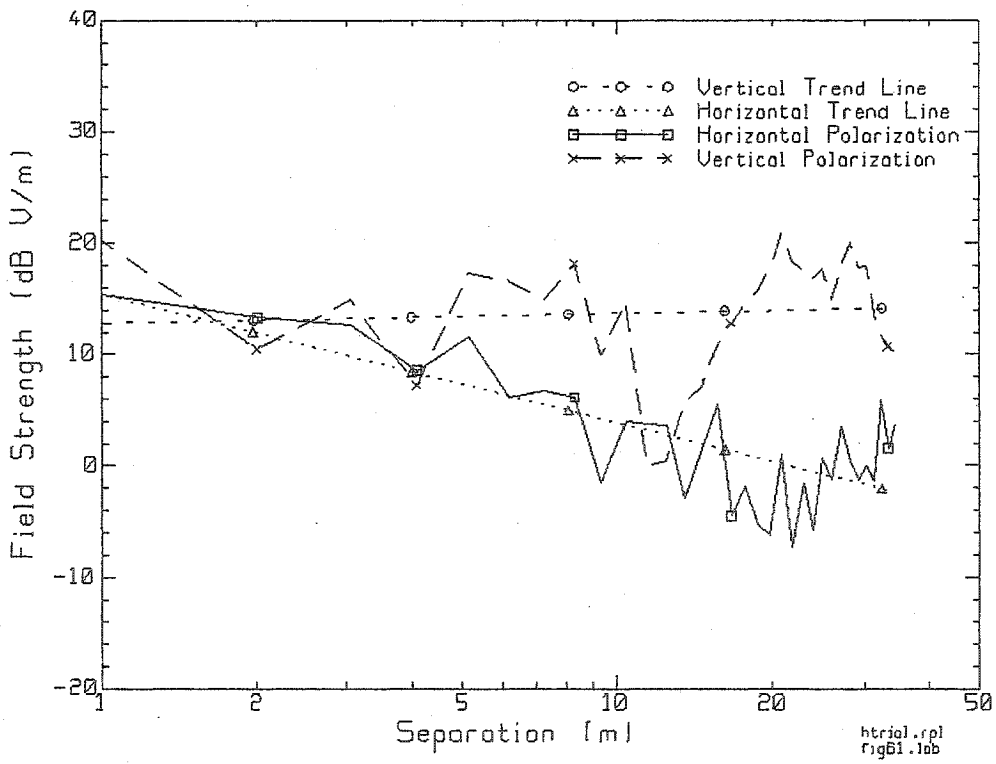

Figure 3.6 Comparison of vertically and horizontally polarized field measurements at 30 cm above floor. Source antenna is vertically polarized in all cases.

The vertically polarized fields as in figure 3.5 (c) vary from 0 to 20 dB V/m but show very low rates of decrease in field strength with separation from the source. The path loss exponent of the vertical trend is n = 0.0435. The horizontally polarized fields exhibit, in contrast to the vertically polarized fields, a rate of decrease in field strength with source separation closer to those of figures 3.5 (a) and 3.5 (b). The field strength begins at 15 dB V/m and decreases to approximately 0 dB V/m near the end of the trajectory. The path loss exponent of the horizontal trend is n = 0.60.

While constant field strength in cross-floor [89] and through building field measurements [9] have been reported, vertically polarized field strength near the floor that does not attenuate with separation from the source is unanticipated and previously unreported behavior [24]. This indicates that the field behavior near the floor is substantially different from behavior along the corridor centerline. As a consequence, models based solely on data obtained from corridor centerline measurements would not accurately predict field strength near the floor.

The structure of the interference pattern in figure 3.5 (c) is consistent for the entire corridor length where the peak and null values are generally at the same level for the entire trajectory. While the field strength begins at smaller values than the trajectories taken at heights higher than 30 cm above the floor, the field strength at the end of the corridor is higher for the 30 cm measurements than for the greater heights. This previously unreported behavior indicates that there may be different propagation mechanisms operating near the floor. Low, nearly constant, field strength near the floor that does not attenuate appreciably with distance would make minimal separations problematic if the source power was large or if there were multiple sources. The implications for EMC and for communication coverage will be discussed in more detail later in this thesis.

The trends for the off-centerline trajectories at 120 and 207 cm above the floor are plotted in figure 3.7 (b) and 3.7 (a) respectively. The path loss exponent for the trajectories varies for each path within the corridor volume. The paths near the corridor centerline tend to have smaller path loss exponents than those paths closer to the side walls of the corridor. The general behavior of the trends and the rate of field strength attenuation for the 120 and 207 cm trajectories are similar to those of the corridor centerline shown in figure 3.2. By contrast, the trend lines for the region 30 cm above the floors, figure 3.7 (c), tend to remain at a nearly constant level for the entire length of the corridor. While the trend lines at 30 cm above the floor begin at smaller field strengths, they are the larger near the end of the corridor than field strengths at the other heights. The slopes of the trend lines at this height are much less than the slopes of the trend lines for the higher regions. There are variations in the slope of the different trends; these will be discussed in more detail later in the thesis.

3.3.1 Residuals of Volume Scan Measurements

The variability of the measured field strengths of the data from the multiple trajectory measurements is obtained from the residuals. This process is the same as in the case of the single trajectory measurements and is described in detail in section 2.6. The residuals will be grouped according to the height of the trajectory above the floor. The trajectories taken at 207 and 120 cm above the floor are plotted in figure 3.8 (b) and (a) respectively, while the residuals of the 30 cm above the floor trajectory data are plotted in figure 3.8 (c).

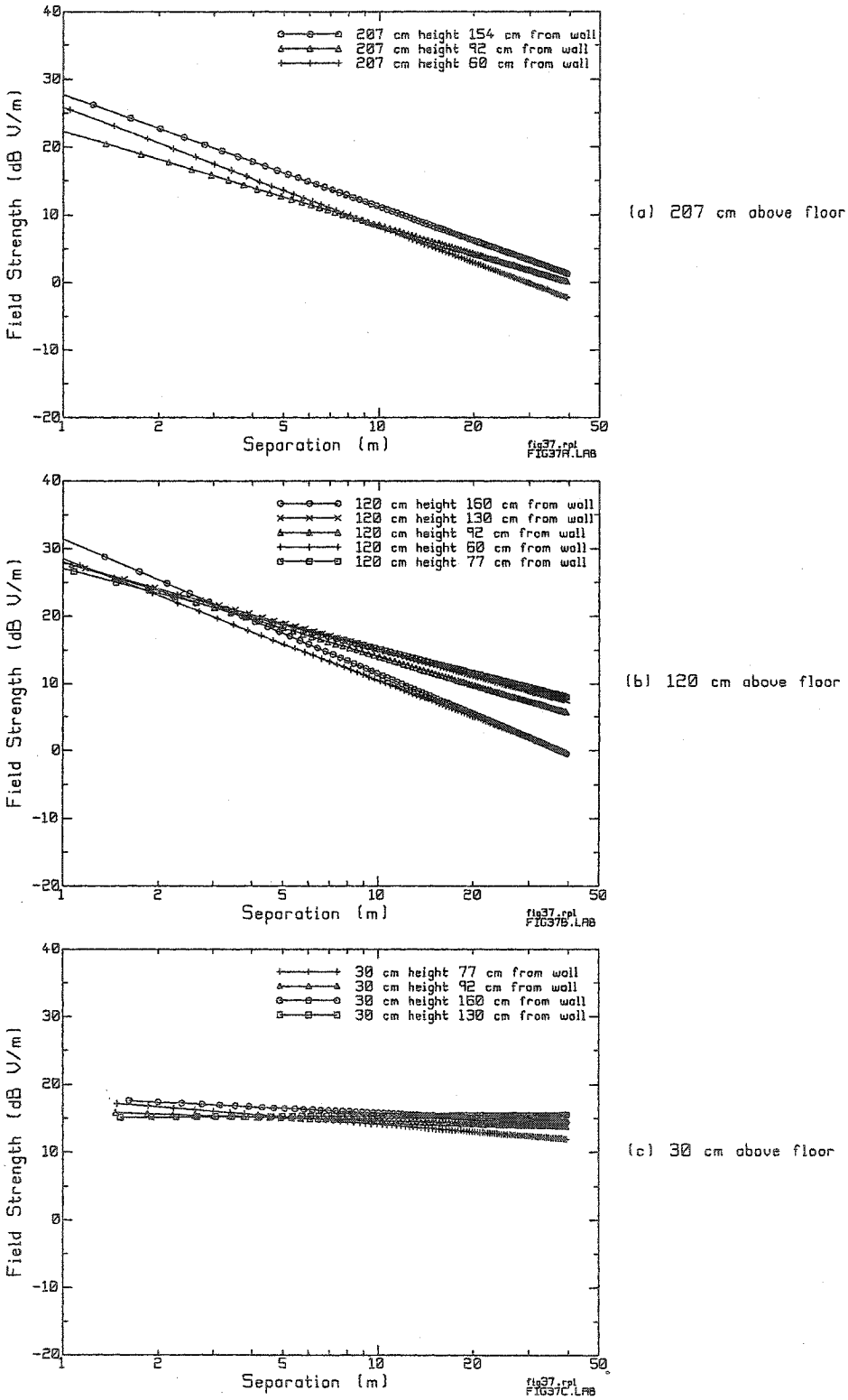

Figure 3.7 (a)-(c) Trends of measured data for at 1900 MHz in 9th floor corridor.

The distributions in figure 3.8 are based on 32 cm spacing between measurements; this lower spatial sampling rate caused a higher variability in the residual. The higher variability in the residuals requires a wider range in the distribution plots. For this reason, the distributions from –5 to 5 V/m are plotted rather than the –3 to 3 V/m range used for the centerline trajectory. The proportion of the residual that is less than 5 V/m varies from 85 to 95 %. The trajectories closest to the centerline of the corridor have less variation than the trajectories closer to the side walls.

In comparison, the residuals of the distributions for the measurements taken at 30 cm above the floor have distributions that vary almost linearly for the range from –5 to 5 V/m. This behavior contrasts strongly with the other residuals obtained above.

There are marked differences in both the trends and the distribution of the residuals for trajectories were taken at 30, cm above the floor when compared to the trends and distributions for trajectories taken at 120 and 207 cm above the floor of the corridor. The next section will compare the data for three trajectories the same distance from the side wall but taken at different heights.

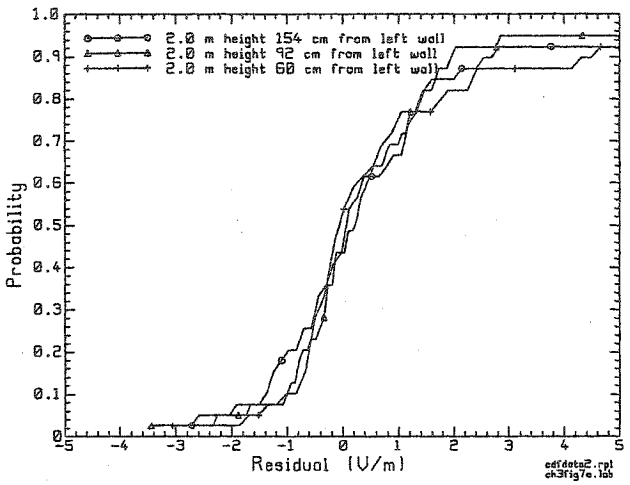

(a) 207 cm above floor

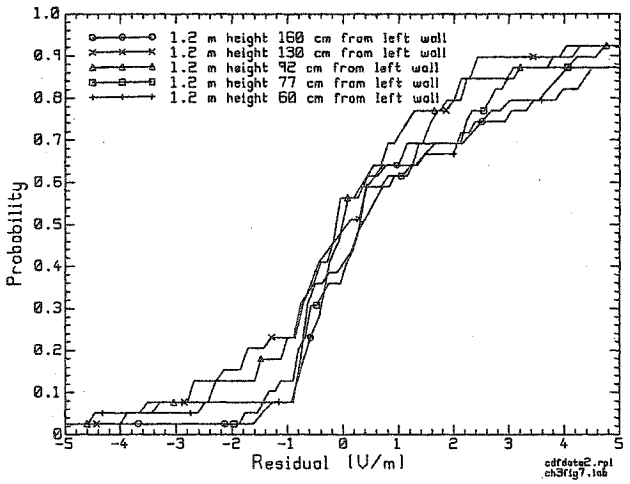

(b) 120 cm above floor

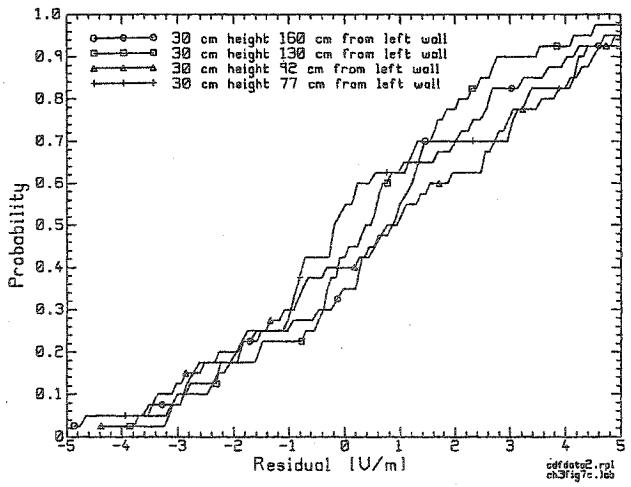

(c) 30 cm above floor

Figure 3.8 (a)-(c) Cumulative distributions of residuals of measured data and trends taken cm above corridor floor

3.4 Comparison of Measurements for Multiple Trajectories

Figure 3.9 compares the power law relationship or trend at 92 cm from the wall at heights of 30, 120 and 207 cm. The trends for the 120 cm and 207 cm heights have similar slopes, but the 207-cm. height trajectory has a lower field strength. This shift in field strength might be caused by the radiation patterns of the transmitter and receiver. In contrast, the trend for the trajectory at 30 cm height remains nearly constant at 5 dB V/m for the entire length of the corridor. This trend begins lower than the other two, but by the end of the corridor has the largest field strength. The 30 cm height trajectories all have similar trends, and often have the strongest fields at the end of the corridor furthest from the source.

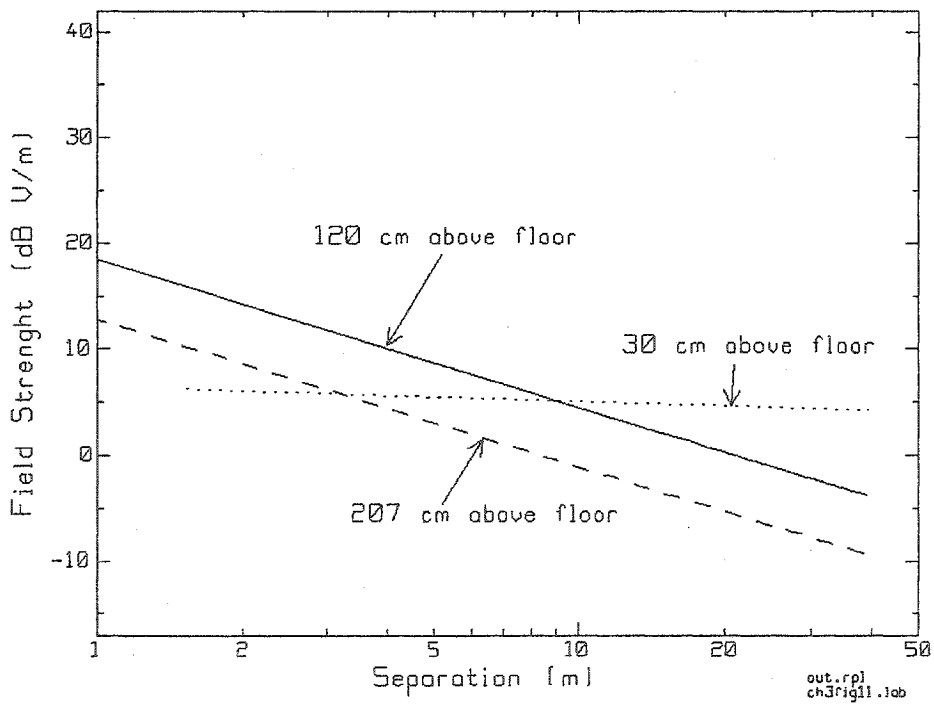

Figure 3.9 Comparison of trends for locations 92 cm from left wall at 30 (dotted), 120 (solid), and 207 (dashed) cm above the floor

The distributions of the residuals are compared in figure 3.10. The distributions are not as smooth as the distributions of the centerline residuals; this is partially due to the wider spatial sampling of the off-centerline trajectories. The distributions for the 120 and 207 cm heights have at least 60% of the residual data within –1 V/m to 1 V/m. The general shape of these distributions is close despite the low sampling rate. The 30 cm residual distribution is quite different in shape when compared to the previous two cases. The approximately straight-line slope of this distribution is suggestive of a uniform distribution rather than the "S" shaped distributions previously encountered. The proportion of the residual within the range –1 V/m to 1 V/m is approximately 20%. From the raw data, trends and distributions the fields at 30 cm above the floor behave differently than fields in locations at 120 and 207 cm above the floor in the corridor.

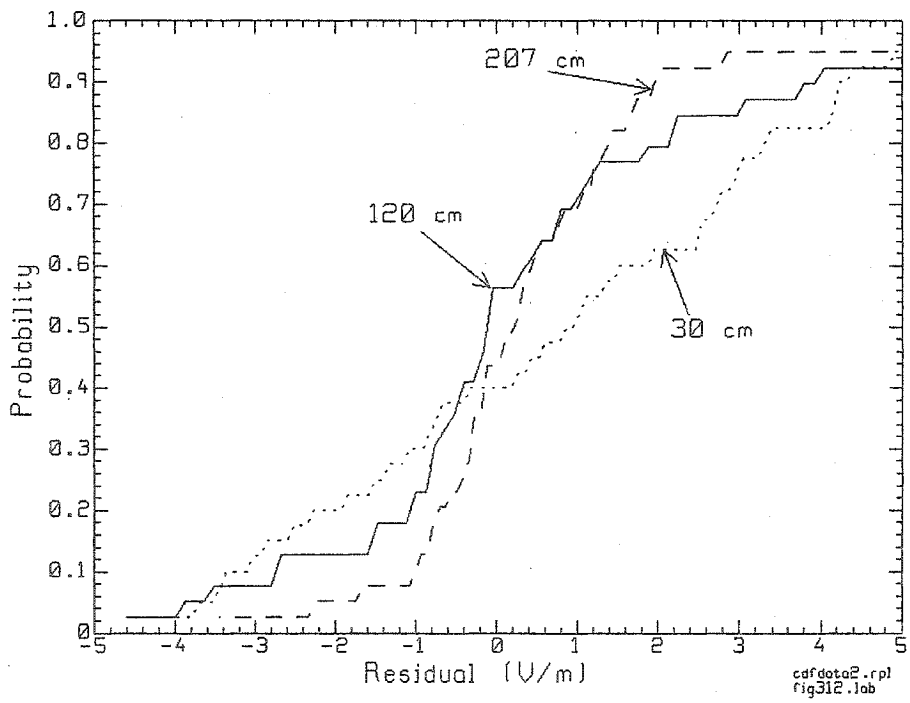

Figure 3.10 Comparison of distribution of residuals for locations 92 cm from left wall at 30 (dotted line), 120 (solid line), and 207 (dashed line) cm above the floor

3.4.1 Path Loss Exponent

The path loss exponent is not constant within the corridor volume. To better view the relationship of path loss exponent as a function of location within the corridor cross-section, the path loss exponent for different height trajectories is plotted as a function of distance from one side wall of the corridor in figure 3.11, which illustrates certain characteristics of the path loss within the corridor. First, the path loss exponent is almost always less than the free space path loss exponent. Second, the path loss exponent is smallest near the centerline of the corridor.

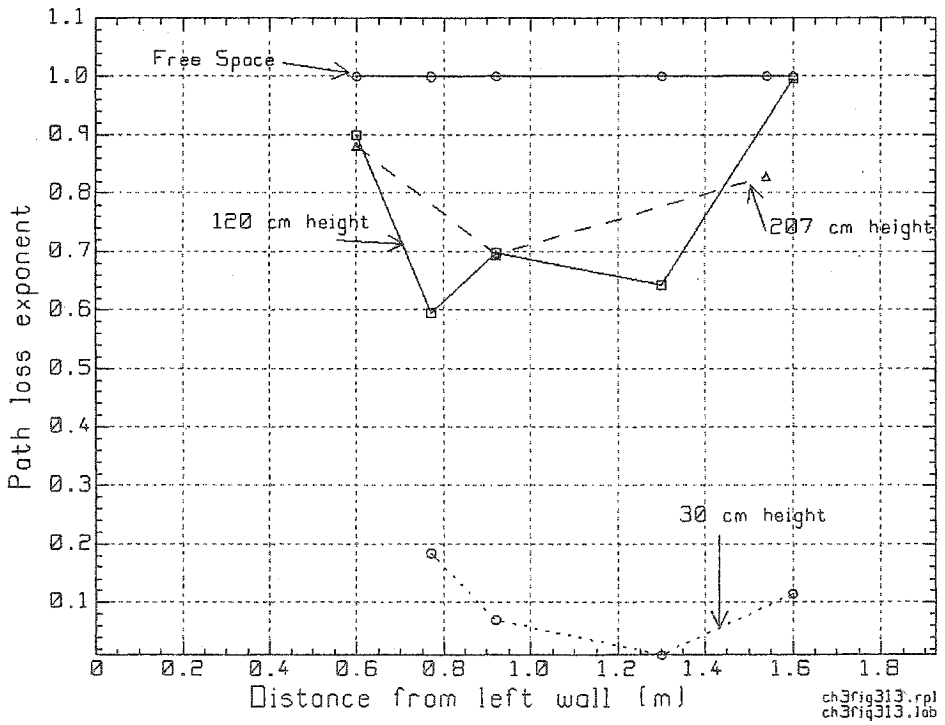

Figure 3.11: Path loss exponents for trajectories at: 207 cm height, (dashed triangle), 120 cm height (solid square), 30 cm height (dotted circle) and Free space (solid circle)

Third, the path loss exponent is much smaller for locations 30 cm above the floor. The path loss exponent near the centerline of the corridor at 30 cm above the floor is very nearly zero for a 50-meter corridor, this implies nearly no loss in field strength along the corridor length.

The lower rate of attenuation near the middle of the corridor is consistent for all three heights of measurements. The rates of attenuation for trajectories at 120 and 207 cm is very close for all distances from the side wall. The rate of attenuation of the field strength near the floor, 30 cm height, is very low. This behavior might indicate a form of guided surface wave that is bound to the floor surface.

Using the information about the field behavior within the corridor volume, the risk of EMI was quantified using a process similar to that of section 3.2 as described in the following sections. The measurements within the volume had a lower spatial sampling rate than the single trajectory measurements; this caused the confidence level to decrease from 95% to 85 % for the same 1 V/m range of data.

3.5 EMC Assessments for Coarse Volume Measurements

This section presents minimal separations computed using the path loss exponents for paths at 30, 120 and 207 cm and at 66, 77, 92, 130, 154, and 160 cm from the side wall. As discussed in section 3.2, the field is modeled using equation 2-8, where *Eo* is the reference field strength, in this case the field strength 1 meter from the source assuming free space propagation, and n is the path loss exponent computed from the measured data using equation 2-5.

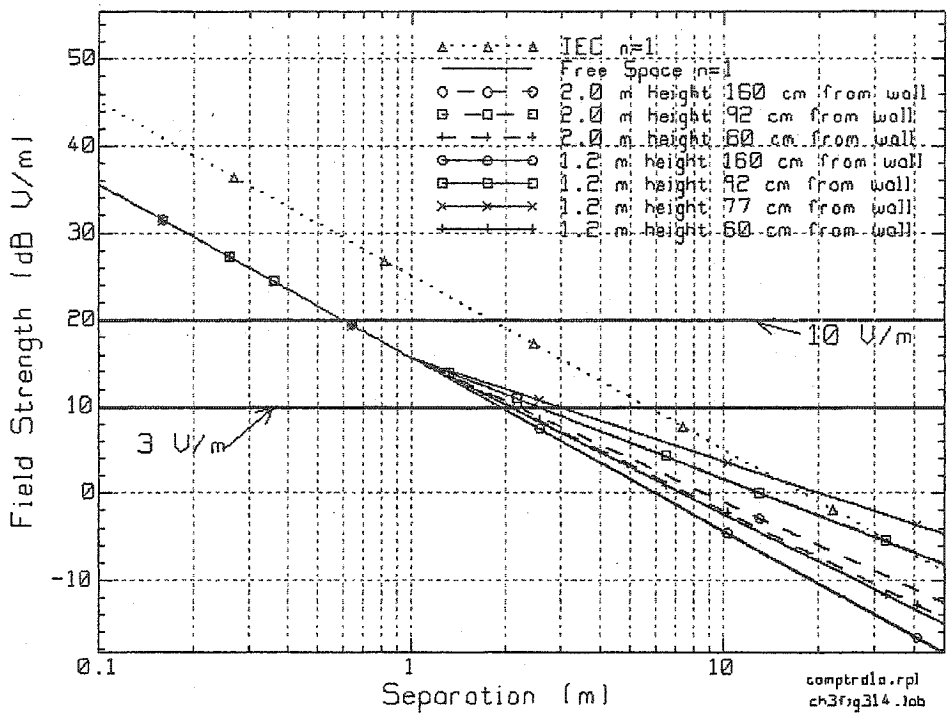

Figure 3.12 Trends for measured fields for trajectories at different heights and locations within the corridor.

Figure 3.12 shows the behavior of the field for 120 and 207 cm above the floor. Note that the "power law" trend line exceeds the IEC field strength estimate at large distances in some cases. This implies that the IEC minimal separation may be risk free for devices with very low immunity.

In the distribution of the residuals in figures 3.8 (a) and 3.8 (b), the range of ±1 volt per meter corresponds to around 85 % confidence levels, that is a 15% risk of exceeding immunity level, for these experiments.

Table 3.6

MSR distances using measured trends with 50% and 15% risk levels for 120 and 207 cm above floor. Using 3 V/m immunity level and the source radiating 0.6 watts

Height above floor (cm)	Distance from wall (cm)									
	60		77		92		130		160	
Risk of exceeding Imm.	50%	15%	50%	15%	50%	15%	50%	15%	50%	15%
120 (cm)	2.2 m	3.3 m	3.2 m	6.0 m	2.7 m	4.8 m	3.0 m	5.5 m	2.0 m	3 m
207 (cm)	2.1 m	3.4 m	-	-	2.7 m	4.8 m	-	-	2.3 m	3.9 m

Table 3.7

MSR distances using measured trends with 50% and 15% risk levels for 120 and 207 cm above the floor. Using 10 V/m immunity level and the source radiating 0.6 watts

Height above floor (cm)	Distance from wall (cm)									
	60		77		92		130		160	
Risk	50%	15%	50%	15%	50%	15%	50%	15%	50%	15%
120 (cm)	0.6 m	0.67 m	0.6 m	0.67 m	0.6 m	0.67 m	0.6 m	0.67 m	0.6 m	0.67 m
207 (cm)	0.6 m	0.67 m	-	-	0.6 m	0.67 m	-	-	0.6 m	0.67 m

From table 3.6, the minimal separation distances for the 3 V/m immunity level are dependent upon the location within the corridor volume. The largest separations are required for paths close to the centerline of the corridor while paths closer to the side walls had smaller MSR distances. This is due to the path loss exponent being smallest near the corridor centerline. The MSR distance is also largest near the corridor centerline and smallest near the sides of the corridor. The table shows that the risk of exceeding the immunity level of 3 V/m can be reduced from 50% to at the most 15% by increasing the separation distances by a factor of 2.

Table 3.7 contains the MSR distances at 50% and 15% risk for a device in the same environment but with a 10 V/m immunity level. In this case distances are all within 1 meter of the source and so the path loss exponent used is the same as free space. The 50% risk recommended distance is 60 cm. The MSR distance at 15% risk is 67 cm rather than 60 cm separation. Increasing the separation from 60 to 67 cm can reduce the risk of exceeding the 10 V/m immunity level drops from 50% to 15%.

The measurements were complemented by a series of simulations that duplicate, validate and enhance the information in the measured data set.

3.6 Corridor Trajectory Simulations

Geometrical Optics is used in this thesis to simulate indoor propagation, as described in section 2.4. A detailed model of the ninth floor was made for input by the GO_3D program. Figure 2.1 is in fact created by GO_3D to show the input geometry. The 7^{th}, 8^{th} and 9^{th} floor corridors are nearly identical so the model should predict fields in these floors well. Each floor has an elevator alcove near glass-block wall "B". However, note that the 9^{th} floor corridor is lined with metal lockers along one side which are not included in the GO model; thus the model is more representative of the 7^{th} and 8^{th} floor corridors which have no lockers.

The electrical properties of the wall materials given in chapter 1 were obtained from the literature for the "analog" cell phone frequency of 850 MHz. The same values were used at 1900 and 2400 MHz. The electrical properties of the wall materials may be substantially different at these frequencies but better values were not available.

Simulations of the electric field were performed for 850 MHz, 1900 MHz and 2400-MHz dipole sources. The results for the centerline trajectories are plotted in figure 3.13. The simulations use a point spacing of 3.2 cm corresponding to the "high-resolution" measurements.

The simulated fields are very close in strength and structure near the source. Further than 1-meter from the source, the interference patterns of the fields exhibit different degrees of structure and attenuate at different rates. The 850-MHz simulation has the lowest level of structure in the interference pattern and the highest rate of field strength attenuation with separation from the source. The complexity of the interference pattern at 1900 MHz was greater than at 850 MHz and less than the 2400 MHz simulations. The rate of field strength attenuation was less for the 1900 MHz simulation than for the 850-MHz simulation. The 2400 MHz simulation had the lowest rate of field strength attenuation and the most structured interference patterns of the centerline trajectory simulations. The path loss exponent values are given in figure 3.14.

The trends of the data in figure 3.13 are plotted in figure 3.14. At 850 MHz the path loss exponent is largest at $n = 0.77$, it is 0.66 at 1900 MHz and 0.59 at 2400 MHz. While the path loss exponents differ, the field strength values provided by the trends within the corridor are within 4 dB of each other for distances further than 1-meter from the source. The differences in the path loss does not indicate large differences in the estimates of field strength.

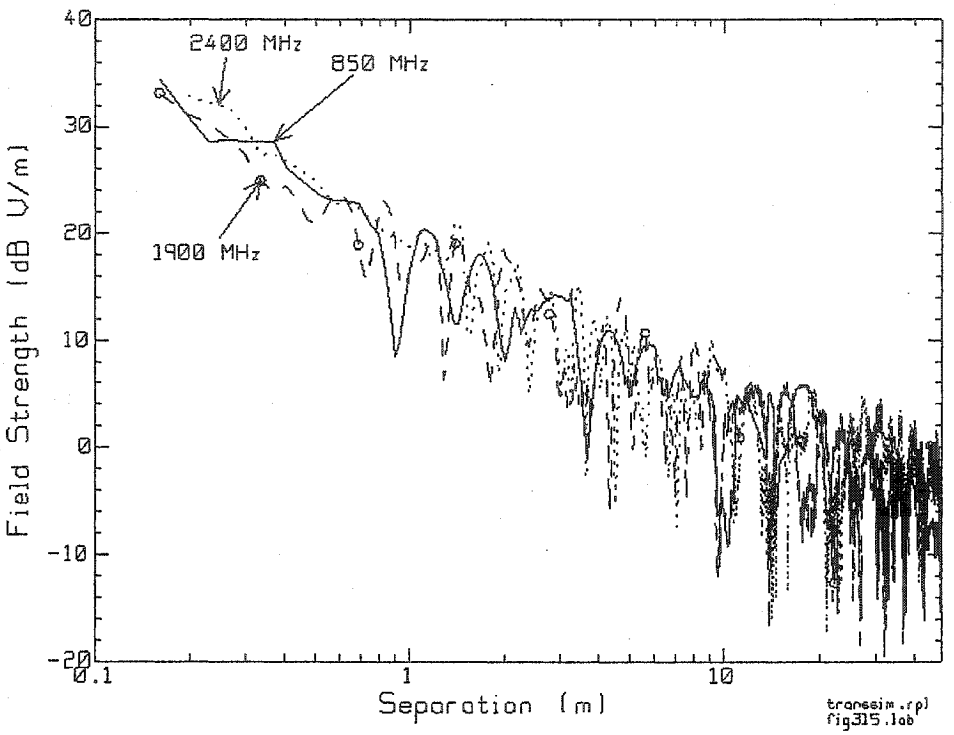

Figure 3.13 Centerline trajectory fields for 850 (solid), 1900 (dashed circle) and 2400 MHz (dotted) simulations 0.6-watt dipole source

The residuals of the data from the trends are plotted in figure 3.15. The distributions are very close for the entire range of values. At 2400 MHz there is a higher proportion of lower residual values, from –1.5 to -0.5 V/m, than the other two distributions. This is due to the more structured interference pattern of the 2400 MHz field that causes more variability in the residual. The greater structure is due to the shorter wavelength

The validation of the simulated centerline trajectory data was accomplished by comparing the trend and residual information for 850 MHz and 1900 MHz data sets for the corridor.

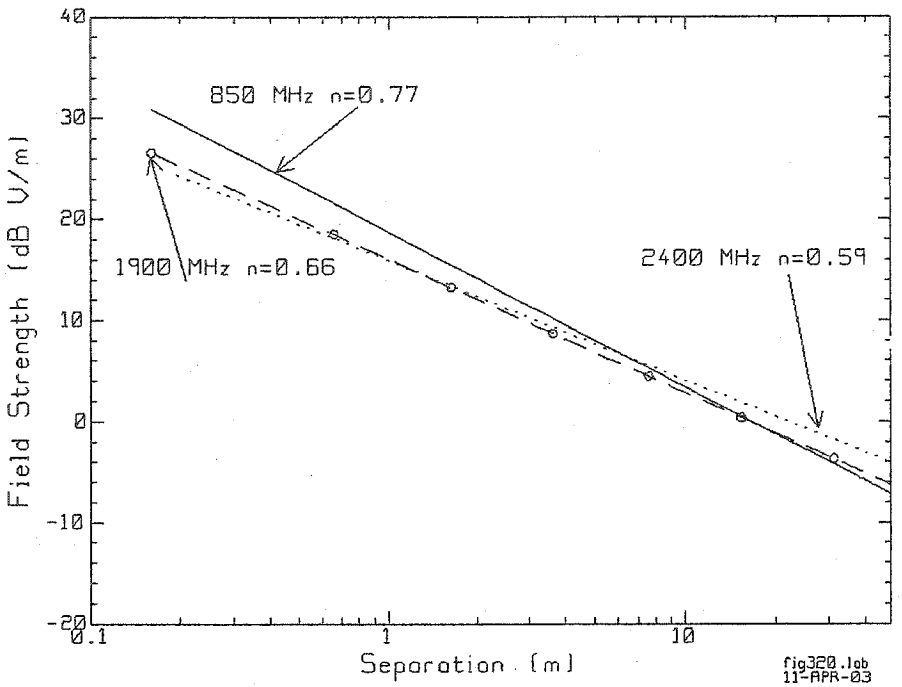

Figure 3.14 Mid-corridor trends for 850 (solid line), 1900 (dashed line circle) and 2400 MHz (dotted line) simulations 0.6-watt dipole source

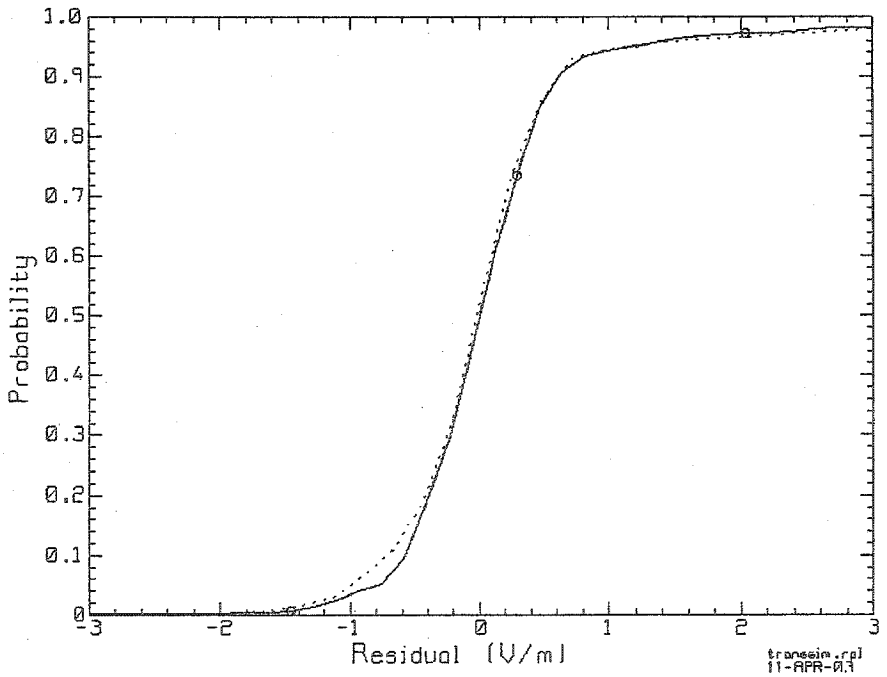

Figure 3.15 Mid-corridor distribution of residuals for 850 (solid line), 1900 (dashed line circle) and 2400 MHz (dotted line) simulations 0.6-watt dipole source

3.7 Validation of Single Trajectory Simulations at 850 and 1900 MHz

Figure 3.16 displays the trends for the measured and simulated data at 850 and 1900 MHz. Table 3.8 gives the path loss exponents values. At 850 MHz, the measured path loss exponent is 0.63, close to the simulated path loss exponent of 0.73. At 1900 MHz ,the measured path loss exponent was 0.70, very close to the simulated path loss exponent of 0.66. Note that the measured path loss exponent values in table 3.8 were derived from measurements in the ninth floor corridor that had lockers along the corridor. These lockers went about 25 cm deep into the corridor making the corridor narrower for the portion of the corridor that had lockers. Since the lockers were not included in the simulation, this could account for some of the differences between the measured and simulated path loss exponents. The trends begin at around 20 dB V/m and drop off to around --8dB V/m near the end of the corridor. The trends were within 7 dB V/m of each other for the majority of the corridor length. While the slopes were different, the trends were very close for the length of the corridor.

Table 3.8

Path loss exponents for 850 MHz and 1900 MHz measured and simulated fields along corridor centerline using 3.2 cm spacing between data.

Frequency (MHz)	Type	n
850	Measured	0.63
850	Simulated	0.77
1900	Measured	0.70
1900	Simulated	0.66

When the trends are plotted, figure 3.16, the differences between the trends are relatively small for the length of the corridor. The differences in the path loss exponents do not lead to large differences in field strength estimates.

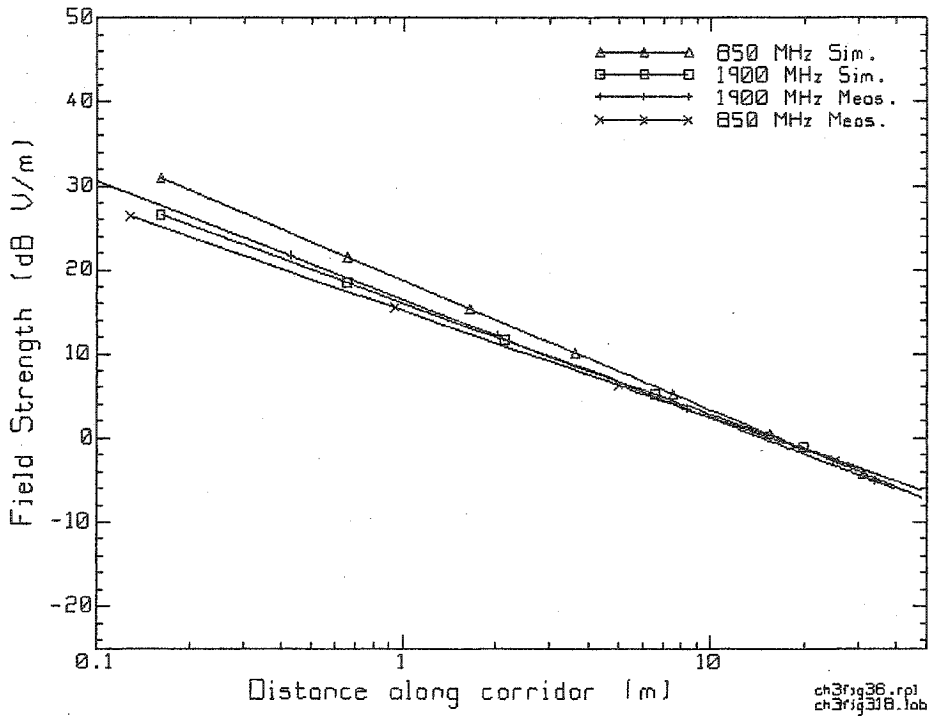

Figure 3.16 Comparison of trends for measured and simulated centerline trajectories at 850 MHz and at 1900 MHz.

The distributions of the residuals for measurements and simulations were obtained and are plotted in figure 3.17. The curves for the simulations at 850 and 1900 MHz are almost identical. With the exception of the 1900 MHz measured data residual, over 95% of the residuals are less than 3 V/m. The simulated residuals are closely grouped around the 0 V/m level with 95% of the residuals within ±1V/m. The measured data exhibits greater variability, with only 76% of the 850 MHz and 65% of the 1900 MHz residuals within ±1V/m. The lower variability allows for more precise MSR estimates within the corridor.

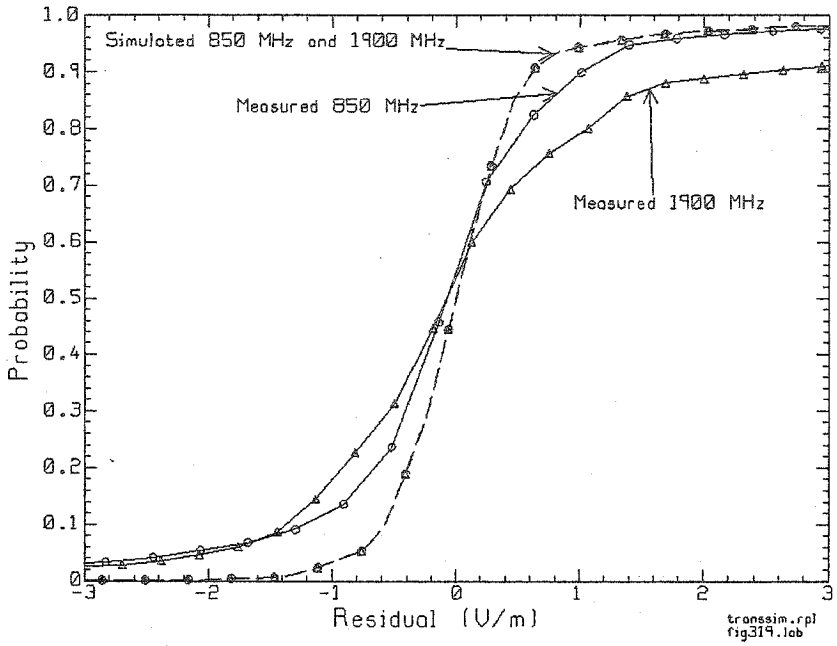

Figure 3.17 Distributions of residuals of measured and simulated 850 and 1900 MHz centerline field strengths

Generally, even though there were different components used in measurements (E_Z) and simulations (E_X, E_Y, E_Z) very good agreement resulted, probably due to dominance of EZ. Any differences (e.g. close by at different heights) are acceptable to estimate worst-case risk.

3.8 EMC Analysis for Centerline Trajectory Simulations

The MS and MSR distances were computed for the simulated data at 850, 1900 and 2400 MHz shown in figure 3.13. The path loss within 1 meter of the source was modeled using free space (n=1) while distances further than 1 meter from the source were modeled using the path loss exponent obtained from the trend. This was done to better model the actual behavior of the field strength in the corridor both close and

further from the source. The IEC and free space trends are plotted along with the curves used for MS and MSR computation in figure 3.18.

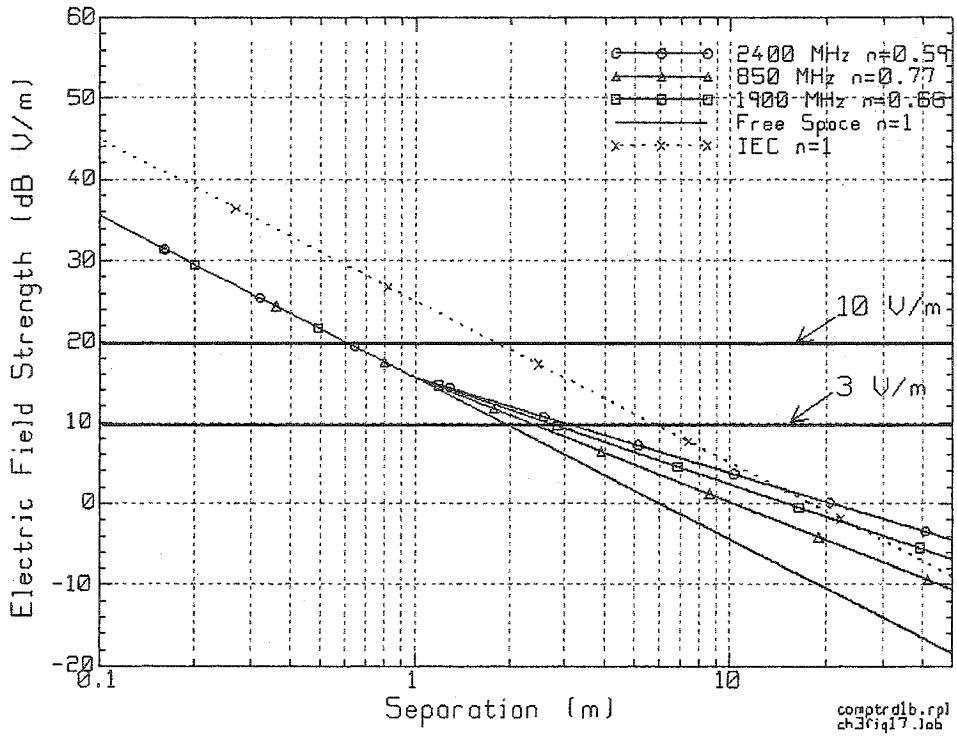

Figure 3.18 Minimal separation distances for trends at 850, 1900 and 2400 MHz centerline power law models

The IEC curve estimates the field strength for a 600 mW source from the IEC estimate of equation 1-2. Using the IEC model, a device with immunity 3 V/m needs to be separated from a 600 mW wireless source by 5.9 meters. The risk of an EMI incident when using the minimal separations based on the IEC model is intended to be zero. The IEC curve provided the highest field strength estimates for most of the corridor length. The 2400 MHz trend estimated field strengths of nearly the same level as the IEC trend for the last 7 meters of the corridor. The solid curve with no symbols in figure 3.18 shows the decline in field strength with distance in free space. The solid curves with symbols are the "bi-linear" trend lines at 850, 1900 and 2400

MHz. The term "bi-linear" is used to indicate that the line has two straight-line segments. The first segment is for distances within one meter of the source. This segment has a path loss exponent of n=1 (free space) and the reference electric field strength E_o is obtained assuming free space propagation. The second segment is used for distances greater than one meter from the source, the same reference field strength is used and n is obtained using equation 2-5 and the simulated field data.

The MS distance is computed using the bi-linear trend line in the following manner. The immunity level of the device is determined and plotted on the graph. In order to illustrate the process, immunity levels of 3 V/m (9.54 dB V/m) and 10 V/m (20 dB V/m) are used. The horizontal distance where the intersection of the immunity level and appropriate bi-linear curve is read from the axis. This distance is the MS distance. For example, at 850 MHz the bi-linear curve intersects the 3 V/m immunity level at 2.2 m. The MS distance for 850 MHz for a device with 3 V/m-immunity is 2.2 m. The risk of an EMI incident with the 2.2 m separation is 50%.

To find a minimal separation distance at a risk level of an EMI incident of 5%, the following steps are used. The distribution of the residuals, figure 3.16, is used to determine the risk field strength associated with the risk of EMI incident. A risk of EMI incident of 5% corresponds to the 95% level on the distribution. The 850 MHz simulated residuals has 95% of the data below 1 V/m. The risk field strength is 1 V/m. The modified immunity level of the device is obtained by subtracting the risk level from the immunity level of the device. In this case the 3 V/m immunity level is reduced by 1 V/m (risk field strength) to obtain a modified immunity level of 2 V/m or 6.02 dB V/m. The intersection of the bi-linear curve for the 850 MHz and the 6.02 dB V/m level occurs at 3.5 m. The MSR with 5% risk occurs at 3.5 m from the source.

Table 3.9 gives the MS distances at 850 and 1900 MHz. If the free space curve is used to estimate the MS distances (1.8 m), the risk of an EMI event is 70-85%. Conversely if the IEC model is used, the risk of an EMI event is virtually zero. The IEC distances are too large to be practical for the use of wireless sources within a hospital environment. The purpose of the MSR distance is to provide a measure of the quality of the protection that the EMC policy offers. Thus if a 5% risk is deemed acceptable, then the much smaller MSR separations in table 3.9 could be used, which would be more practical for the implementation of wireless technology in a hospital.

Table 3.9

MSR distances for 850 and 1900 measured and simulated data and minimal separations based on free space and IEC trends for 0.6-watt source and 3 V/m immunity. * = 10% risk of exceeding immunity.

Trend	850 MHz		1900 MHz		Free Space	IEC
Risk of exceeding immunity	50%	5%	50%	5%	-	-
Measured	3.0 m	5.7 m	2.7 m	4.6 m *	1.8 m	5.9 m
Simulated	2.5 m	4.1 m	2.4m	4.0 m	1.8 m	5.9 m

When determining the MS distances for a device with a 3 V/m or 10 V/m immunity level, the same procedure was followed as in section 3.2. The MS distances for the simulated fields are found in table 3.9 where the simulated and measured MS and MSR distances were compared. The MSR distances for the 850 and 1900 MHz simulated fields were based on 5% risk of exceeding immunity as was the 850 MHz measured data. The 1900 MHz data used a 10% risk of exceeding immunity level; see section 3.2 for more detail.

3.9 Multiple Trajectory Simulations

The simulations were next extended to trajectories that passed through the corridor volume along paths displaced from the centerline horizontally and vertically. The trajectories chosen were analogous to the ones used in measurements in section 3.3 for multiple trajectories.

Electric fields were simulated along paths 30, 120 and 207 cm height and 60, 77, 92, 154 and 160 cm from the side wall of the corridor at 1900 MHz. The resulting data is plotted in figure 3.19 (a)-(c). Figure 3.19 (a) shows trajectories at 207 cm above the floor, figure 3.19 (b) shows trajectories at 120 cm above the floor and figure 3.19 (c) shows trajectories taken at 30 cm above the floor. In all cases, the simulated fields out to 2 meters from the source varied from around 10 to 30 dB V/m. The fields decreased in strength but demonstrated higher variability as the distance from the source increased. At the far end of the corridor the fields were lower, varying from 0 to less than –20 dB V/m. The increased structure at the further end of the corridor had two components, a small-scale variation that produced variation over small position changes (centimeters) and a larger scale variation that produced changes over larger distances (meters).

Unlike the measured fields taken at 30 cm heights, figure 3.5 (c), the simulated fields at 30 cm height show a gradual decrease in field strength with distance from the source. This difference in behavior indicates a propagation mechanism other than GO is needed to model the fields near the floor of the corridor. The closer spacing between data results in more structure in the simulated fields, seen in figure 3.19 (a)-(c).

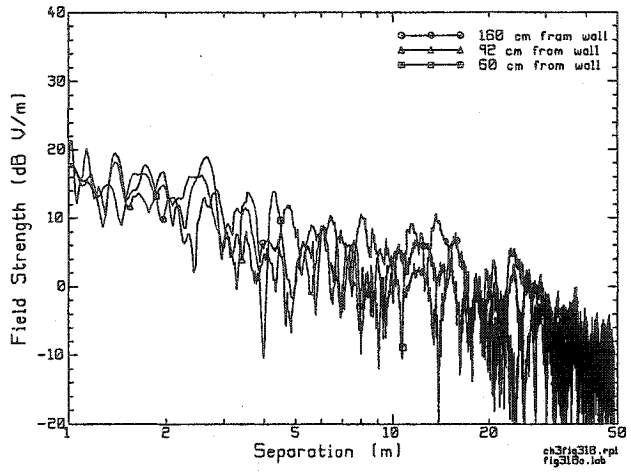

(a) 207 cm above floor

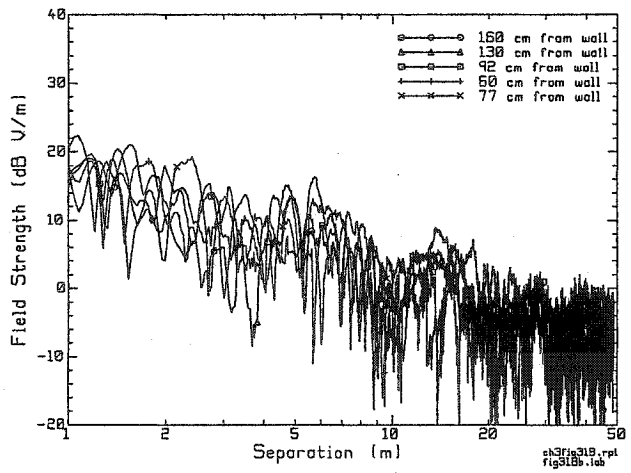

(b) 120 cm above floor

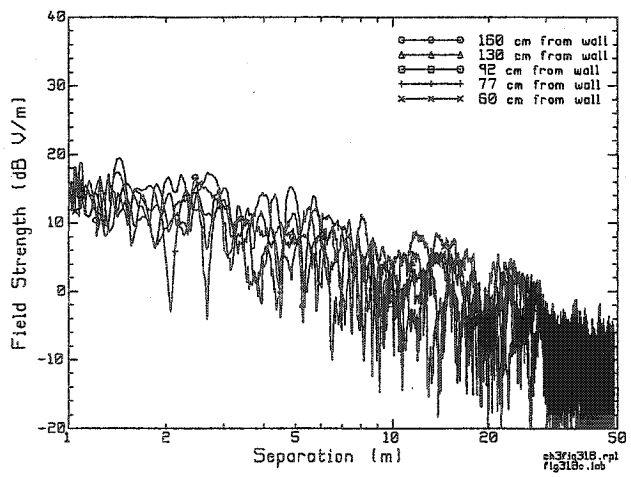

(c) 30 cm above floor

Figure 3.19 (a)-(c) Simulated field strengths at 1900 MHz corridor model using 600 mW dipole source located 1.2 m from wall "A".

The extraction of the information found in the simulation data followed the same process as in the measurement section. The trends were obtained as described in section 2.5. The resulting trend lines for the trajectories at 207, 120 and 30 cm height are plotted in figures 3.20 (a), (b) and (c) respectively. The trends all begin between 15 and 20 dB V/m and decrease until –5 to –10 dB V/m is reached at the end of the corridor, about 50 meters from the source. The field strength of the trends tended to be close, usually with 4 dB for the length of the corridor. The field strength at all three heights decreases slower near the middle of the corridor and faster near the sides of the corridor.

The cumulative distributions of the residuals are plotted in figure 3.21 (a)-(c). For all of the distributions shown, 99% of the data was found within 5 V/m of the median value of 0 V/m. When the range was narrowed to within 1 V/m of the median value, the percentage of residual data that was found within the range changed to approximately 84 % of the data points. This is larger than the 60-75 % of data points that were within this range for the measured data for the trajectory along the middle of the corridor at 1900 MHz. In the case of the residuals from the simulated data taken at 30 cm above the floor, figure 3.21 (c), the range from –5 V/m to 5 V/m contains around 99% of the data. When the range was restricted to –1 V/m to 1 V/m the amount of data that fell within the range decreased to 90 %. While these values are close to the other simulated ranges, they are very different from the range of the equivalent measurement that had 40% of the data falling within 1 V/m of the median. Overall, the distributions of the residuals of the simulated data tended to have lower variation than the measured data. This was partially due to the wider spacing between measurement points, 32 cm, compared to simulated data, 3.2 cm.

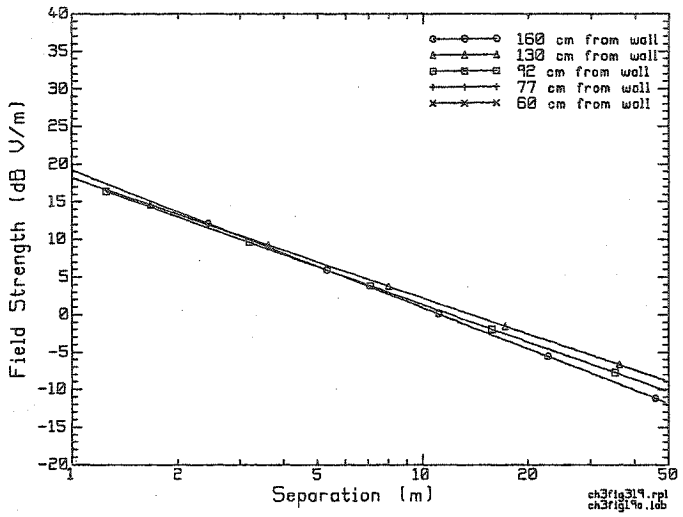

(a) 207 cm above floor

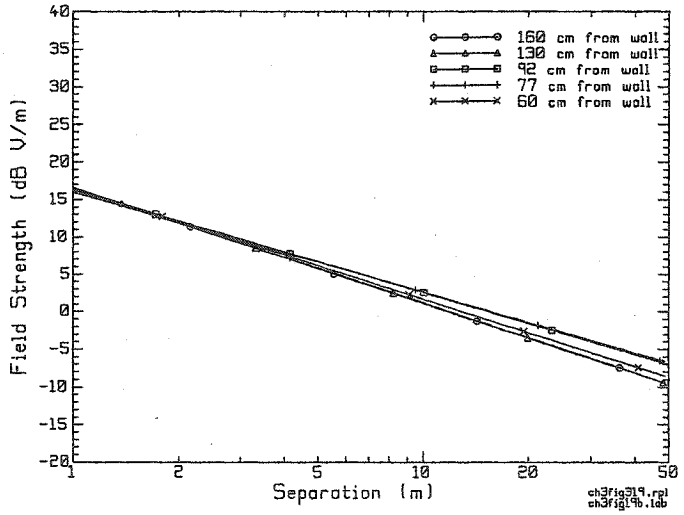

(b) 120 cm above floor

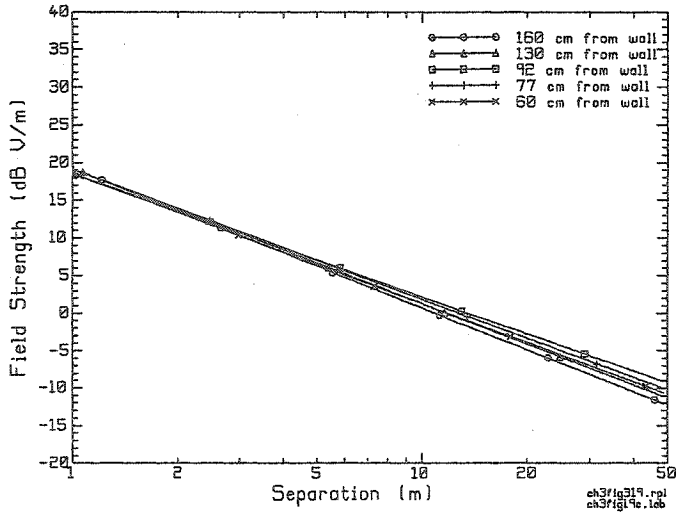

(c) 30 cm above floor

Figure 3.20 Trends of simulated data along corridor centerline at 1900 MHz

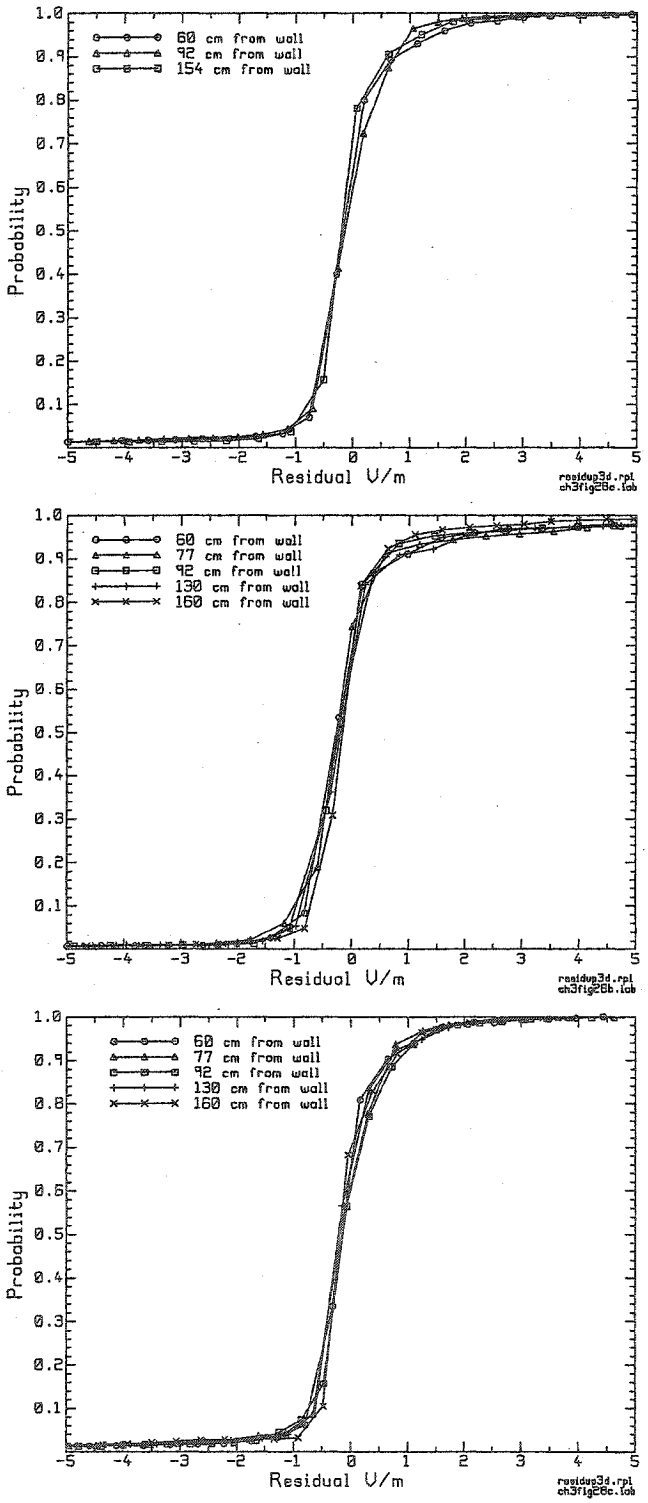

Figure 3.21 Residuals of data and trends for corridor simulations at 1900 MHz

The distributions of the residuals taken at different heights but at the same cross-sectional position are plotted in figure 3.22. While in all three cases the range –5 V/m to 5 V/m contains 99% of the residual data, the more restricted range of within 1 V/m of the median has around 85 % of the residual data points for the 30 and 120 cm height trajectories, while the 207 cm trajectory residual has around 90 % of the data points within 1 V/m of the median.

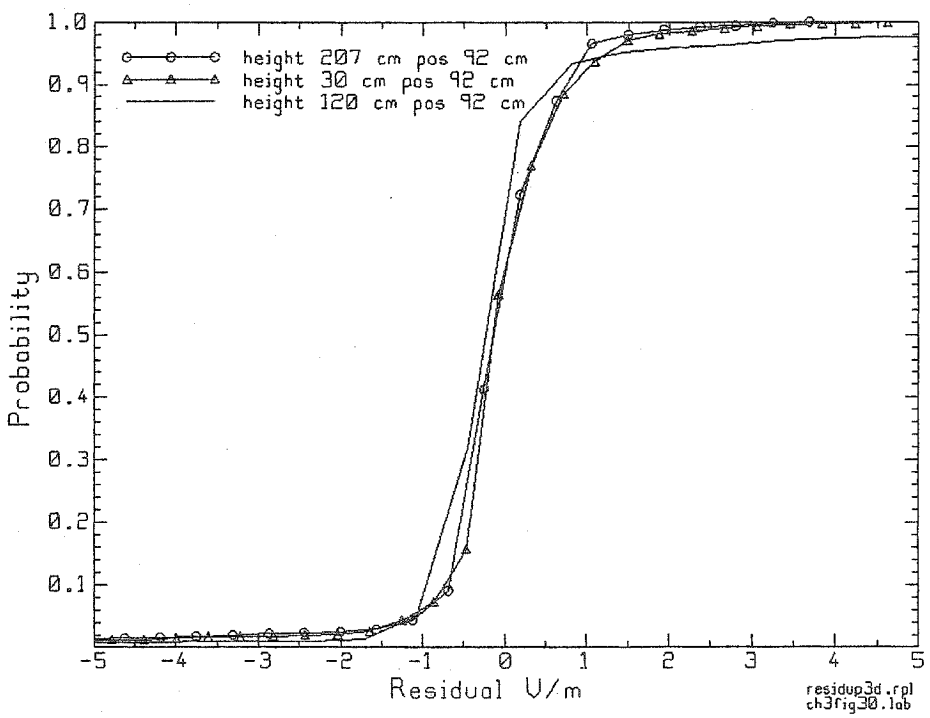

Figure 3.22 Cumulative distributions of residuals at 1900 MHz along centerline of corridor.

Unlike the more coarsely sampled measured data, the distributions of the residuals were similar for trajectories taken at different heights. The general shape of the distributions was similar for the different trajectories within the volume of the corridor. The range of the field values was also consistent for all of the distributions of residuals for the simulated multiple trajectories.

3.9.1 Comparison of Measured and Simulated Multiple Trajectories

It is important to note that the sampling of the 3-D measurements was 32 cm between measurement points, while the simulated fields used 3.2 cm spacing between measurement points. There were 10 times the number of samples in the simulation than in the measured 3-D data sets. The wavelength was around 15.79 cm at this frequency. The measured fields were being sampled at much less than the Nyquist sampling frequency.

The trajectories obtained from measurements and simulations will be compared in the following manner. The slopes of the trends, namely the path loss exponents, will be plotted as a function of the position within the corridor volume. The distributions of the residuals of the trends will be plotted in order to compare the variability of the data for each trajectory.

Figure 3.23 shows the path loss exponents as a function of the distance from the left wall and height above the floor. The path loss exponents for the simulated trends fall within the range of 0.64 to 0.89 for all heights and cross-sectional positions. There is a tendency for the path loss exponents to be smallest near the middle of the corridor, 92 cm from left wall. By contrast, the measured data has more variable values for the path loss exponents. The values vary from 0.59 to 1 for heights 120 and 207 cm above the floor and from 0.01 to 0.2 for trajectories 30 cm above the floor. The path loss exponents are markedly lower for trajectories near the middle of the corridor for all heights and the smallest trends occur close to the floor.

The largest difference in path loss exponents for the simulated and measured trajectories at 120 and 207 cm above the floor was around 26 %. This was smaller

than the difference between the path loss exponents for the simulated and the measured trajectories at 30 cm above the where the largest difference was around 195 %.

The distributions of the residuals of the trajectories discussed above are compared in figure 3.24. The residuals of the simulated fields had sharp slopes around the 0V/m point. The simulated data had around 95 % of the data within 1 V/m of the median value. The residuals of the measured data have relatively shallow slopes, in particular the trajectories at 30 cm above the floor. The measured data had around 80% of the data within 1 V/m of the median for the trajectory at 207 cm above the floor, around 50% of the data for the trajectory 120 cm above the floor, and around 20% of the data within 1 V/m of the median for the trajectory 30 cm above the floor.

When comparing the measured and simulated corridor volume scans, the path loss exponent of the power law model again provides an important parameter for comparison.

The path loss exponent obtained from the simulations was within the range of values obtained from measurements with the exception of the measurements near the floor. The path loss exponents of the simulated data did not exhibit the dependence on location within the corridor that the measurement data did. The attenuation of simulated fields was slightly lower near the middle of the corridor than at the side walls. The simulation path loss exponents, unlike the corresponding measurements, did not exhibit strong variation within the corridor cross-section. The low, nearly constant field strength found at 30 cm above the floor in the measurement data was not present in the simulation data. This suggests that the propagation mechanism that causes the field behavior at 30 cm above the floor differs from GO mechanisms used.

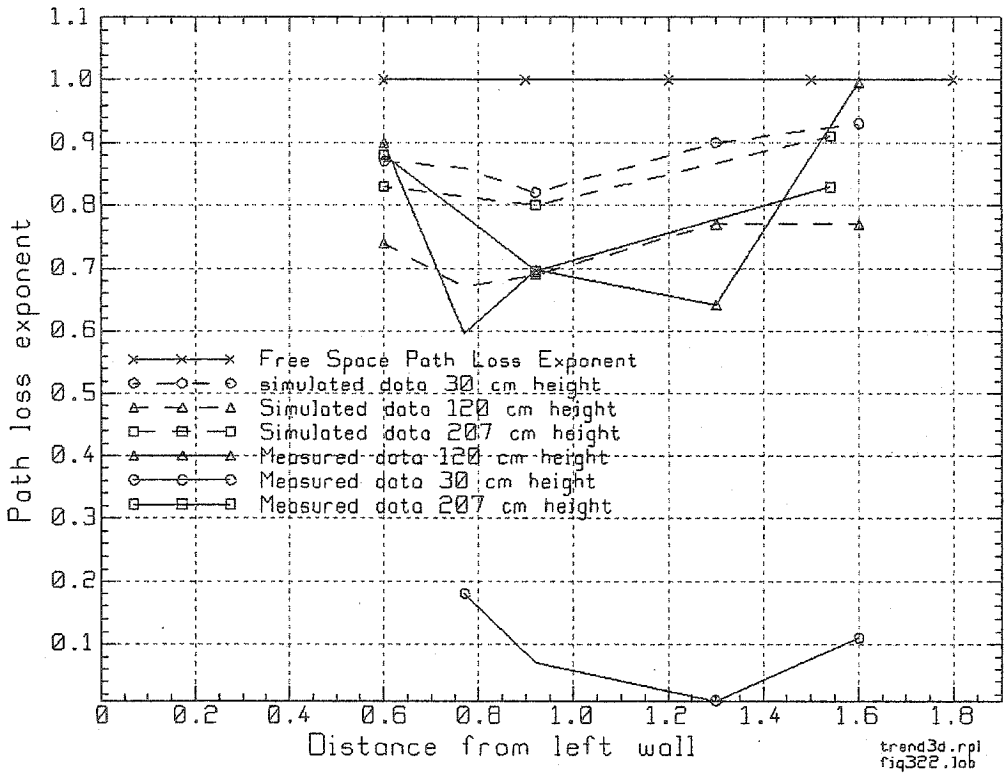

Figure 3.23 Comparison of measured and simulated path loss exponents at 1900 MHz ninth floor corridor. Free space path loss included for comparison.

Unlike the single trajectory comparisons, the distributions of the residuals of the multiple trajectories were very different. Note that the sampling differed for the measurement and simulations that may account for some of the differences in the distributions.

Using the characterizations developed in the previous chapters, the potential for EMI using various policies will be investigated in the next section.

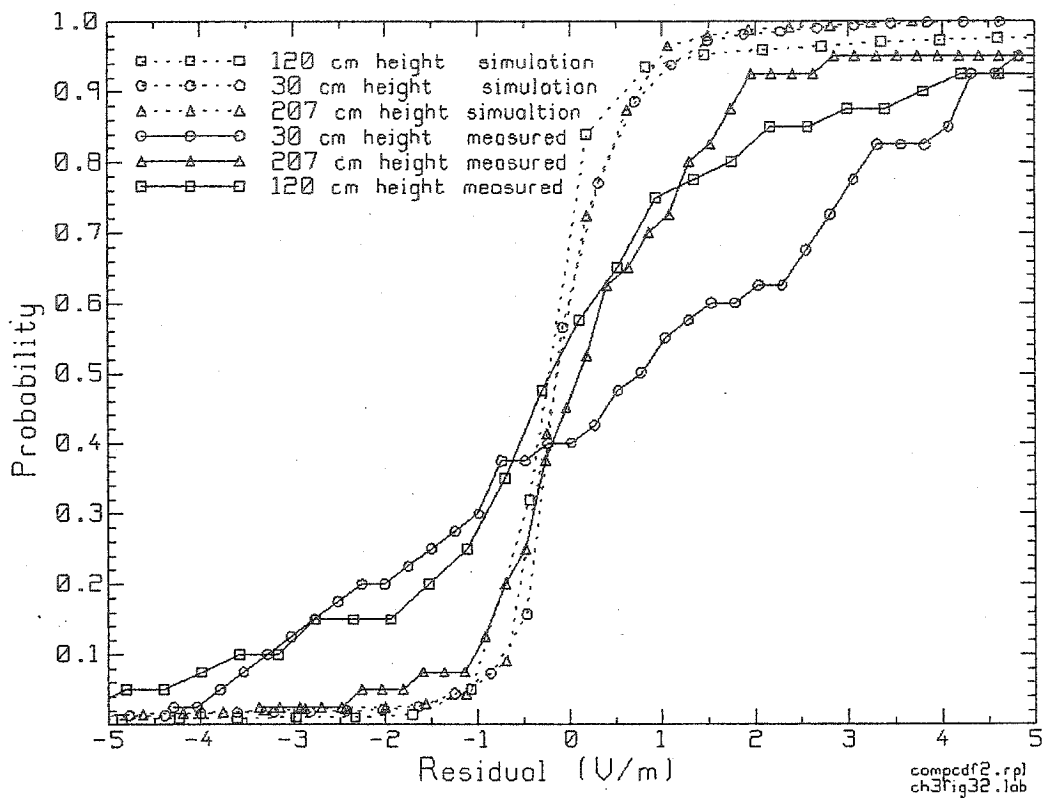

Figure 3.24 Distribution of residuals for measured and simulated fields along corridor centerline ay 1900 MHz.

3.9.2 EMI Results for Multiple Trajectories

The trends of the simulated fields for trajectories that pass through the corridor through upper parts of the volume, 120 and 207 cm above the floor, were compared with the field estimates for free space and the IEC standard.

In contrast with the behavior shown in the 3-D measurement section above, the simulated field trends for the trajectories at 30 cm above the floor had slopes similar to the trends at 120 and 207 cm above the floor. The simulated fields for trajectories 30 cm above the floor did not duplicate the low strength, nearly constant fields that were recorded during the measurements. The trends of the simulated fields for all

three heights above the floor ranged from 0.8 to 0.9. The slopes of the trends did not substantially vary along the corridor cross-section.

A selection of the trends is plotted in figure 3.25; these trends were used to illustrate the variation of the slopes of the simulated trends. The shallowest slope was obtained from the data near the middle of the corridor, at 30 cm above the floor. The intermediate slope value was taken near the left wall at 120 cm above the floor and the sharpest slope was obtained from data taken closest to the right hand wall at 207 cm above the floor.

The minimal separations were computed using the trends and both 50% and 5% risk levels, 5% risk corresponding to ±1 V/m range in field strength for the simulated fields. The results of the minimal separations calculations were placed in table 3.10.

The minimal separations were all less than the IEC recommended distance of 5.9 meters for a 3 V/m immunity level. The minimal separations for the 10 V/m immunity level were the same as in table 3.7.

The simulated data had generally smaller minimal separations and higher confidence levels. The smaller separations typically occurred near the sides of the corridor while the larger separations typically occurred near the middle of the corridor.

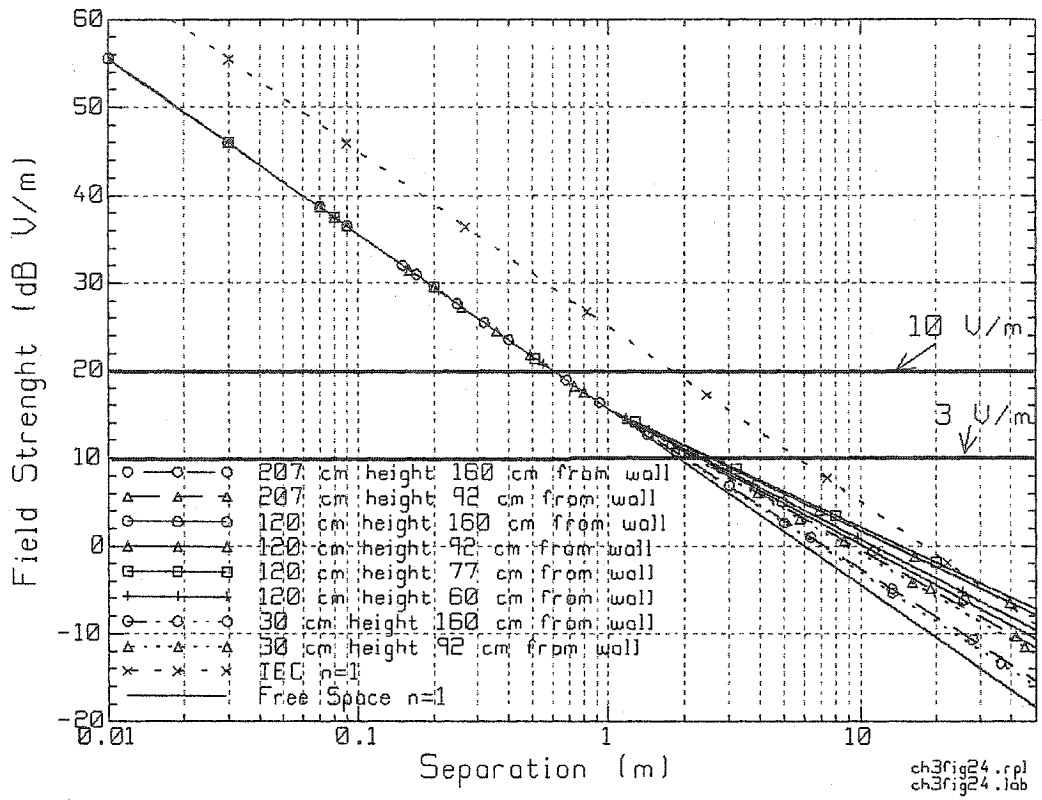

Figure 3.25: Bi-Linear curves used to determine MS and MSR distances for devices with various immunities.

Table 3.10

MSR distances using measured trends with 50% and 5% risk level for 120 and 207 cm above the floor. Using 3 V/m immunity level and the source radiating 0.6 watts

Height above floor (cm)	Distance from wall (cm)									
	60		77		92		130		160	
Risk of exceeding imm.	50%	5%	50%	5%	50%	5%	50%	5%	50%	5%
30 (cm)	2.2 m	3.5 m	2.2 m	3.6 m	2.4 m	3.8 m	2.2 m	3.4 m	2.1 m	3.2 m
120 (cm)	2.6 m	4.4 m	2.8 m	5.1 m	2.7 m	4.9 m	2.5 m	4.1 m	2.5 m	4.1 m
207 (cm)	2.3 m	3.7 m	-	-	2.4 m	3.9 m	-	-	2.1 m	3.3 m

3.10 Summary

Electric fields generated by a single RF transmitter placed at one end of a hospital corridor were measured using single trajectories along the middle of the corridor and multiple trajectories that passed through the volume of the corridor. These measurements were performed at 850 and 1900 MHz.

The information provided by the trajectory measurements was used to generate models for field strength as a function of distance away from the transmitter, trends, and for the variability of the field strength around the trend, distributions of residuals.

The trends indicated that the rate that the measured fields attenuated varied with position within the volume of the corridor. Fields near the walls tended to attenuate more rapidly than fields near the middle of the corridor. Fields near the floor of the corridor were weaker than fields near the middle of the corridor and did not attenuate very much with distance.

Numerical simulation of electric fields within the corridor were performed using a GO based code. The simulations agreed with the measured fields very well in most cases except for fields near the floor. The simulations were not able to reproduce the low, nearly constant, fields that were encountering during the 1900 MHz measurements.

The trends and distributions of the residuals of the measured fields were used to quantify EMI risk for different EMC policies. Relative to models based on the measured data: A) If the source was assumed to radiate maximum power, minimal separations based on free space were the least effective in reducing EMI risk and the

IEC standard was the most effective. B) If realistic power levels for the source were used, free space minimal separations were much more effective in reducing EMI risk and the IEC standard was very conservative in reducing EMI risk.

The next chapter in the thesis will explore the behavior of the fields on a planar surface within the corridor volume. These are preliminary 3-D studies where the planes provide discrete volume images of the electric fields at given heights.

Chapter 4

Corridor Planar Surface Simulations, Morphology and Statistics

This chapter presents the field strength in a 50-m corridor of figure 2.1 obtained by computation using Geometrical Optics. The field is calculated on a planar surface parallel to the floor that is at the same height as the measured data in chapter 3.

The results of the simulations are classified according to frequency of the source and location of the source relative to the end wall. The data obtained is compared with electromagnetic compatibility standards. The planar plots of the fields were presented using color contour maps as described in chapter 2.

The contour maps emphasized the structural characteristics, or morphology, of the fields. This field data is used to obtain the cumulative probability distribution of the field strengths within the region under study. The distributions of the fields were computed and presented as cumulative distributions.

The effectiveness of various EMI policies is investigated using the morphology and statistics of the simulated fields for the corridor. These investigations are presented at the end of the chapter.

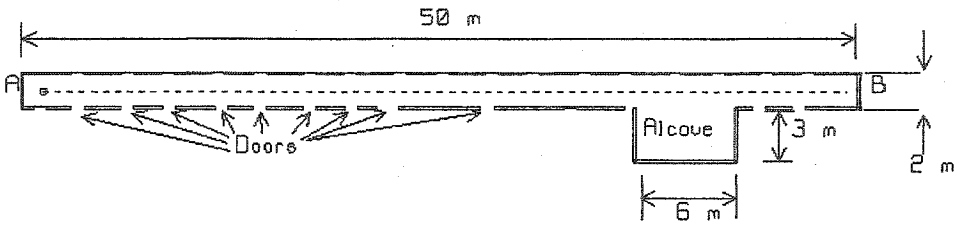

Figure 4.1 Schematic of corridor used in simulations, A and B indicate location of glass-block walls. Doorways were closed in simulations.

4.1 Planar Surface Scans

A three-dimensional model of the corridor with ceiling height of 2.5 meters above the floor was used for these simulations. A schematic of the simulation model is shown in figure 4.1. Only the corridor walls were included in the simulation and not the room walls. Thus any ray that passes out of the corridor and through a wall or door exits the model; that is, if the ray is not reflected back into the corridor from an adjacent room wall it is not considered in the simulation. The transmitter was placed near to the glass block wall labeled "A" in figure 2.1. Three-dimensional values for the distance between the transmitter and the glass block wall were set depending on the simulation. The transmitter power was fixed at 600 mW for the simulations performed in this study. The frequencies used were 850, 1900 and 2400 MHz. The corridor walls were modeled as clay-block and the floor and ceilings were modeled as reinforced concrete. The doors, constructed of either wood or metal, were in the "closed" position for the simulation. For the threshold chosen in these simulations, most rays that passed through the walls lost much of their strength and were discarded from field computations.

4.1.1 Planar Surface Simulations 850 MHz

In the simulations, the electric field was computed on a grid of 3.2 cm by 3.2 cm squares at different heights above the floor within the corridor. The field at the center of the square was used to approximate the field for the entire square. The planar surface was composed of a grid of these 3.2 by 3.2 cm squares. The source was a vertical dipole antenna. The magnitude of electric field strength for all three polarizations E_x, E_y and E_z was computed using ray-tracing method computation. The "total electric field strength" E_t, defined as the largest possible value of the field is all three-vector components were in phase.

$$E_t = \sqrt{|E_x|^2 + |E_y|^2 + |E_z|^2} \qquad \ldots (4\text{-}1)$$

The total electric field was used as the worst-case situation if all three components were in phase.

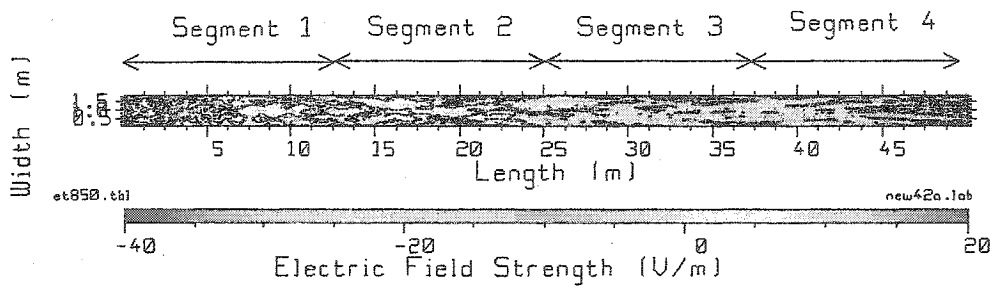

Figure 4.2 Contour map of fields, full view, divisions for stacked segment display noted on top of figure.

The planar surface color contour map provides information on the morphology or structure of the fields within the corridor. An example of a contour map for an 850 MHz simulation with the source near the left hand end wall of the corridor is shown in figure 4.2. The corridor is roughly 25 times longer than it is wide. For the corridor planar surface maps, the horizontal axis, distance in X, measures the distance along the corridor in meters, the left hand end wall being the zero location. The vertical axis, distance in Y, measures the position across the width of the corridor in meters, the bottom wall being the zero location. The field strength is plotted in dB referred to 1 V/m. The color scale went from –40 dB V/m to 20 dB V/m. The contours began at –40 dB V/m with 10 dB between successive contours.

The format of figure 4.2 presents difficulties in seeing particular features or regions because the contour map is so long compared to the width. In order to expand the scale while maintaining the aspect ratio of the plot, the contour map was divided into 4 equal segments each 12.5 meters long and 1.92 meters wide. Figure 4.2 shows the four 12.5 m segments that will serve as dividers. In figure 4.3, these four segments are plotted as a vertical stack with segment 1 at the top, segment 2 below segment 1, segment 3 below segment 2, and segment 4 at the bottom. This will be termed a "stacked-segment field map".

Figure 4.3 shows a stacked-segment field map for simulated fields for a planar surface at a height of 130 cm above the floor. The transmitter is a half-wave dipole operating at 850 MHz radiating 600 mW. The dipole is located at 1.2 m from the left end of the corridor and 0.9125 from the bottom wall. The field strength in the 12.5 meters closest to the left hand end wall is displayed in the top segment of figure 4.3. The section of the corridor between 12.5 m and 25 m from the left hand end wall of the corridor form the second segment, shown in figure 4.3 second from the top. The

section of the corridor between 25 m and 37.5 m from the left hand end wall form the 3rd segment from the top in figure 4.3, and the last quarter of the corridor is found in bottom segment of the figure. The distances along the corridor length were indicated along the bottom, horizontal axis of the plot. The vertical axis related the position along the across of the corridor. The black contours are related to electric field strength of –40, -30,…, 10, 20 dB V/m.

The color contour map of figure 4.3 is not symmetric about the centerline of the corridor. The source itself is not located on the centerline of the 1.92-m wide corridor; it is 0.9125 m from one wall, considerably off center. Also the placement of doorways along the length of the corridor is not symmetric from one side wall to the other. Although most of the doors are made of wood; two doors, marked "S" in figure 4.1 are steel doors hence highly reflecting. Also near the "B" end of the corridor there is a large alcove, (the elevator lobby), making the corridor asymmetrical in segment four of the contour maps.

The field strengths near the source are high, in the range of 20 to 50 dB V/m, and the contours exhibits strong symmetry with the sidewalls. Field strength above 20 dB V/m are off the top of the color scale and are graphed as white regions with contours at 30, 40 and 50 dB. At distances between 3 and about 16 m from the source the contours tend to be aligned diagonally. The fields tended to be stronger near the center of the corridor and weaker near the walls. Near the end of the corridor, the contours aligned in a manner suggestive of interference patterns from both the end wall and the sidewalls. The contours indicated stronger fields near the middle of the corridor and weaker fields near the walls.

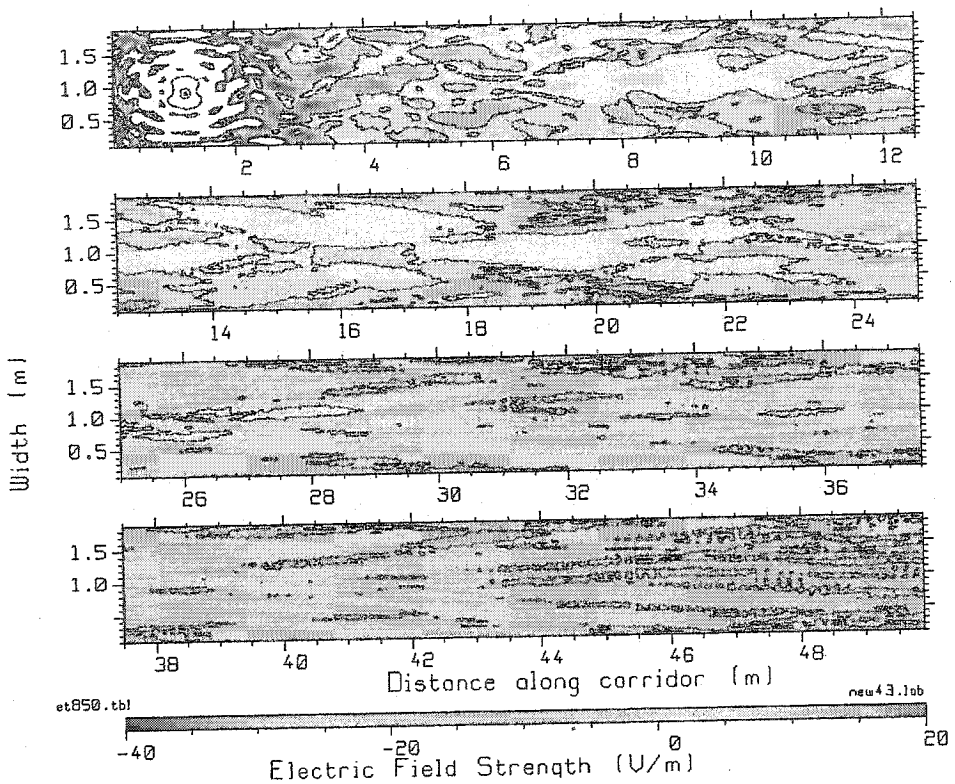

Figure 4.3 Planar surface plot of electric fields within corridor at 850 MHz Stacked segments: segment 1 at top, segment 4 at bottom

For distances further than 16 m from the end wall, the fields are strongest near the center and the contours that enclosed the higher fields are aligned along the length of the corridor and the larger field strengths are found in the middle of the corridor. The field strengths along the middle of the corridor were typically 5-10 dB stronger than the fields near the wall. The contour map used 10 dB contours starting at –40 dB V/m.

While the stacked-segment planar surface contour map provides insight into the location and morphology of the fields within the corridor, the discontinuous nature of the four-segment presentation does not allow easy identification of the transitions of the interference patterns or the trends in the field plots along the corridor length. A second presentation format was developed to emphasize the lateral character of the

plot. Shown in figure 4.4(a-c), the map does not maintain the aspect ratio. The lateral emphasized plot, shown in figure 4.4, contained all of the data from figure 4.3 but the aspect ratio was not maintained.

The laterally emphasized format expands the width scale by a factor of 25. One unit in the Y-axis corresponded to 25 units in the X-axis. This scale will emphasize any side-to-side trends in the planar surface plot and de-emphasize any horizontal trends.

The contours near the source, within the first 10 meters on the X-axis, were aligned side-to-side. The interference patterns were oriented between the sidewalls, lateral patterns. The stacked-segment presentation of figure 4.3 clearly shows contours oriented along the length of the corridor for distances greater than 16 m from the source. In the "laterally-emphasized" format, figure 4.4, these longitudinal contours are de-emphasized and not readily perceived. Both formats are useful for understanding the morphology of the field.

The high field strengths are concentrated around the source at 850 MHz, shown in figure 4.4(a), and the field strength decreases with larger distances from the source. The complexity of the structure of the contours is lowest at 850 MHz, figure 4.4(a), but greater at 1900 MHz and 2400 MHz, figure 4.4(b) and 4.4(c) respectively. As expected the rate at which contours change is greater when the source frequency is increased.

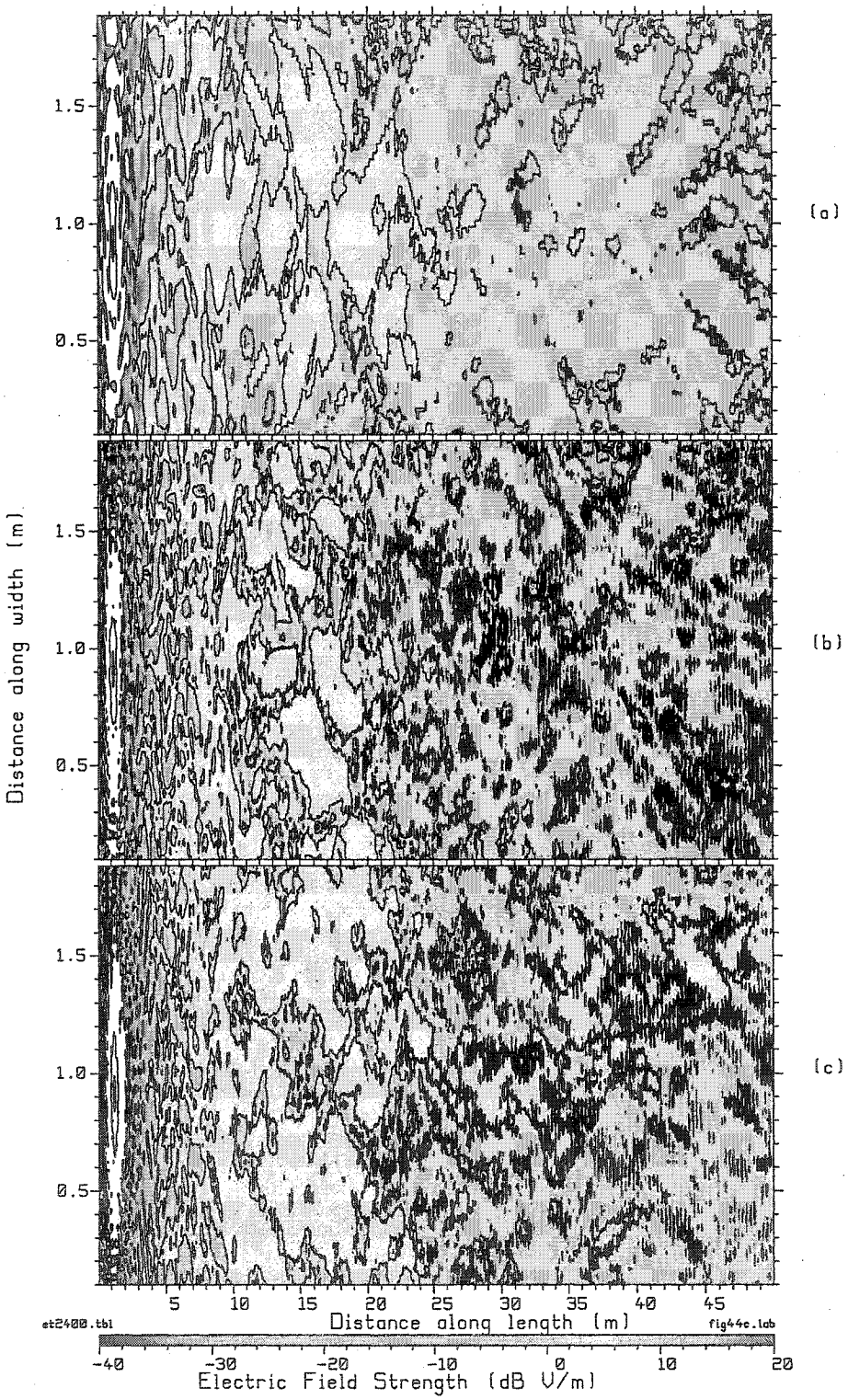

Figure 4.4 Contour maps for (a) 850 MHz, (b) 1900 MHz, and (c) 2400 MHz field simulations in corridor.

4.2 Cumulative Distributions

Figures 4.3 and 4.4 present the morphology of the fields. The data was used to derive the cumulative probability distribution of figure 4.5 by the methods described in section 2.5. The cumulative probability distribution provides information on the probability of encountering particular field strength.

The distribution was computed, using the process discussed in section 2.5, by dividing the planar surface into a grid of 3.2 by 3.2 squares. The value of the field at the center of each square was the value for that small subsurface. The number of squares with a particular value divided by the total number of squares provided a probability distribution based upon the fraction of the total planar surface area that contained a particular value. This probability distribution was used to compute the cumulative distribution, or distribution, of the fields found on the plane.

The distribution of the simulated fields within the corridor at 850, 1900 and 2400 MHz on a planar at 120 cm above the floor is plotted in figure 4.5 for field values from 0 to 10V/m. The distribution indicates that at 850 MHz, little over 2% of the fields are over 10 V/m and that around 9% of the fields are above 3 V/m over the entire corridor surface area at 120 cm height. Since the distribution was based upon the fraction of the total planar surface that had a field strength less than or equal to the given value, 9% of the fields were above 3 V/m indicated that 9% of the total planar surface area of the corridor, based upon the 3.2 cm by 3.2 cm grid, had field strength above 3 V/m.

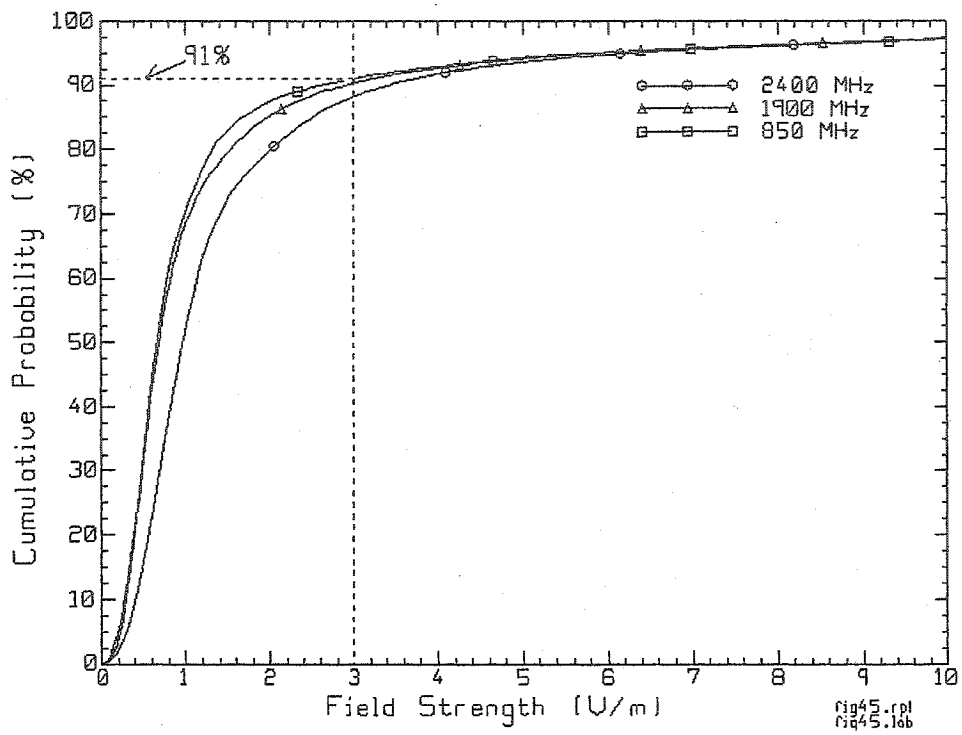

Figure 4.5 Distributions of simulated fields in corridor at 850, 1900, 2400 MHz.

The approach to assess the potential for electromagnetic interference based on planar surface computations differs from the trajectory approach in that residuals are not used. The distributions for the entire plane and the planar surface plots were used instead.

4.3 EMI Risk Based on 850 MHz Simulations

The potential for electromagnetic interference within a hospital corridor was computed for the case of a 600 mW, 850 MHz source located in the same position as above. The interference risk for a device susceptible to fields greater than 3 V/m and the risk for a device susceptible to fields greater than 10 V/m were investigated for the following cases: The case of no separations being applied, the case minimal

separations based upon free space propagation, and the case of minimal separations based upon the IEC standard.

The previous section's planar surface plot shows that the highest fields are found around the source and that fields near the middle of the corridor tended to be higher than fields near the walls. The cumulative distribution indicates that 9% of the corridor planar surface area had fields above three volts per meter. In figure 4.6 (a), the regions that contain field strengths greater than 3 V/m are shown in white.

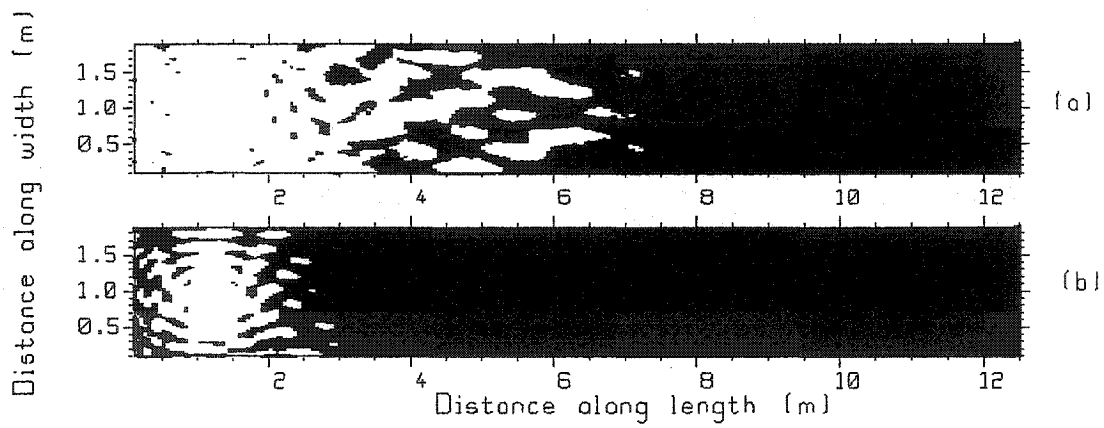

Figure 4.6 EMI plots regions with fields in white (a) over 3 V/m and (b) over 10 V/m

The white regions were extensive for distances as far as 4 meters along the length of the corridor. From 5 to 6 meters along the corridor the white regions occur around the middle of the corridor. The interference patterns tend to align longitudinally within the corridor after 4 meters. Longitudinal interference patterns tended to have higher fields near the middle region of the corridor and lower fields near the sidewalls. The white regions of field strength greater than 3 V/m did not occur past 7 meters along the corridor, which is about 6 meters from the source. The white regions tended to be more common near the middle of the corridor than near the sidewalls.

In figure 4.6 (b), the regions of the corridor that had field strengths greater than 10 V/m were shown in white. The white regions were confined to areas within 2 meters of the source, the first 3 meters of the corridor. The interference pattern near the source was aligned with the sidewalls; this alignment had strong fields near the end walls.

If a minimal separation policy were to be applied, a region around the source would be forbidden to susceptible medical devices, as shown in figure 4.7. That is, such devices would not be allowed to operate within this region. In order to determine the potential EMI risk in such situations, the field distributions for regions outside of the minimal separation zone were computed. The minimal separations were computed using free space and the IEC standard for devices of 3 V/m and 10 V/m immunities.

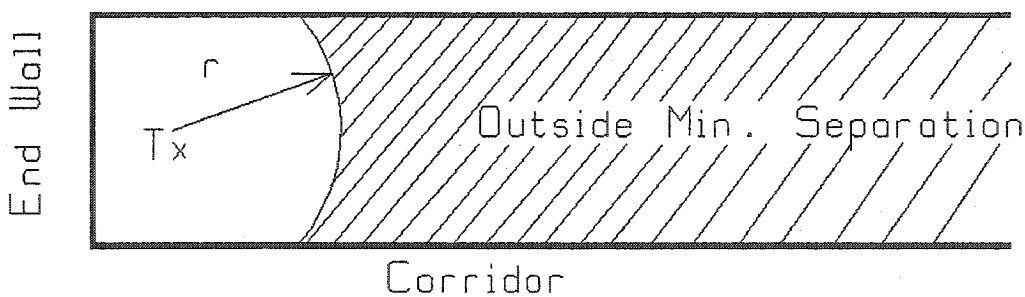

Figure 4.7 Schematic of minimal separation (r) around transmitter (Tx) in hospital corridor. Hatched region used for computation of risk of EMI when minimal separation of distance "r" used.

The values of minimal separation and EMI risk are given in table 4.1. The separation distance varied from 5.9 meters when using the IEC standard for devices with 3 V/m immunity to 0.6 meters when using free-space based minimal separations for devices with 10 V/m immunity. The risk of EMI is computed directly from the distribution of

fields outside of the minimal separation region. Figures 4.5 and 4.8 contain the distributions used to create this table. The risk of exceeding 3 V/m, according to figure 4.5, is 9% at 850 MHz and the risk of exceeding 10 V/m is 2.5% when no EMC policy is employed. The distributions used for the different minimal separations at 850 MHz are shown in figure 4.8 (a). When using minimal separations based on free space and 3 V/m immunity, regions further than 2 meters from the source are used, the risk of exceeding 3 V/m is 3.4%. Minimal separations based on free space with 10 V/m immunity require 0.6-meter separation and reduce the risk of exceeding the 10 V/m immunity to 0.63%. The IEC-based minimal separations require 5.9 meters separation for devices with 3 V/m immunity and the risk of EMI is 0.03% at this level. For devices with 10 V/m immunity the separation is 1.8 meters and the risk of EMI is nearly zero.

AT 850 MHz the risk of EMI is highest when no policy is applied but there is no restriction on the possible placement of medical devices within the corridor relative to the source. Using free-space based minimal separations reduces the risk but restricts the available space for medical devices within the corridor. The more conservative IEC based minimal separations further reduces the risk to less than 1% but also reduces the available corridor space even more than free-space based minimal separations.

The morphology from figure 4.6 indicated the location and structure of the higher field strengths based on the interference patterns within the corridor. One feature is that high field strengths occur more frequently near the middle of the corridor than the sidewalls for this configuration. By using the field maps, risk of EMI may be further reduced by selecting locales that had typically lower field strengths, i.e. near the sides of the corridor.

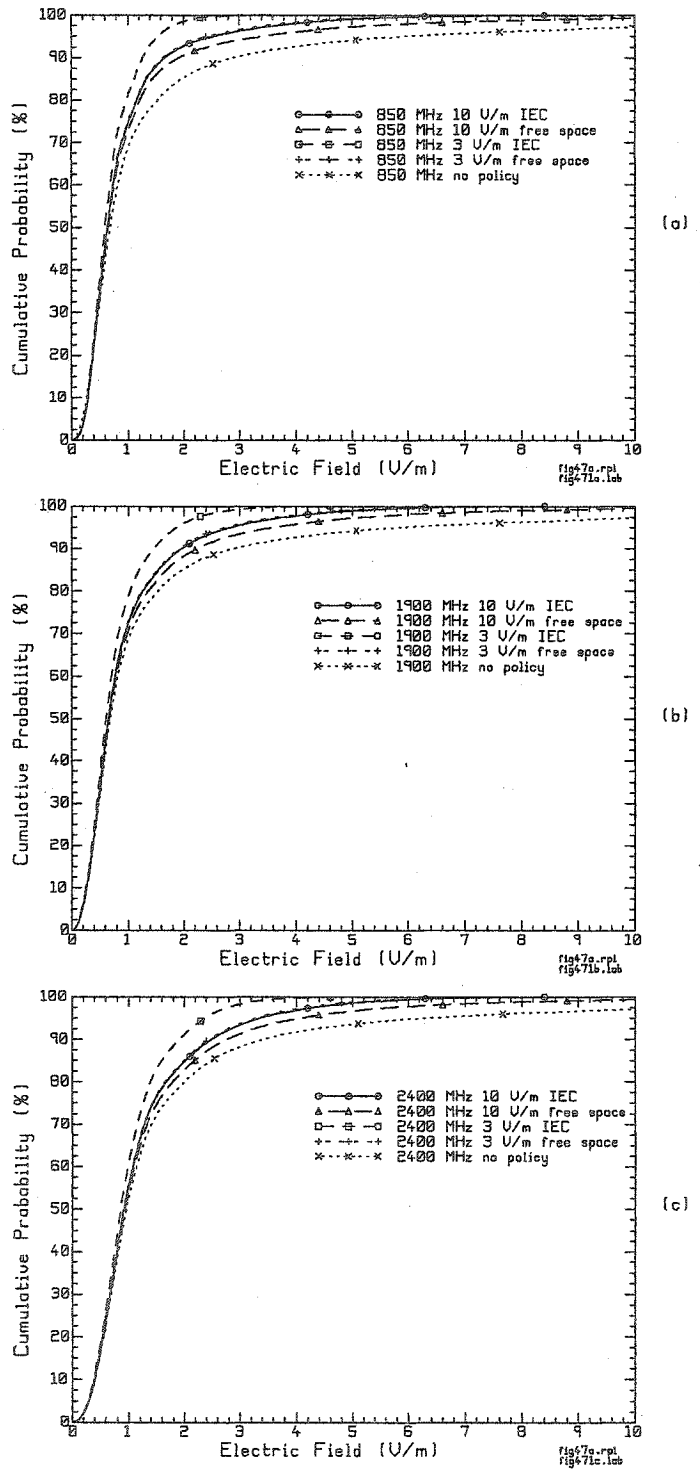

Figure 4.8 Cumulative distributions of field strengths for corridor outside of minimal separation distances at (a) 850 MHz, (b) 1900 MHz and (c) 2400 MHz

Table 4.1

Risk associated with different policies for corridor with 600 mW source operating at 850 MHz near one end of the corridor

Immunity level	Policy	Minimal Separation	% Risk
3 V/m	None	NA	9.0
3 V/m	Free Space	2 meters	3.4
3 V/m	IEC	5.9 meters	0.03
10 V/m	None	NA	2.5
10 V/m	Free Space	0.6 meters	0.63
10 V/m	IEC	1.8 metes	0

The simulations were also performed using 1900 and 2400 MHz transmitters. These frequencies were close to those allocated for digital cell phone and Bluetooth respectively.

4.4 Planar Surface Simulations at 1900 and 2400 MHz

The frequency in the simulations was changed to 1900 and 2400 MHz using the same source location and power, 600 mW, as in the 850 MHz simulations. The material properties used were also the same as the 850 MHz simulations, although the electrical properties of the walls and floor simulations should be those of the higher frequency. The contour plots of the simulated fields for all three frequencies were plotted in laterally emphasized format in figure 4.9. The same scale was used for each plot and the field range was from –40 dB V/m to 20 dB V/m.

As previously discussed the 850 MHz fields in figure 4.4 (a) are, as expected, strongest near the source and decreases in strength with separation from the source. Typically, fields are stronger near the middle of the corridor and weaker near the sides of the corridor. The contours tend to align with the end walls, lateral orientation, when near the source and gradually changed orientation further from the source. The contours at the furthest portion of the corridor are aligned with the sidewalls, longitudinal orientation, although this is de-emphasized in the "lateral" plot format.

At 1900 MHz, figure 4.4 (b), some aspects of the interference patterns change. While the highest fields are still found near the source, the orientation of the contours shifts from lateral to longitudinal around halfway along the corridor. As might be expected, the complexity of the interference patterns increases with frequency. The higher strength fields tend to occur near the middle of the corridor in the lateral sense and near the source in the longitudinal sense.

When the frequency is changed to 2400 MHz, figure 4.4 (c), the contours appear rather different than in the 850 and 1900 MHz simulations. The alignment of the contours shifts rather quickly from lateral to longitudinal, within 3 meters of the source. The field strength is generally larger for the whole length of the corridor. While the highest strength fields still occur most often near the middle of the corridor in the lateral sense, the fields near the side walls of the corridor are stronger than at the lower frequencies. The region of high field strength around the transmitter is slightly larger at this frequency than at the previous two frequencies. The impression is that the overall field strengths are slightly larger.

4.4.1 Cumulative Distributions at 1900 and 2400 MHz

The morphology of the fields within the corridor was studied using contour maps, which provided qualitative information into the structure of the fields. The quantitative assessment of the field structure of the simulated fields was performed using the distributions of the fields. The field strength contour maps of figure 4.4 (b) and 4.4 (c) were used to derive the cumulative distributions of figure 4.5 at 1900 and 2400 MHz respectively.

The distributions of the 850 and 1900 MHz simulated fields indicated that the behavior of the simulated fields was very close. The probability of encountering fields above a particular value was within 5% for the entire range of fields. The 2400 MHz distribution differed from the previous two for lower field strengths; more of the planar surface had field strengths between 0.5 and 2 V/m than at 850 and 1900 MHz. For example, at 850 and 1900 MHz, around 35% of the surface had fields below 0.5 V/m while at 2400 MHz only 16% of the surface had fields below 0.5 V/m. This difference of around 20% holds until around 2.2 V/m. This agrees with the observation made above that there were more "warm" areas in the 2400 MHz contour map than at the other two frequencies. At around 3 V/m the differences in the distributions is very small.

4.4.2 EMI Analysis at 1900 and 2400 MHz

The contour plots of the simulated fields for the first 12.5 meters of the corridor using thresholds of 3 V/m and 10 V/m shown for 1900, figure 4.9, and 2400 MHz, figure 4.10, are shown below. Field strengths greater than the threshold are white. The 1900 MHz simulations, figure 4.9 (a) and (b), had strong fields near the source, which

formed lateral interference patterns. Figure 4.9 (a) indicates that fields above 3 V/m exist as far as 10 meters down the corridor, which is about 9 meters from the source. The majority of the high fields occur near the middle of the corridor. The contour plot with the threshold of 10 V/m, figure 4.9 (b) indicates that only areas immediately around the source contain fields higher than the immunity level. Portions of the corridor further than 1 meter from the source do not contain field strengths above 10 V/m.

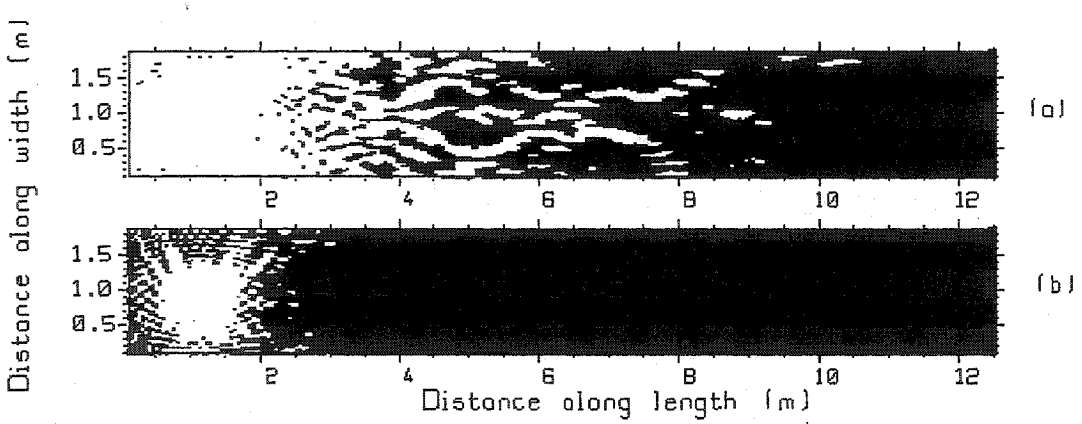

Figure 4.9 EMI plots with fields (a) over 3 V/m and (b) 10 V/m at in white at 1900 MHz

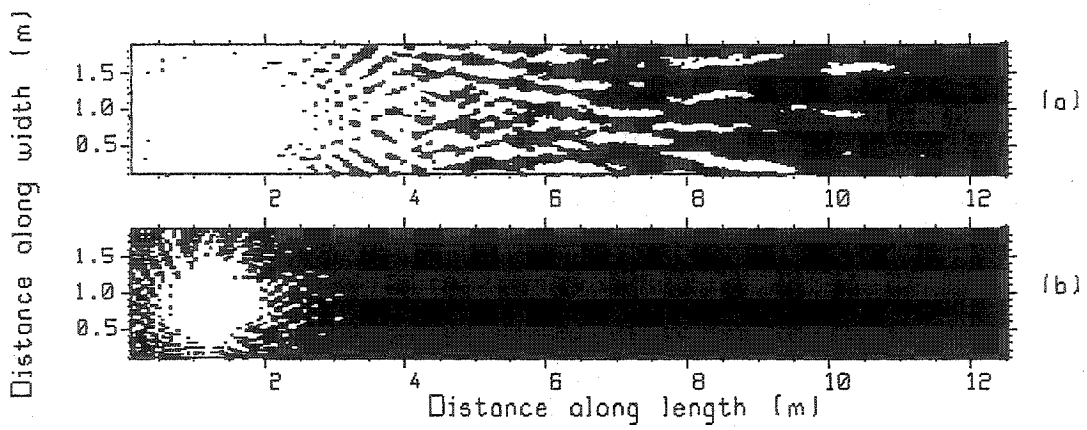

Figure 4.10 EMI plots with fields (a) over 3 V/m and (b) 10 V/m in white at 2400 MHz

When the 2400 MHz simulations are plotted using the same scale and thresholds as above, figure 4.10 (a) and (b), the overall behavior is similar to the 1900 MHz simulations. Figure 4.10 (a), detailing locations with field strengths greater than 3 V/m in white, indicates that most of the regions with field strengths above 3 V/m are located near the centerline of the corridor. There are slightly more regions further from the transmitter with higher fields than in the case of the 1900 MHz simulations. In figure 4.10 (b) the regions of field strength higher than 10 V/m, do not, however, extend very much further from the source at 2400 MHz than at 1900 MHz.

The cumulative distributions of the field strengths at both frequencies, shown in figure 4.8, are used to generate risk values for the corridor using the three different EMC policies. Table 4.2 shows the risk of exceeding immunity for a 600 mW transmitter listed according to frequency and policy. At 1900 MHz the risk of exceeding the immunity level of 3 V/m is 9.8% when using no policy, 3.4 % for free space minimal separations and 0.8% when using IEC based minimal separations. The risk of exceeding 10 V/m immunity is 2.8% with no policy, 0.5% when free space is used and nearly 0% when the IEC minimal separations are used. At 2400 MHz the risk of exceeding the immunity level is larger for 3 V/m immunity. The risk of exceeding the immunity is 12% when no policy is applied, 6.3% when free space minimal separations are used and 1.8% when IEC minimal separations are used. When 10 V/m immunity is used, the risk at 2400 MHz is the same as the 10 V/m immunity risk at 1900 MHz.

The risk of EMI is reduced by more than half when using minimal separations based on free space than no separations and nearly eliminated when using minimal separations based on the IEC standard. For devices with 10 V/m immunity levels, the difference in risk when using free space and the IEC standard is nearly the same.

Table 4.2

Risk of EMI according to policy: none, free space and IEC, minimal separations; and frequency 1900 and 2400 MHz for 600 mW dipole transmitter in corridor

Frequency	Immunity	Policy	Separation	% Risk
1900 MHz	3 V/m	None	NA	9.8
1900 MHz	3 V/m	Free Space	2 meters	3.4
1900 MHz	3 V/m	IEC	5.9 meters	0.8
1900 MHz	10 V/m	None	NA	2.8
1900 MHz	10 V/m	Free Space	0.6 meters	0.5
1900 MHz	10 V/m	IEC	1.8 meters	0
2400 MHz	3 V/m	None	NA	12
2400 MHz	3 V/m	Free Space	2 meters	6.3
2400 MHz	3 V/m	IEC	5.9 meters	1.8
2400 MHz	10 V/m	None	NA	2.8
2400 MHz	10 V/m	Free Space	0.6 meters	0.5
2400 MHz	10 V/m	IEC	1.8 meters	0

The morphological information provided by figures 4.6, 4.9 and 4.10 indicate that the risk of encountering higher fields is greatest near the source and along the centerline of the corridor. In order to further reduce the risk of EMI, medical devices should be placed near the side walls when the source is located near the end wall. The interference patterns were aligned obliquely to the sidewalls for distances from 4 to 10 m and the bands of higher field strength would drift across the corridor cross-section indicating that occasionally high field strengths are near the side walls.

The change in frequency effectively changed the electrical distance between the source and the walls, floor and ceiling of the corridor. The next section investigates

how the source location relative to the end wall affected the field strength values within the corridor at 1900 MHz.

4.5 Variation of Source Location.

This section examines the fields in the corridor for the different locations of the source relative to the end wall in figure 2.1. The choice of the source location is shown to have a significant effect on the field strengths found in the simulations. To provide some insight into the effect of source placement on the results from simulation, the corridor model used for the 1900 MHz simulations was modified. One source location was chosen to provide a strong interference pattern along the center of the corridor. A second location was chosen to make the fields weak one the corridor centerline. The contour plots for these two configurations were compared with the contour plot using the 1.2-meter wall separation data from the previous section.

The source has an image in the glass block wall at "A" in figure 4.1. The distance of the source from the glass-block wall controls whether an observer at some distance along the corridor "sees" the fields of the source and the image "in phase" or "out of phase". The image in the glass-block wall is approximately 180 degrees out of phase with the source, if the source is positioned at a distance approximately equal to a multiple of the half-wavelength for the glass-block wall, then an observer further along the corridor sees the source field plus the image field out of phase and they cancel. Conversely, if the source is an odd multiple of the quarter wavelength from the glass-block wall, the source field and image field are in phase and add. Distances close to the value of 1.2 m, the distance used in the previous sections, were used for these simulations. It was found that with the source 1.1875 m (7.52 wavelengths) from the wall, the field along the centerline is small. Conversely, with the source

1.225 m (7.76 wavelengths) from the wall, the centerline field is strong. The difference between the distances from the end wall is 0.24 wavelengths, very close to a quarter wavelength distance. The conversion of meters to wavelength at 1900 MHz is one wavelength is equal to 15.79 cm.

Figure 4.11 contains contour plots of the fields on a planar surface at the same height as the 1900 MHz source for three transmitter locations: 1.1875 m (a), 1.2 m (b), and 1.225 m (c) meters from the wall. With the source 1.1875 m from the end wall, the fields in the corridor are much smaller than with the source 1.225 m from the end wall. The field of the "in-between" distance of 1.2 m are much more like those at 1.1875 m than at 1.225 m. The "hot region" with fields greater than 10 dB V/m extends to about 5 m for a source separation of 1.1875 m and 1.2 m; but for 1.225 m the "hot" region extends much further, to about 10 m along the corridor. Clearly for EMC purposes, the separation of the source to the glass-block end wall is a very significant factor.

The three configurations had the following features in common: the highest field strengths were closest to the source and the field strength declined with distance from the source. The larger fields tended to occur near the center of the corridor and the weaker fields tended to occur near the sidewalls. As in the previous example, the interference patterns tended to align laterally when near the source and shift to align longitudinally as the distance from the source increased. The regions with weaker fields had interference patterns with higher structure than the regions with higher fields. The exception to this observation was the regions around the source.

The contour maps provided, as seen in section 4.1, details of where the field strength was high and where the field strength was low. Contour maps do not provide the

information on the proportion of the total surface with high or low fields. In order to obtain quantitative information about such proportions, cumulative distributions of field strength were computed for the three source locations.

4.5.1 Cumulative Distributions for Different Source Locations

The next step is the quantitative comparison of the of the field strengths for the three cases. This was done using the distributions of the field strengths for the planar surfaces. Figure 4.12 shows the cumulative distribution curves for the three source distances at 1900 MHz.

From figure 4.12, the distributions of the fields for the 1.1875 and 1.2 meter configurations were very close for the range from 0 to 10 V/m. This reinforced the observation that the contour plots seemed to have comparable interference patterns. The distribution of the 1.225-meter configuration differed in the range from 0 to 3 V/m. The corridor was "hotter" with a source separation of 1.225 m to the end wall. This is seen in figure 4.13 as follows. With a 1.225 m separation, 50% of the points in the corridor were above 1 V/m, but with the source 1.1875 or 1.2 m from the end wall only 31.7% were above 1 V/m. The difference between the distributions decreased as the field values increased. The probability of encountering fields less than or equal to 3V/m was 88.7% for the 1.225-meter separations and 90.4 % for the other two configurations. The distributions were virtually indistinguishable above 5 V/m. The variation of source location affected the distribution by changing the proportion of lower strength fields encountered, but did not substantially change the proportion of higher strength fields.

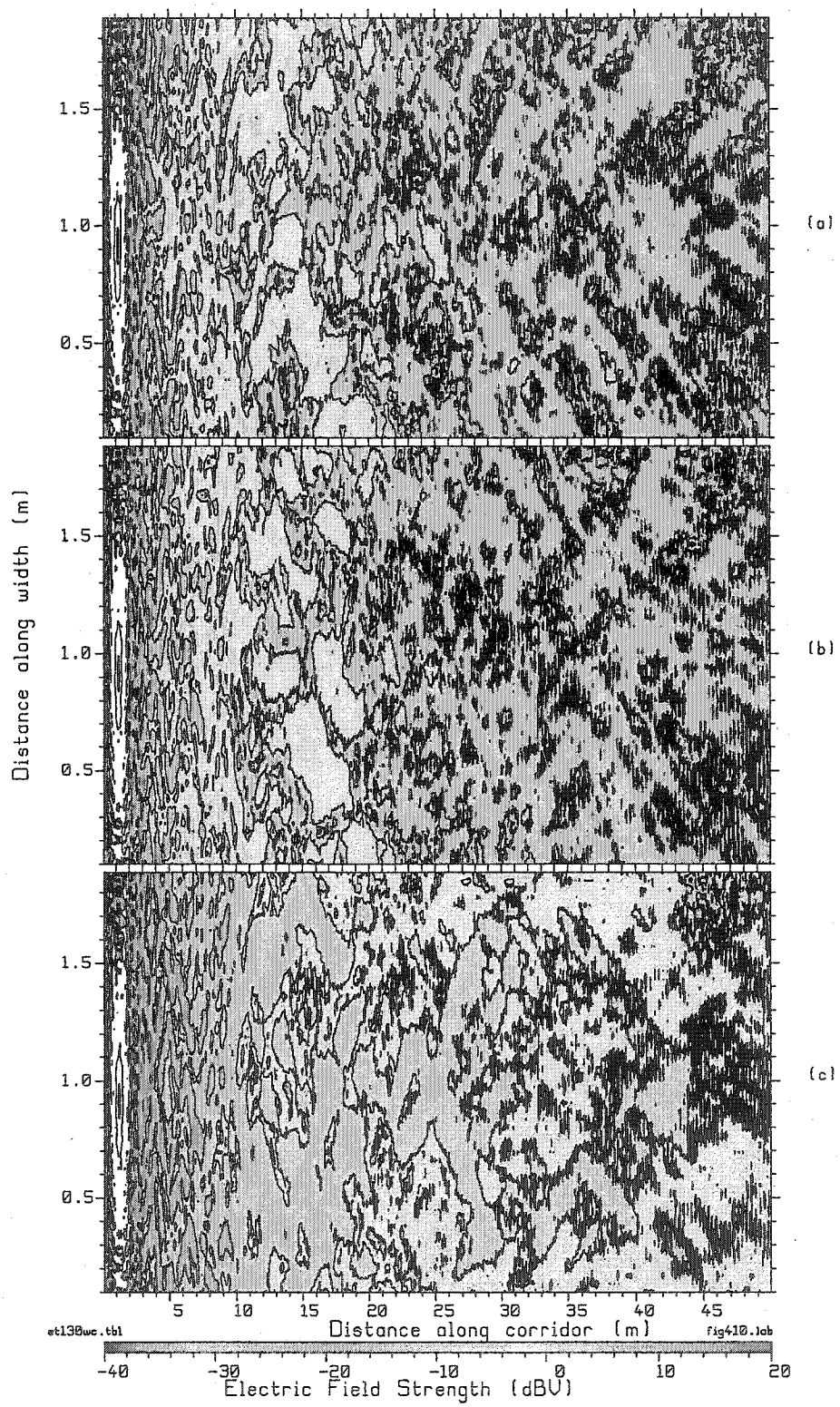

Figure 4.11 Contour maps of field strength 600 mW source at (a) 1.1875 (7.5 λ), (b) 1.2 (7.6 λ) and (c) 1.225 m (7.76 λ) from end wall of corridor

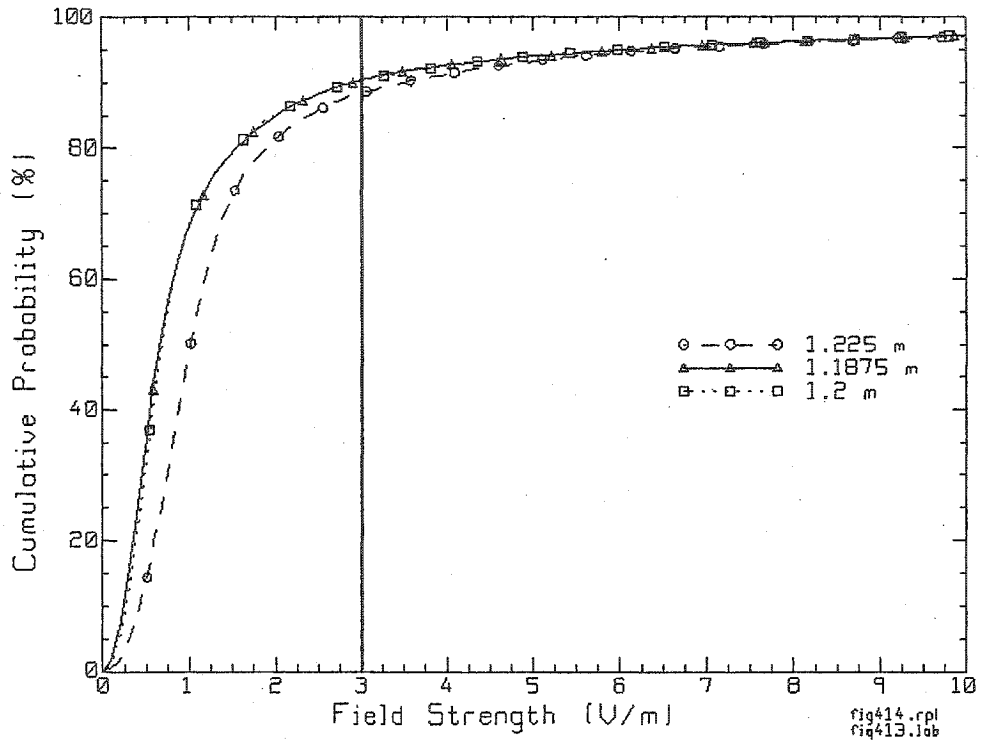

Figure 4.12 Comparison of distributions of fields within corridor at 1900 MHz with source located at: 1.1875, 1.2 or 1.225 m from glass block wall

4.5.2 EMI Risk for Different Source Locations

The risk of EMI was computed using the distributions from section 4.5.1 and along with the minimal separations is found in table 4.3. The information about the risk using 1.2-meter separation between the transmitter and the end wall is found in table 4.1. Note that an immunity level of 3 V/m is above the region in figure 4.12 where the cumulative distributions for the three distances are very different. Thus, in table 4.3, the risk for the three EMC policies is not very different for the two source locations. When using the "free space" policy, the risk of EMI is 4% with 1.1875 m and

increases to 5.7% at 1.225 m. This moderate increase in EMI risk is surprising considering how different the corridor fields are in figure 4.11.

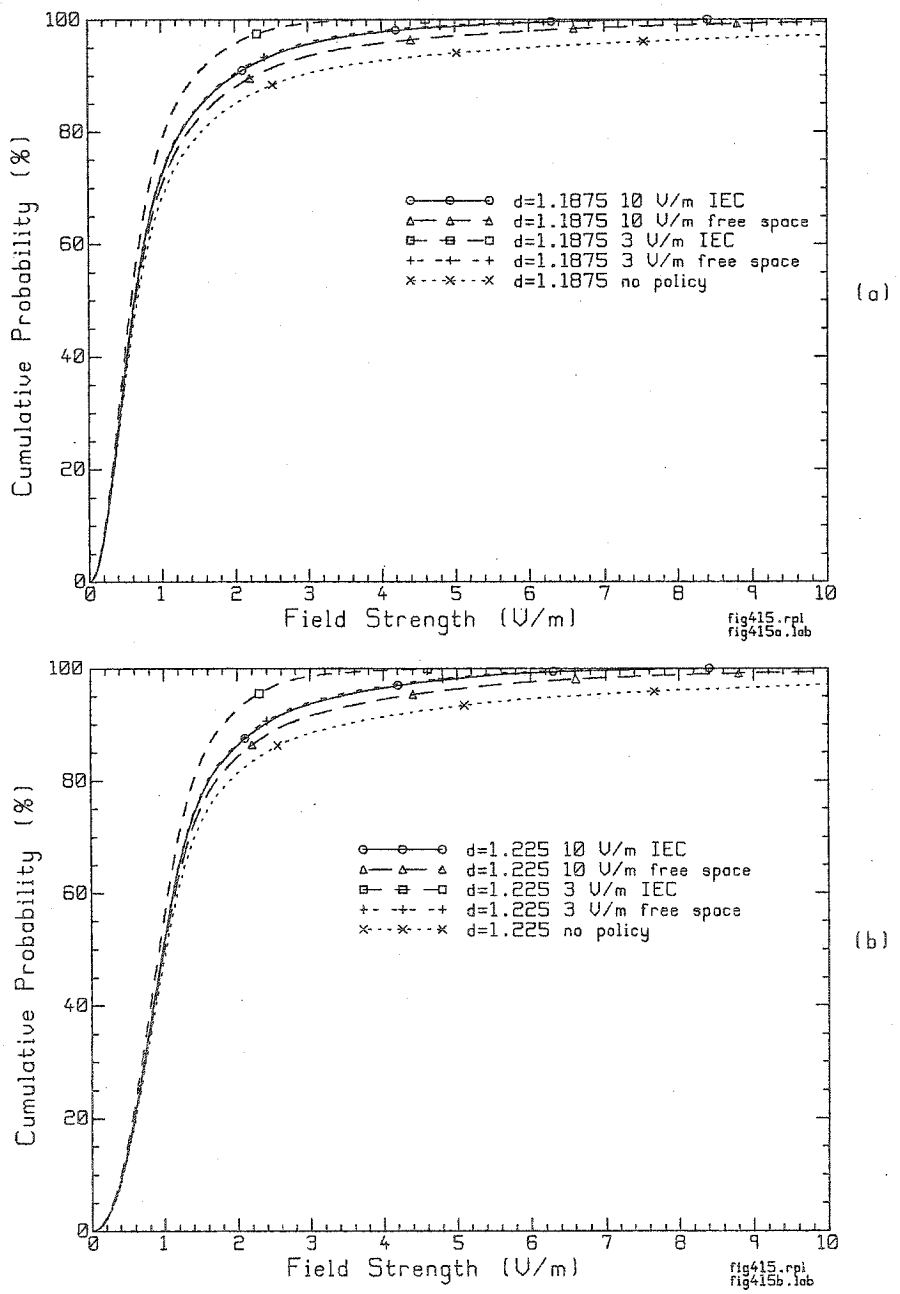

Figure 4.13 Cumulative distribution of field strength for source location (a) 1.1875 and (b) 1.225 m from left wall using different minimal separations

The distributions in figure 4.13 are nearly identical for field strengths under 1 V/m. The no policy curve is the lowest curve, indicating a larger proportion of higher field strengths than the other curves. In descending order the curves with proportions of high field strengths are: 3 V/m free space 3 V/m IEC, 10 V/m free space and 10 V/m IEC has the lowest proportion of the total planar surface area with high field strengths. This behavior is the same for both the 1.1875 and 1.225 m spacing. As in the previous section, the risk of EMI was computed using cumulative distributions for 3 EMC policies, none, free space minimal separations and IEC separations for two immunity levels, 3 V/m and 10 V/m. The risks and minimal separations are shown in table 4.3. For the 1.1875 m spacing from the end wall, using no policy the risk of exceeding 3 V/m is 9.4% and the risk of exceeding 10 V/m is 2.8%. When using free space minimal separations the risk of exceeding 3 V/m drops to 4.0% and the risk of exceeding 10 V/m is reduced to 0.45%. When using IEC minimal separations the risk of exceeding 3 V/m is 0.62 while the risk of exceeding 10 V/m is nearly zero. The risk when the source is 1.225 m is generally higher, using no policy the risk of exceeding 3 V/m is 11.4% and the risk of exceeding 10 V/m is 3.8%. Free space minimal separations reduce the risk to 5.7% of exceeding 3 V/m and 0.6% of exceeding 10 V/m. IEC minimal separations further reduce the risk to 1.4% for exceeding 3 V/m and nearly zero risk of exceeding 10 V/m.

The risk of EMI was within two percentage points for all of the configurations for each of the policies. The risk levels of the 1.225-meter separation were slightly higher than the other configuration risk levels for every policy. In all cases, the usage of minimal separations reduced the risk of EMI by at least half compared to no EMC policy. The minimal separations based on free space were less effective for devices with 3 V/m immunity level than the IEC standard, but the 10 V/m immunity devices

had nearly the same level of protection using either the free space or the IEC based minimal separations.

Table 4.3

Risk associated with: no EMC policy, free space separations and IEC separations for source 1.1875 and 1.225 m from end wall

Immunity Level V/m	Policy	Minimal Separation (m)	% Risk d=1.1875 (m)	% Risk d=1.225 (m)
3	None	NA	9.4	11.4
3	Free Space	2	4.0	5.7
3	IEC	5.9	0.62	1.4
10	None	NA	2.8	3.8
10	Free Space	0.6	0.45	0.60
10	IEC	1.8	0	0

4.6 Identification of Distribution of Fields

A preliminary attempt to relate the distributions of the interference pattern field strengths of the simulated fields at 850, 1900 and 2400 MHz to known distributions (e.g. Gaussian, Log-Normal, Rayleigh) will be performed in this section. By associating a known distribution to the field strength values, a closed form expression may be used to characterize the data. Rayleigh distributions were used as initial guesses at the cumulative field distributions, *F(X)*, on the planar surface simulated within the corridor using,

$$F(X) = 1 - e^{\left(\frac{X^2}{2\sigma}\right)} \qquad \ldots(4\text{-}2)$$

with X being the random variable field strength and σ the standard deviation of X [27].The parameter used for the cumulative distribution function for the Rayleigh distribution was the inverse of twice the variance [27]. The distribution of the simulated data was plotted against the test distribution using 100 bins for each distribution, as shown in figure 4.14. The smaller the deviation from the ideal match line, the closer the distributions were.

After using the above-mentioned graphical technique to obtain relatively close matches in distributions, the Kolmogorov-Smirnov test was used to test for matches [27, 80]. This test uses the maximum absolute value of the difference between two distributions $F_O(X)$, the distribution under test, and $F(X)$, the known distribution, for all values of X. The maximum absolute difference "D" is defined by:

$$D = \max\left|F_O(X) - F(X)\right| \qquad \ldots(4\text{-}3)$$

If the difference is less than or equal to the appropriate constant, the two distributions are considered the same with a certain confidence level. This test used 100 samples and the confidence level was determined using the maximum difference. If the difference was less than or equal to 0.05 the two distributions are considered to be the same with over 99% confidence. The tests were not conclusive for the entire data series, but if the high field strength regions around the source were excluded, a match with over 99% confidence was obtained in all three cases.

The above comparison indicates that with the exception of the region immediately around the source, within 60 cm of the source, there is a high degree of confidence

that the Rayleigh distribution can predict the statistical behavior of the field strength within the corridor. This confirms previous work in which signal fading due to scattering from various structures is associated with Rayleigh distributions [47, 52, 67].

Table 4.4

Rayleigh distribution parameters for simulated fields in corridor

Frequency	Parameter	Confidence
850 MHz	0.5	99.7%
1900 MHz	0.5	100 %
2400 MHz	0.7	100 %

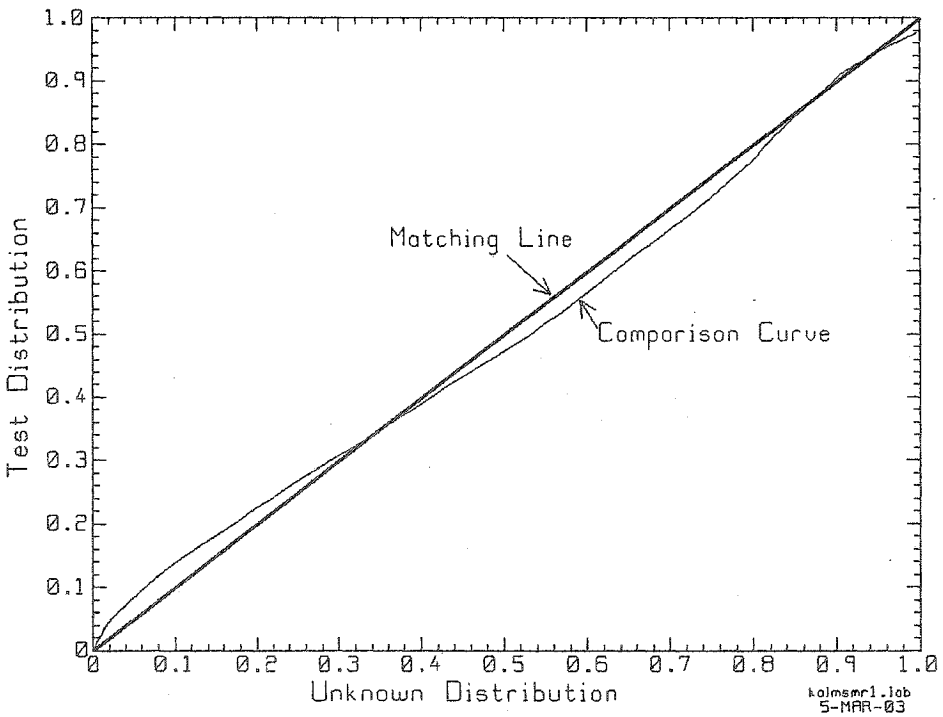

Figure 4.14 Relating field distribution with known distributions. Best match Rayleigh using parameter of 0.5 for 850 MHz distribution using 100 bins.

4.7 Summary

The use of planar surface plots and distributions of the field strength of simulated field data provided useful characterizations of the electric field within a corridor. The morphology data found in the surface plots was used to identify locations where high field strengths occurred and displayed how trends in the interference patterns varied within the corridor. The interference patterns tended to align with the sides of the corridor when near the source and to align with the end walls when further from the source.

The distributions of the field strengths provided quantitative information about the simulated fields. This information was used to compare the simulated fields for different frequencies and configurations within the corridor.

The operating frequency of the simulated transmitter was chosen to be 850, 1900 and 2400 MHz with the source 1.2 m from the end wall of the corridor. The increase in frequency caused the interference pattern to align with the end walls closer to the transmitter. The distributions of the fields were similar for the 850 and 1900 MHz simulations, but the 2400 MHz simulations generally had higher field strengths for regions further than 4 meters from the source. The distributions of field strengths 3 V/m and higher were the same for all three frequencies.

The location of the transmitter relative to an end wall was varied so as to produce minimum and maximum fields along the middle of the corridor. The contour plots indicated that the relative position of the source did not affect how far away from the source the transition in orientation of the interference patterns occurred. The highest

field strengths tended to occur close to the middle of the corridor in all three configurations.

The distributions of the field strengths indicated that the configuration that had a maximum along the middle of the corridor had generally larger field strengths than the other two configurations for distances further than 4 meters from the source. The distributions were very close for fields greater than 3 V/m but the cumulative distribution of field strength values from 0 to 3 V/m varied with source location relative to the end wall. The configuration that produced the maximum along the corridor centerline also produced higher field strength values along much of the planar surface.

The risk of electromagnetic interference was quantified for different policies, source locations and frequencies. The usage of minimal separations, free space or IEC based, reduced the risk of radiated EMI by at least half. The IEC based minimal separations were the most effective at reducing the EMI risk for devices with 3 V/m immunities, the free space based minimal separations performed about as well as the IEC based minimal separations for devices with a 10 V/m immunity level.

The next section will discuss electric fields within rooms. The characterization processes used in chapters 3 and 4 will be used for data obtained from measurements and simulations within a small clay-block walled room at 850 MHz.

Chapter 5

Room Measurements and Simulations, Morphology and Statistics

This chapter presents the results of measurement and simulation surveys in a small clay-block walled room. The data is then used to compute the risk of an EMI incident for devices with 3 V/m or 10 V/m immunity. Figure 2.12 (pg. 37) is a floor plan of the room. The source, labeled "C" in the figure, was located off the diagonal near the bottom right hand corner of the room. The fields due to a 600 mW source located near one corner of the room and operating at 850 MHz were measured and simulated using GO_3D.

The measurements were performed using the techniques discussed in section 2.3. The planar surface measurements were performed on a grid composed of 3.2 cm side length squares as shown in figures 2.13 and 2.14 (pg. 39). The results of the measurements and simulations were displayed using contour plots with 10 dB contours such as figure 2.15. (pg.40) The measurements were paralleled by a series of computer simulations that used a relatively crude model of the rectangular room. The room was modeled as a 3 x 3 m closed structure with clay-block walls. Windows, entrance alcove and doors were omitted from this model. Figure 2.15 shows the measured and simulated field strengths at 850 MHz. For both the measured and simulated cases, the highest field strengths (over 25 dB V/m) are, as expected, near the source. Intermediate field strengths, between 10 and 20 dB V/m are found at many locations on the planar surface, not just near the source. The fields, especially in the

simulations, show a standing-wave pattern, due to strong reflections from the clay-block walls. Figure 2.21 (pg. 50) shows that, in the simulation, the clay-block wall has a reflection coefficient of about 0.8 for normal incidence. The measured data, figure 2.15 top, does not show as prominent an interference pattern across the lower portion of the measurement surface. This suggests that the walls in the actual room did not reflect as strongly.

The simulation shows a radial structure of maxima and minima approximately oriented on the lower right corner of the room in figure 2.13. This can be understood in terms of the image sources in the two walls, which form a corner reflector structure. There are, effectively, four sources that radiate to form a complex pattern of peaks and minima. Hence in the simulation, there is a maximum in the directional pattern that strikes the left wall at about 0.5 m from the bottom of the figure. A second maximum strikes the left wall about 1.2 m from the bottom of the figure. Conversely, there is a well-defined minimum that strikes the top wall at 2.5 m from the left wall of the figure. The directional pattern is not as clearly seen in the measured data, likely because the actual walls were not as reflective as in the simulation model.

While the morphology in figure 2.15 (pg. 40) provides information about the location of high or low field strengths and information about the trends of the fields, the statistical distribution of the fields is required in order to determine the proportion of the surface that contains field strengths above a particular level. The distribution of

the measured fields and the simulated fields is used rather than the distribution of the residuals of the trends since the data is not related to a particular trajectory.

The cumulative distribution of the field strength, shown in figure 5.1, obtained using the methods discussed in section 2.5.4, is used to characterize the field behavior on the planar surface. Despite the relatively simple model, (door, alcove and window omitted), and despite the difference in wall reflection suggested by figure 2.15 (pg. 40), the measured and simulated distributions are quite similar. From the distributions in figure 5.1, around 20 % of the surface had fields below 3 V/m, and around 78% of the surface had fields below 10 V/m.

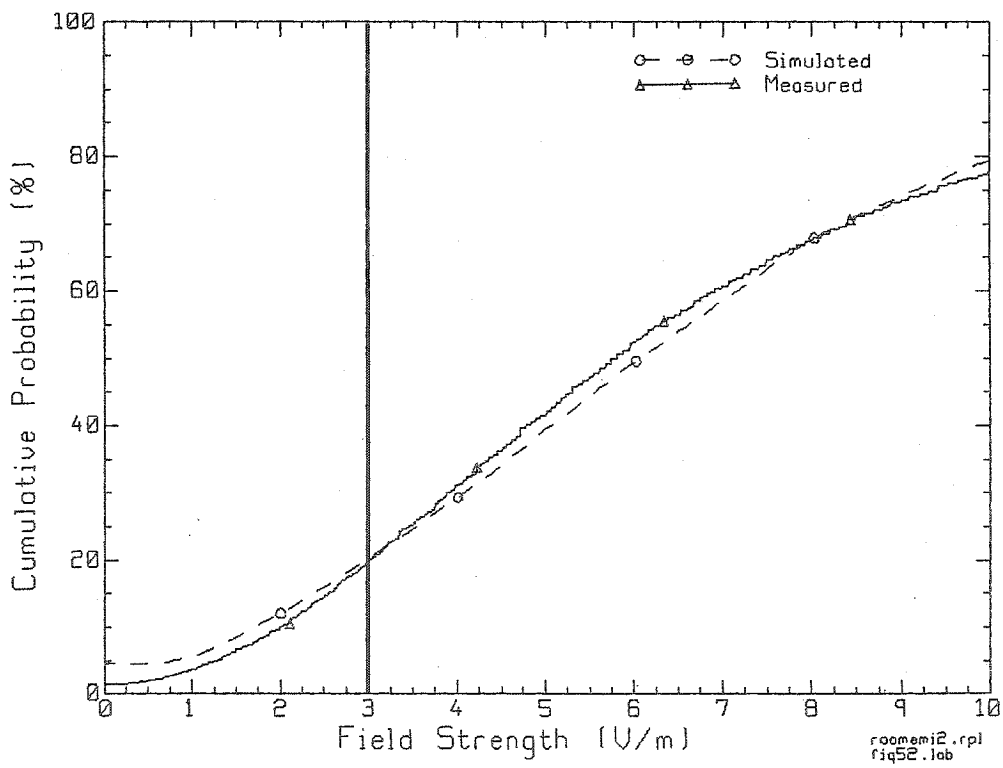

Figure 5.1 Distributions of measured and simulated room fields at 850 MHz

5.1 Trajectories in Small Clay-Block Rooms

Measured and computed trajectory data for the two paths in figure 2.16 (pg. 42) are plotted in figure 2.17 (a) and 2.17 (b) (pg. 43). Path "A" travels approximately radially away from the source to the opposite corner in figure 2.16 is plotted in figure 2.17 (a). Near the source, located at 0.65 m along the path, the measured field strength increases to 37 dB V/m while the simulated field strength is over 40 dB V/m. Further from the source, after 1 meter along the path, both the measured and simulated field strength varies from 0 to 20 dB V/m. While the general shape of the measured and simulated fields are quite close, the locations of the peaks and nulls along the path do not match up. This is most likely due to the lack of detail in the simulation model of the room.

Path "B" is roughly equidistant from the source, figure 2.17 (b), with field strength varying from 0 to 20 dB V/m along the path. Since the points on the path are roughly equidistant from the source, the path loss exponent is approximately zero. The field strength varies due to the constructive and destructive interference of rays at different points in the room. The measured and simulated field strengths have the same general behavior, but the locations of the peaks and nulls along the path do not align. As in the case of the trajectories moving away from the source, these differences may be explained by lack of detail in the model.

Regression lines were fitted to the data in figure 2.17 (a) using the same methods in section 2.5.1. The regression lines and the associated data for both the simulated and measured fields in the room are shown in figure 5.2 (a). While the measured field strength is slightly lower than the simulated field strength for much of the path, the difference between the measured and simulated fields is small, less than 5 dB V/m in most cases. The field strength is over 3 V/m for most of the path, and is 10 V/m near the source and at a few locations further along the path, 2 and 3.7 m from the source for simulated fields and 3.1 and 3.7 m from the source for measured fields. The power law models based on the regression lines, or trends, has different path loss exponents, n = 1.24 for measurements and n = 0.798 for simulations. While the path loss exponents are different, the curves are within 4 dB of each other for much of the path. It is worth noting that for relatively short paths, a large difference in path loss exponents does not always indicate a large difference in the field predicted by the power law model. The field varies more or less consistently about the power law model for the entire path length.

The behavior of the fields further than 70 cm from the source, located at approximately 0.65 m on the path, is investigated by removing the data between 0 and 1.4 m along the path. The power law models were re-computed using the reduced data set and the results are shown in figure 5.2 (b). The path loss exponents of the power law models are now, n = 0.891 for the simulations and n = 0.332 for the measurements. As in the previous case, while the path loss exponents are quite

different, the field strength predicted by the power law models are within 4 dB of each other for most of the path.

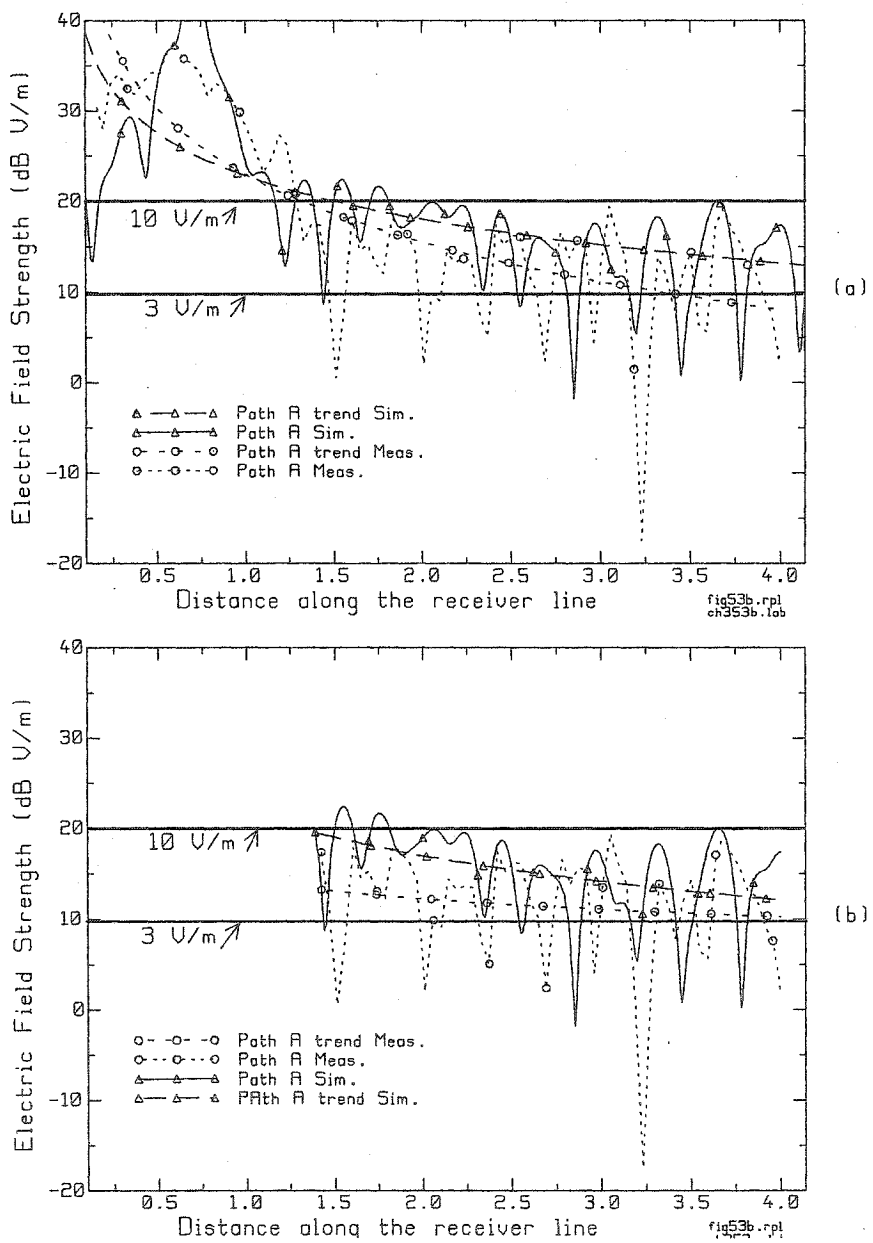

Figure 5.2 Field strength in small clay block room at 850 MHz for: (a) full trajectory and (b) trajectory further than 70 cm from source in figure 2.10.

The exclusion of the region around the source had a large impact on the path loss exponent for the measurements and a smaller effect on the path loss exponent for the simulations. The path loss exponents for both the "A" and "B" paths are shown in table 5.1.

Table 5.1

Path loss exponents for small clay block room at 850 MHz for path "A" and path "B" for measurements and simulations with 3.2 cm sampling grid on surface. Source located at 0.65 m along path "A".

Path	Data	*N*
A: $0 \leftrightarrow 4$ m	Meas.	1.24
A: $0 \leftrightarrow 4$ m	Sim.	0.798
A: $1.4 \leftrightarrow 4$ m	Meas.	0.332
A: $1.4 \leftrightarrow 4$ m	Sim.	0.811
B	Meas.	0.058
B	Sim.	0.133

The path loss exponent for measured data on path "A" is $n = 1.24$, indicating that the field strength decreases at a rate higher than free space, $n = 1$. The path loss exponent for simulations performed on path "A" produced a path loss exponent of $n = 0.798$. This would seem to indicate that the field strength declines at a lower rate in the simulations than for the measurements. However, the field strength along path "A" in figure 5.2 (a) does not show a marked difference in field strength between the simulations and measurements. Next, the path loss exponents for the portion of path

"A" further than 0.7 m from the source were obtained. The measured data produces a path loss exponent of $n = 0.332$, while the simulations produce a path loss exponent of $n = 0.811$. Again the path loss exponents are quite different but the measured and simulated field strengths, figure 5.2 (b), are close.

The field strength further than 1.5 m along the path does not decrease continuously with distance, but rather has relatively equally spaced peaks and nulls of field strength along the path. This behavior is contrary to intuition that suggests: Field strengths at locations further from the source are weaker than field strengths at locations closer to the source. This intuition is based on the assumption that the fields behave as in free space.

The path loss exponents for path "B" are $n = 0.058$ for measurements and $n = 0.133$ for simulations. These values are much smaller than those of path "A" and are suggestive of relatively constant field strength along the path. This is in accordance with the points on the path being roughly equidistant from the source. The field strength along path "B", as seen in figure 2.17 (b), varies from 0 to 20 dB V/m in a complicated fashion. The range of field strengths along path "B" is the same as for path "A" between 1.4 and 4 meters.

Using power law models to estimate field strength in small rooms such as the one discussed above is limited value since the large differences in the path loss exponent can be found for data sets that are very close in value. For this reason, EMI estimates

in rooms will be based on the distribution of the field strengths; the method used in chapter 4, rather than the power law and distribution of residual process used for EMI risk analysis in chapter 3.

5.2 EMI Risk in Small Rooms

The risk of electromagnetic interference for small clay-block walled room was assessed using information based on multiple trajectory measurements performed on a planar surface. Contour plots of the field strength provided information on the structure of the interference patterns, while the distribution of the field strengths provided quantitative information about the proportion of the planar surface that contained particular field strengths.

The structure of the interference pattern was used to identify regions where high field strengths occurred. This was done by having all regions within the contour plot with field strengths above a threshold plotted in white and all others dark. Figure 5.3 (a-d) has contour plots using this format for measured data with a 3 V/m threshold, figure 5.3 (a), and a 10 V/m threshold figure 5.3 (b). The simulated data is also plotted with 3 V/m figure 5.3 (c), and 10 V/m figure 5.3 (d), thresholds. White, "hot", regions indicate where the field strength is above the threshold on the planar surface. For example, in figure 5.3 (a) the white regions correspond to places where the field strength exceeds 3 V/m.

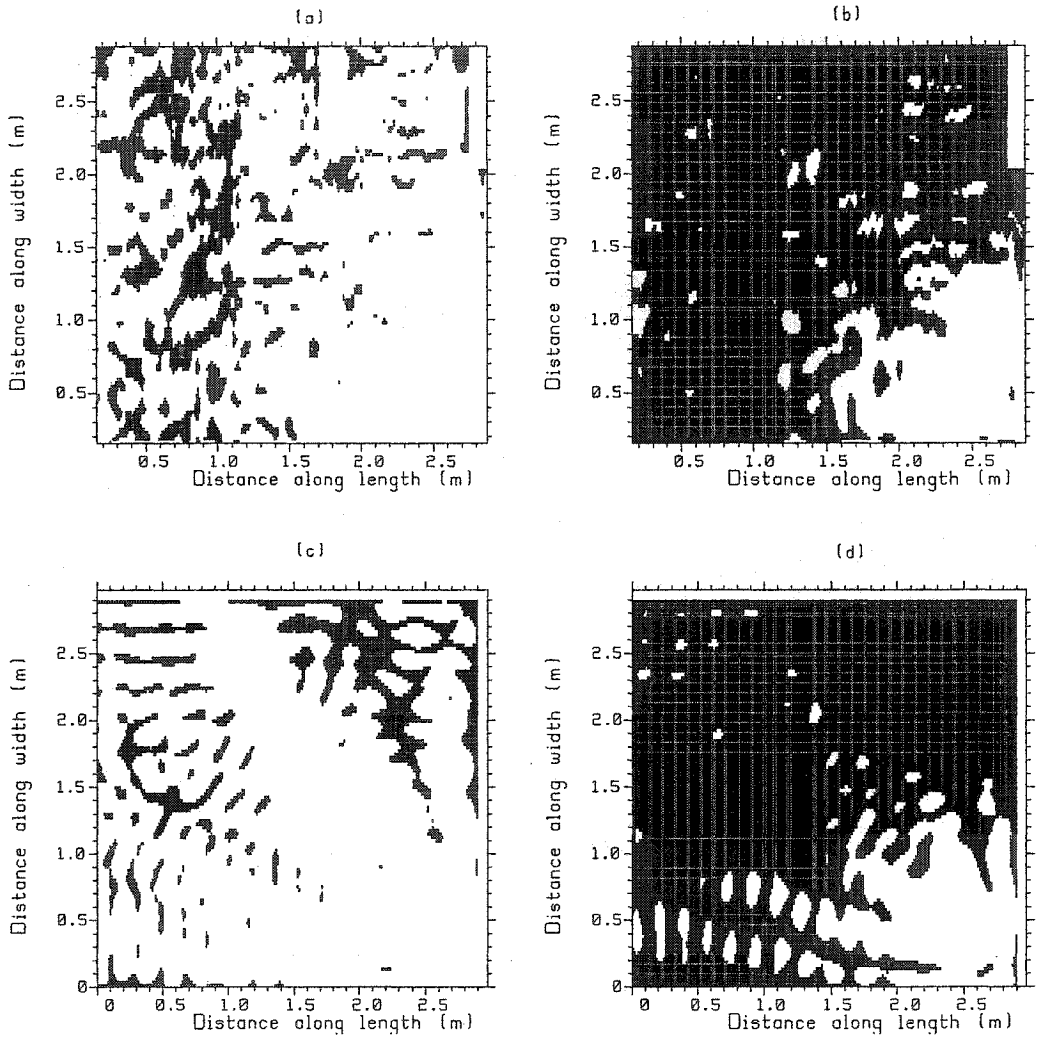

Figure 5.3 EMI plots with fields over (a) 3 V/m-measured, (b) 10 V/m-measured, (c) 3 V/m-Simulated, (d) 10 V/m-simulated, in white

In figure 5.3 (a), the field strength exceeded the threshold in most locations, including regions furthest from the source. The 3 V/m threshold plot provided insight into the structure of the interference patterns and the EMI implications for this environment. Contrary to intuition, regions further from the source did not necessarily provide lower EMI risk. When the threshold was set at 10 V/m, the immunity level of new

medical devices, the proportion of "hot" areas decreased substantially as shown in figure 5.3 (b). The areas of high field strength are concentrated near the source in the bottom right hand corner of the surface. There are some small regions where the field strength exceeds 10 V/m scattered further from the source, near the left edge of the surface from 0 to 0.5 m on the horizontal axis at 1 m along the vertical axis, near the middle of the surface from 1 to 1.5 m on the horizontal axis and 1.5 to 3 m on the vertical axis. Also, there are some locations from 1.7 to 2.2 m on the horizontal axis and 2.2 to 2.7 m on the vertical axis where the field strength exceeds the 10 V/m threshold. These small "hot" areas are scattered throughout the planar surface making the choice of a safe location difficult as being further from the source does not always insure field strength below the threshold.

The simulated fields are plotted using the 3 V/m threshold in figure 5.3 (c). As with the measured data, much of the surface area has field strengths greater than 3 V/m. Regions furthest from the source were mostly above the 3 V/m threshold, this again runs counter to intuition where further is assumed to be safer. The simulated data with a 10 V/m threshold is plotted in figure 5.3 (d). The proportion of the surface above the threshold dropped, and most of the "hot" regions are concentrated near the source. There are two sections of the planar surface where the "hot" regions extend along the entire horizontal axis. The first region is from 0 to 0.7 m and has a pattern of hot regions suggestive of an interference pattern aligned with the side walls. The second regions follows the diagonal that links the upper left and lower right corners of the figure and is approximately 0.5 m wide. The orientation of the maxima varies along

the diagonal. Near the source, the maxima tend to be oriented in a radial manner, but from 2 to 2.7 m on the vertical axis, the orientation of the maxima follows the side and upper edge.

5.2.1 Distributions of the Field Strength

The distributions of field strength on the planar surface are computed for various situations. If there is no EMC policy and a device is allowed anywhere on the surface, the distribution of the fields for the entire surface is used. If a minimal separation EMC policy is used, for example the IEC 60601-1-2 standard, then only the portion of the surface that the susceptible device would normally be allowed to operate on is used. For example, using free space separation with a device of 10 V/m immunity and a 600 mW source operating at 850 MHz, the minimal separation is 60 cm. In this situation the device is prohibited from operating within 60 cm of the source. The region within 60 cm of the source is, in this case, not used to compute the distribution of field strength. Figure 5.4 shows a schematic of the room and planar surface used in the computation of the distributions. Using the minimal separation of r = 60 cm, the portion of the planar surface used for the computation of the distribution is outside of the arc. The region outside the arc is defined as a safe region, according to the IEC standard, where the device may operate without risk of EMI. The actual risk is quantified using the distributions of field strength for the appropriate situation.

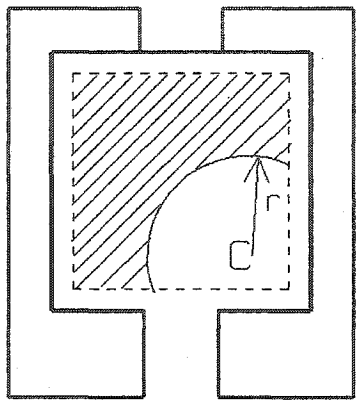

Figure 5.4 Schematic of room with source located at "C" used for computation of distribution of field strength. Minimal separation distance "r" region is white. Region where device may operate has diagonal lines. The box with the dashed line encloses the planar surface where the data is obtained.

The distributions of the fields within the room for various EMC policies were plotted together in figures 5.5 (a) and 5.5 (b). For each curve the field strength data is taken from the region outside of the arc in figure 5.4. The radius of the arc is determined by the EMC policy used. For a 600 mW isotropic source, using no policy the radius of the arc is zero, for free space and 3 V/m immunity the radius is 2 m. The IEC policy requires a 5.9 m separation, which places the device outside the room. When the device immunity level is 10 V/m the free space minimal separation is 60 cm, and the IEC separation is 1.8 m.

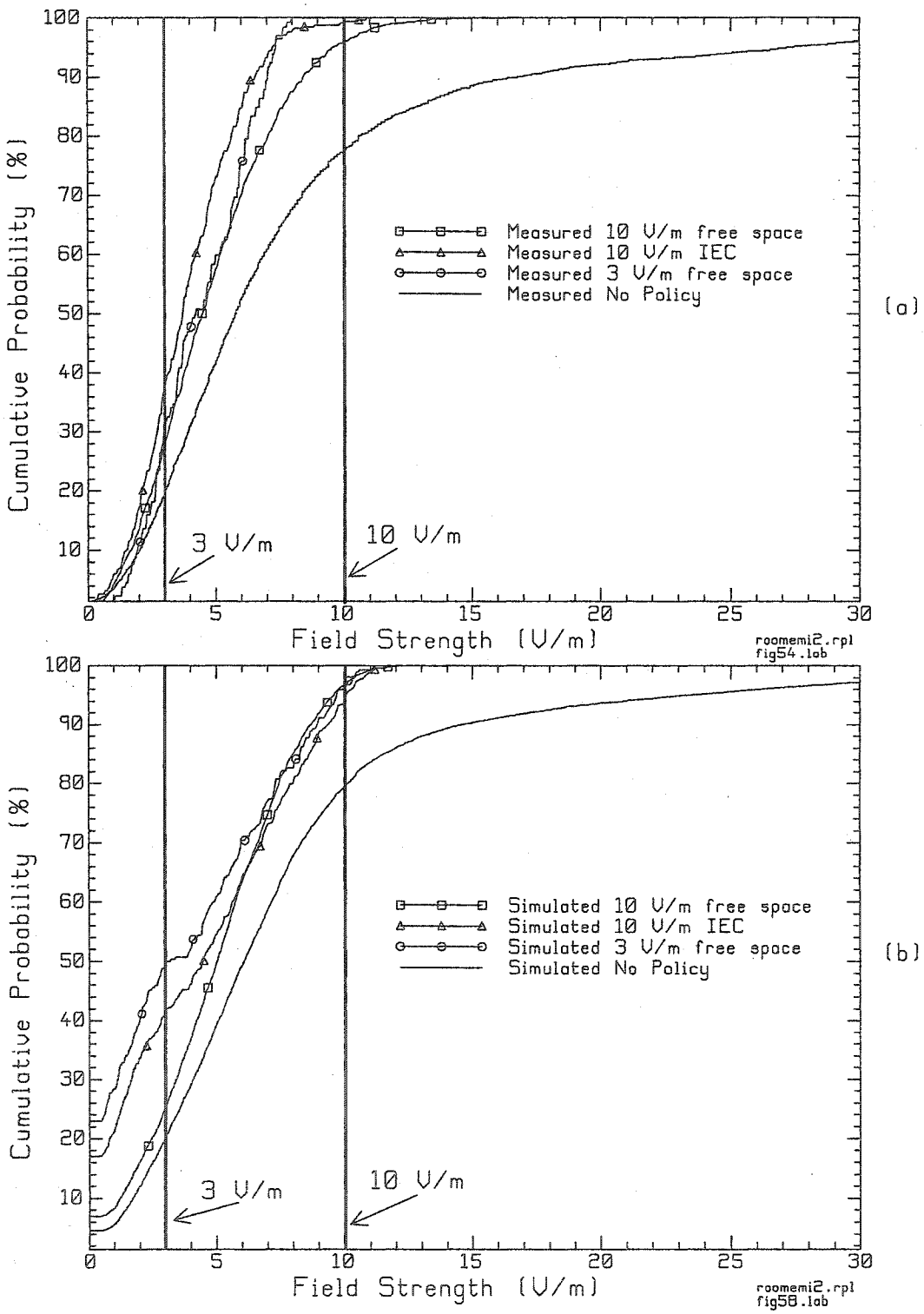

Figure 5.5 Cumulative distributions of (a) measured field strength and (b) GO simulations for small clay-block walled room at 850 MHz for different EMC polices.

The no-symbol curve in figure 5.5 (a) is the distribution of the measured field strength over the whole area inside the dashed line box in figure 2.12. This corresponds to no EMC policy where devices may be operated anywhere in the room. The lines with circles, squares correspond to the EMC policy of "free-space minimal separations" for 3 V/m and 10 V/m respectively, while the solid line with triangles corresponds to the IEC policy for 10 V/m immunity level. The distributions of the simulated fields are shown in figure 5.5 (b). The no-symbol line corresponds to no EMC policy, the lines with circles, squares correspond to the EMC policy of "free-space minimal separations" for 3 V/m and 10 V/m respectively while the solid line with triangles corresponds to the IEC policy for 10 V/m immunity level

Table 5.2 shows the percentage risk of an EMI event based on the curves of figure 5.5 (a) and 5.5 (b). When no EMI policy is used in the room, the solid curve is used, for both measurements and simulations to compute the probability of exceeding the immunity level. In the case of 3 V/m, according to the measurements, the risk of exceeding the immunity level is 80%; for a device with 10 V/m immunity, the risk of exceeding immunity is 22%. The simulated data indicates that the risk of exceeding the immunity level of 3 V/m is 79.5% and the risk of exceeding an immunity level of 10 V/m is 20.5% when no policy is used. When a free space based minimal separations policy is used for devices with 3 V/m immunity, solid line with circles, the risk of exceeding 3 V/m is 69% for the measurements and 51.4 % for the simulations. The risk of exceeding the immunity when free space based minimal separations for 10 V/m immunity, solid line with triangles, is 3.9% for measurements

and 4.2% for simulations. The IEC based EMC policy for devices with 3 V/m immunity does not allow devices to operate within 5.9 m of the 600 mW source. For the small, 3 m length square, room used in this study, the device is not allowed to operate within the room and therefore the risk is identically zero. When using the IEC based policy for devices with 10 V/m immunity, solid line with triangles, the risk of exceeding immunity is 0.88% for measurements and 6.6% for simulations.

Table 5.2

Risk of EMI incident for clay-block room at 850 MHz. *= Separation puts device outside of room.

Immunity (V/m)	EMC Policy	Separation (m)	Simulated % Risk	Measured % Risk
3	None	0	79.5	80
3	Free Space	2.0	51.4	69
3	IEC	5.9 *	0	0
10	None	0	20.5	22
10	Free Space	0.6	4.2	3.9
10	IEC	1.8	6.6	0.88

The usage of minimal separations based on free space did reduce the risk of EMI within the room. The amount of reduction for devices with 3 V/m immunities was small while the 10 V/m immunity devices had substantial reduction of EMI risk. The proportion of the planar surface that was outside of the minimal separation region was small in the 3 V/m case, the medical device would be allowed to operate in only around 3 % of the surface. The proportion of the surface that was outside of the

minimal separation region for the 10 V/m immunity level was around 88%. The IEC 10 V/m meter standard would have nearly the same minimal separation distances as the free space 3 V/m shown in table 5.2. The risk would be virtually zero and the proportion of the room available for use would be 3%. The IEC 3 V/m minimal separations would preclude medical devices to be in any room that had dimensions less than 6 meters.

5.3 Identification of Distribution of Fields

The distribution of the electric field strength of the interference patterns within the room was compared with Rayleigh cumulative distributions using the procedure described in section 4.6 where the corridor distributions were compared with different distributions.

The graphical comparison in figure 5.6 indicated that a Rayleigh distribution using a parameter of 4.8 was close to the distribution of the simulated room fields. Note that each distribution was formed using 100 bins. The Kolmogorov-Smirnov test was not conclusive for these distributions when the entire room was used. As in the corridor characterization of section 4.6, when the portion of the fields immediately around the source was excluded, the distributions matched with over 96% confidence. The distribution of the interference pattern within the room could be estimated using the above distribution with high confidence except for regions very close to the source.

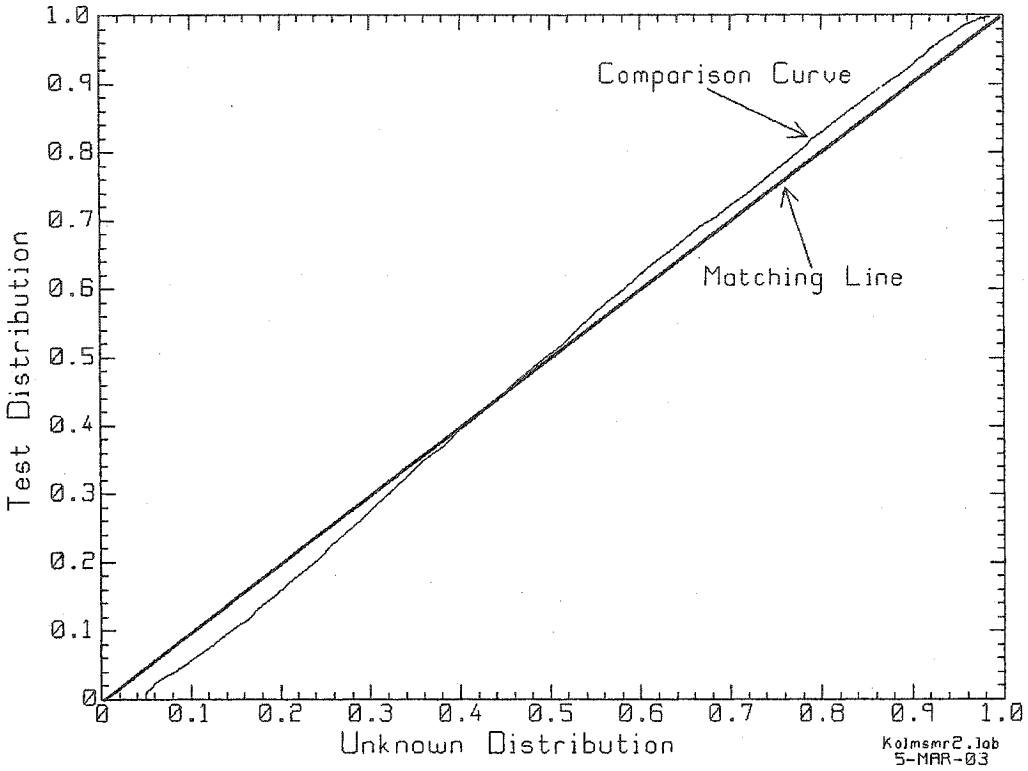

Figure 5.6 Relating field distribution with known distributions. Best match Rayleigh using parameter of 4.8 using 100 bins.

While the differences between the matching line and the comparison curve were small, there was only a small portion of the middle of the matching line where the two lines overlapped. This implied that the Rayleigh distribution was not an ideal distribution to use for this field structure.

5.4 Summary

Electric fields within a small clay-block walled room were produced using a 0.6-watt RF source operating at 850 MHz. The resulting electric field data was sampled using both single trajectory and multiple trajectory measurements.

A parallel series of simulations was performed and the simulation data was validated by the measurements. The single trajectory simulations were very close to the measured trajectories. The simulated multiple trajectories, forming a planar surface in the room, had a similar general structure to the measured fields and were statistically very close to the measured fields. The interference patterns were more prominent for the simulated fields suggesting that the walls used in the simulations were more reflective than the actual walls in the room where the measurements were performed.

Characterizing the field strength using power law models did not provide as useful a tool as for corridors in chapter 3. The small room did not provide sufficient distances for the field strength to attenuate according to the path loss exponent. The measured and simulated trajectories had field strengths that were generally very close despite having different path loss exponents. Regions with strong fields could be located throughout the planar surface investigated. Moving away from the source did not usually reduce the field strength for this environment.

The resulting data sets were used to assess the potential of EMI within the room for medical devices of 3 and 10 V/m immunities. Three EMC policies were investigated: free space based minimal separations, IEC based minimal separations and no minimal separations. If no EMC policy is used, the risk of EMI was 80% for devices with 3 V/m immunity. Using an EMC policy based on minimal separations reduced the risk for devices with 3 V/m immunity as follows: free space minimal separations brought

the risk down to 51.4 and 64 % for the simulated and measured cases respectively. IEC based minimal separations prohibited devices from operating within the room; this effectively reduced the risk of EMI to zero. For devices with 10 V/m immunity, no EMC policy indicated a risk of EMI of 20.5% according to simulations and 22% for measurements. Using free space based minimal separations, the risk was reduced to 4.2% for simulations and 3.9% for measurements. The IEC based minimal separations provided risk levels of 6.6% for simulations and 0.88% for measurements for devices with 10 V/m immunity. These last risk values were interesting as they seemed to conflict with an intuitive feel for the problem when free space type propagation is assumed. Previous work in rooms with reflective walls indicated that a small room would behave as a lossy resonant cavity, [58] and that "corner reflector" type geometry within a room could create high field strength regions at locations far from the source in small rooms [55]. The IEC standard is a more rigorous policy where the distances are typically more than 3 times greater than free space based standards. Why then is the risk greater? There was a region of high field strength furthest from the source and there is a region of low field strength near the middle of the room. Excluding the middle of the room and using only the far corner of the room actually increased the risk by excluding the safe regions in the middle of the room.

The next chapter will discuss an alternate theoretical approach in which the average electric field within a room will be used to characterize the electromagnetic environment with a single number. The average field for measured and simulated room data will be compared with the theoretical value of the average electric field.

Chapter 6

Preliminary Estimation of the Average Electric Field in a Room

In chapter 5, a small room with walls of substantial reflectivity, interference patterns tended to dominate the field structure. Statistical characterization of the fields within such rooms is used in reverberation chambers and resonant cavities. [35, 36, 37] The basic principles that govern these structures were developed using average energy principles as defined by Sabine et al. [69]. In this chapter this characterization will be extended to rooms with non-metallic walls that are substantial but not perfect reflectors. This chapter will introduce an expression for the average field strength within a small room with reflective walls based on a series of assumptions similar to those used in acoustics for reverberation time in live rooms [49].

6.1 Description of the Environment

A small rectangular room is assumed to have walls that absorb a fraction of the energy incident on them and reflect the remaining energy back into the room. A source with power P_O is placed in the room. If there are no absorbers in the room, power loss must be due to transmission through the walls. The time average electrical stored energy density in a plane wave with electric field strength E (V/m), ψ, is assumed to be constant and is given by the following relationship:

$$\psi = \frac{1}{2}\varepsilon E^2 \ (\mathrm{J/m^3}) \qquad \ldots(6\text{-}1)$$

where ε is the permitivity of free space and E is the electric field strength.

A small portion of a wall ΔS is surrounded by a hemispherical "Huygen's Source", [4, 5] of thickness "*dr*" shown in figure 6.1, which is an equivalent source of the field incident on ΔS. An elemental portion of the equivalent source dV, assumed to be isotropic, radiates energy in all directions as

$$\frac{\psi dV}{4\pi r^2} \ (\mathrm{J/m^2}) \qquad \ldots(6\text{-}2)$$

where r is the distance from dV to the elemental wall surface in figure 6.1.

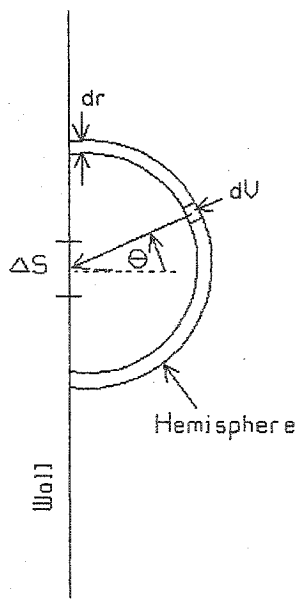

Figure 6.1 Schematic of equivalent source for small portion of wall ΔS.

The energy incident on ΔS is the normal component of the radiated energy obtained using the projection onto the surface area. The projection is

$$\Delta S \cos\theta$$

...(6-3)

where θ is the angle formed by the incident ray and the surface normal in figure 6.1. The energy incident on ΔS, dW, using the projection relationship in (6-3) is

$$dW = \frac{\psi dV}{4\pi r^2} \Delta S \cos\theta \ \text{(J)}$$

...(6-4)

This is the contribution of an elemental portion of the hemisphere; the total contribution of the entire hemisphere is obtained by integration over the surface. The differential volume of a hemisphere element is given by

$$dV = dr\left(r\sin\theta d\phi\right)\left(rd\theta\right)$$

...(6-5)

where ϕ is the angle following the perimeter of the projection of hemisphere onto the wall surface. The contribution of the elemental volume dV can be written as

$$dW = \frac{\psi \Delta S}{4\pi r^2} \cos\theta \left(r^2 dr\right)\left(\sin\theta d\theta\right) d\phi \ \text{(J)} \qquad \ldots(6\text{-}6)$$

Now that the elemental volume contribution is known, the contribution of the entire hemisphere can be computed. The entire hemisphere of thickness *dr* is computed using

$$dW = \int_{\theta=0}^{\frac{\pi}{2}} \int_{\phi=0}^{2\pi} \frac{\psi \Delta S}{4\pi} dr \cos(\theta)\sin(\theta) d\phi d\theta \ \text{(J)} \qquad \ldots(6\text{-}7)$$

after integration this becomes

$$dW = \frac{\psi \Delta S}{4} dr \ \text{(J)} \qquad \ldots(6\text{-}8)$$

In order to relate energy with power, a time dependence must be introduced, knowing that the propagation of electromagnetic waves is of a fixed velocity, *v*, for a given medium, the time that the wave, or energy, takes to travel through a distance *dr* is

$$dr = vdt \ \text{(m)} \qquad \ldots(6\text{-}9)$$

In an air filled room, the velocity v is treated as the speed of light $v \cong c \cong 3.0 \cdot 10^8$ m/s

Equation 6-8 may now be re-written as

$$dW = \frac{\psi \Delta S}{4} c dt \qquad \ldots(6\text{-}10)$$

which can be written as

$$P_{\Delta S} = \frac{dW}{dt} = \frac{\psi \Delta S}{4} c \text{ (W)} \qquad \ldots(6\text{-}11)$$

where the power arriving on the elemental wall surface ΔS is $P_{\Delta S}$. At steady state, the total power absorbed by the walls is equal to the total power radiated by the source, assuming that there are no absorbers within the room. The total power absorbed by the walls is the product of the power per unit area with the area of the walls and the average absorption coefficient. The power per unit area, p_a is obtained from equation 6-11 and is

$$p_a = \frac{dW/dt}{\Delta S} \text{ (W/m}^2\text{)} \qquad \ldots(6\text{-}12)$$

The total absorption of the room, A_T, is the product of the area of the walls, S, and the average absorption coefficient, $\tilde{\alpha}_i$, The absorption coefficient of a wall panel α is in general dependent on the angle of incidence. The average absorption coefficient $\tilde{\alpha}$ is

the absorption coefficient averaged over all incident angles. The total absorption of the room is computed using

$$A_T = \sum_{i=1}^{N} S_i \tilde{\alpha}_i \ (\mathrm{m}^2) \qquad \ldots(6\text{-}13)$$

where N is the number of wall panels. The area of wall panel "i" is S_i m^2. Each panel represents a portion of the wall surface with particular electrical properties. For example, a uniform wall would be one panel with a given absorption coefficient. If there were a window in the wall, the surface would have two panels, one for the window and the other for the rest of the wall. The average absorption coefficient is given by:

$$\tilde{\alpha}_i^{\,2} = 1 - \left|\tilde{\Gamma}^2{}_i\right| \qquad \ldots(6\text{-}14)$$

where $\tilde{\Gamma}_i$ is the average value of the reflection coefficient taken overall all incidence angles. If the walls were totally transparent, then $\tilde{\alpha} = 1$ and the total absorption is equal to the total surface area of the walls. If the walls were perfectly reflecting then $\tilde{\alpha} = 0$ and the total absorption is equal to zero. The total power absorbed by the walls in the room, which is equal to the power of the source, can be written using equation 6-12 as

$$P_o = p_a A_T = \frac{dW/dt}{\Delta S} A_T \text{ (W)} \qquad \ldots(6\text{-}15)$$

Using 6-11, this relationship can be re-written as

$$P_o = \frac{\psi c}{4} A_T \text{ (W)} \qquad \ldots(6\text{-}16)$$

The energy density per unit volume can now be related to the power of the source as follows

$$\psi = \frac{4P_o}{A_T c} \text{ (J/m}^3\text{)} \qquad \ldots(6\text{-}17)$$

The electric field is related to the energy density from equation 6-1, allowing equation 6-17 to be written as

$$\frac{\varepsilon \tilde{E}^2}{2} = \frac{4P_o}{A_T c} \text{ (J/m}^3\text{)} \qquad \ldots(6\text{-}18)$$

To solve for the relationship in terms of the average electric field strength, the above relationship is rewritten as

$$\tilde{E} = \sqrt{\frac{8\eta P_o}{A_T}} \text{ (V/m)} \qquad \ldots(6\text{-}19)$$

where η is the intrinsic wave impedance of space (377 ohms) which is close to the value of the intrinsic wave impedance of air.

The relationships developed above are founded on several assumptions: that the energy density is uniformly distributed throughout the room; the walls are quite reflective and that there are no absorbers in the room and that the source is an isotropic radiator.

When relating the expression in 6-19 to power density of plane waves $\overline{S}_{av}$, given by

$$\overline{S}_{av} = \frac{1}{2}\text{Re}\left(\hat{E} \times \hat{H}^*\right) = \frac{\left|\hat{E}\right|^2}{2\eta} \qquad \ldots(6\text{-}20)$$

when computing the energy (W) which is the product of power density, room surface area (S) and time (dt) equations 6-9 and 6-20 are used to get

$$W = \frac{\left|\hat{E}\right|^2}{2\eta} S dt = \frac{\left|\hat{E}\right|^2}{2\eta} S \frac{dr}{c} \text{ (J)} \qquad \ldots(6\text{-}21)$$

The energy density is the ratio of total energy to volume that is written as

$$\Psi = \frac{\frac{E^2}{2\eta}\frac{dr}{c}_S}{drS} \quad (\mathrm{J/m^3}) \qquad \ldots (6\text{-}22)$$

which, when simplified becomes

$$\Psi = \frac{E^2}{2\eta c} = \frac{E^2 \varepsilon}{2} \quad (\mathrm{J/m^3}) \qquad \ldots (6\text{-}23)$$

the same result as in equation 6-1. This indicates that equation 6-1 describes the energy density for a room taking into account both the electric and magnetic field contributions when the fields behave like plane waves.

6.1.2 Average Reflection Coefficient

In equation 6-14, $\tilde{\Gamma}_i$, is the wall reflection coefficient averaged over all incidence angles given by

$$\tilde{\Gamma}_i = \int_{\theta=0}^{\pi/2} \Gamma_i(\theta) f(\theta) d\theta \qquad \ldots (6\text{-}24)$$

where θ is the angle of incidence, $\Gamma_i(\theta)$ is the angle-dependent reflection coefficient and $f(\theta)$ is the probability density function giving the likelihood that a ray will strike a wall at a particular incidence angle θ.

Additional assumptions are used to estimate the average value of the reflection coefficient. Since multiple reflections are assumed, the average of the parallel and perpendicular polarization reflection coefficients is used. This decision will be valid when there is no predominant polarization after multiple reflections. The probability density function is not generally known a priori so a uniform distribution was assumed for a first trial. The walls were assumed to be of uniform construction. The layered reflection coefficient used by the GO_3D code was taken to be a good estimate of the reflection coefficient of a particular wall construction.

The Sabine Theory, adapted above to electromagnetic fields in rooms, is more likely to be effective in "live" rooms where the walls have high reflection coefficient values. The estimate of the average electric field computed using the above relationships is more useful when the walls, floor and ceiling have high reflection coefficients.

The following section investigates the minimum value of the average reflection coefficient.

6.1.3 Average Electric Field Strength

Suppose that a 600 mW isotropic source radiates in a room of total wall surface area 46.8 m^2, where all of the wall surfaces have the same average reflection coefficient. If the reflection coefficient were zero, then the source radiates as if it were in free space. In this case A_T=46.8 m^2 and the average electric field strength is 6.28 V/m. As the reflection coefficient of the walls rises, the average absorption, equation 6-14, falls and 6-13 shows that A_T declines in value. Then 6-19 shows that the value of the average electric field in the room rises as expected. Figure 6.2 shows the value of average field strength as a function of the average wall reflection coefficient. For $\tilde{\Gamma} \geq 0.553$ the field strength is 20% or more, larger than the case with transparent walls. Figure 6.2 shows that for reflection coefficients larger than roughly 0.8 the average field strength in the room rises sharply with increasing reflection coefficients. The figure suggests that although the Sabine method of equation 6-19 might be used for "small" reflection coefficients such as 0.55, it is a better estimator when walls with "larger" reflection coefficients, say 0.8 are used.

From figure 6.2, the average field strength for a room with transparent walls is 6.22 V/m. The average field strength increases within the room as the average reflectivity of the walls increases reaching a vertical asymptote at total reflection where the average reflection coefficient has unity magnitude. The increase in average field strength occurs at higher rates after $\tilde{\Gamma} \geq 0.553$, where the average field strength is 20% above free space level when the average reflection coefficient is 0.553, 65%

above free space level when the average reflection coefficient is 0.8 and 127% above the free space level when the average reflection coefficient is 0.9.

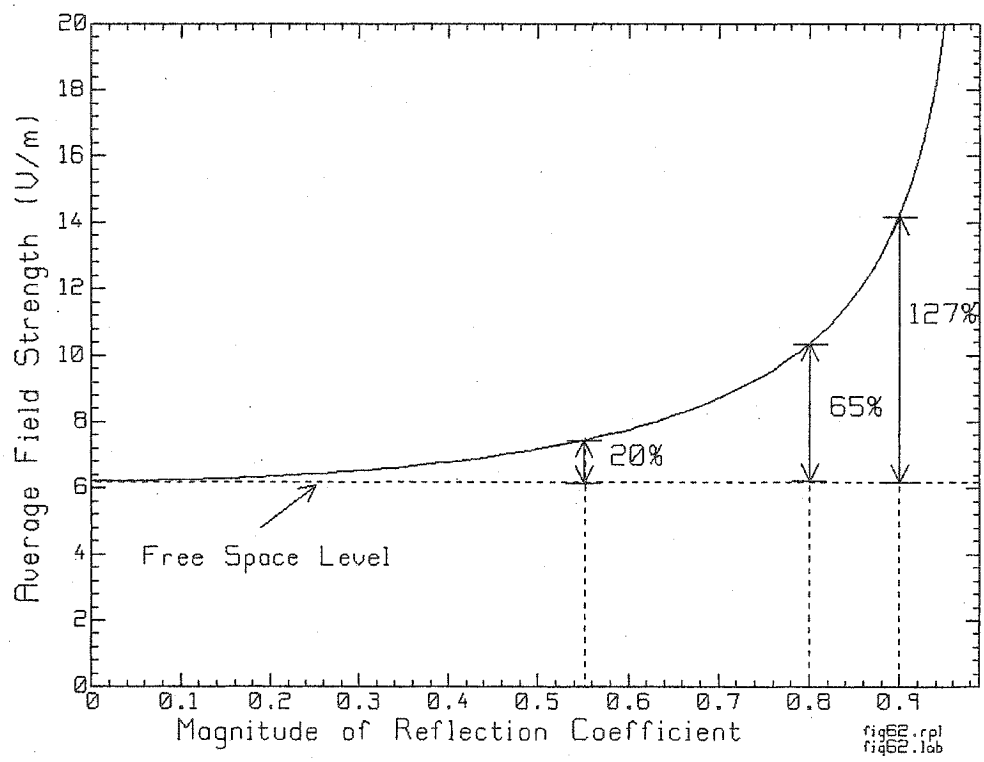

Figure 6.2 Average electric field strength for a rectangular room with 46.8 m^2 interior surface area with a 600 mW source operating within the room.

The higher average fields are due to the reflection of fields back into the room, these reflections also produce interference patterns such as those found in section 5.1 and section 5.2. The higher average field strength coupled with the interference patterns produce electromagnetic environments where minimal separation based EMC policies are not as effective. The average field strength may be used to identify whether a susceptible device may be operated in a particular room. Minimal separation-based

EMC policies are less effective in rooms with an average reflectivity above the threshold level.

6.2 Average Field in Small Clay-Block Room

The small clay-block walled room of Chapter 5 will be used as an example in the average field computation in this section. The absorption of the walls, floor and ceiling of the room must be estimated. The average reflection coefficients for the different materials within the room were computed using equation 6-20 for both polarizations using the GO_3D program discussed in section 2.4. The resulting average reflection coefficients assuming all possible incident angles are shown in table 6.1. This is considered valid when the source is located near a corner of the room as in figure 2.10. The probability density function for the incident angles is assumed to be uniform for this initial investigation. The four materials used in the construction of the room are clay-block, wood, metal and concrete. Two of the side walls are of clay-block construction, the other two side walls are of composite construction, one has a window with a metallic screen and radiator, the other has a doorway and door. The door has a mirror that covers over 70% of the door surface area on one side. The ceiling is made of reinforced concrete.

The clay-block material reflects about half of the parallel-polarized electric fields and over eighty percent of the perpendicular-polarized fields. The concrete material reflects only a third of the parallel-polarized fields and sixty percent of the

perpendicular-polarized fields. The metal acts as a perfect reflector for both polarizations and the 4.5 cm thick wood has nearly the same reflective properties as the 30 cm thick concrete at 850 MHz, namely approximately a third of the parallel- and sixty percent of the perpendicular-polarized fields are reflected.

Table 6.1

Average of the square of the reflection coefficients for different wall materials and different polarizations at 850 MHz assuming uniform probability distribution of incident angles. The average value of the reflection coefficient is computed using both polarizations.

Material	Polarization	$\lvert\tilde{\Gamma}^2\rvert$	Average
Clay (14 cm)	Parallel	0.3302	
Clay (14 cm)	Perpendicular	0.6946	0.5124
Concrete (30 cm)	Parallel	0.1434	
Concrete (30 cm)	Perpendicular	0.3935	0.2685
Metal (0.1 cm)	Parallel	1	
Metal (0.1 cm)	Perpendicular	1	1
Wood (4.5 cm)	Parallel	0.1908	
Wood (4.5 cm)	Perpendicular	0.4286	0.3097

The internal composition of the walls is not fully known, as there is internal piping and ducting along with support studs that are within the walls and pierce the floor and ceilings. In addition, the walls and floors are of reinforced concrete. The reinforcing

structures are made of metal and usually consist of a metallic grid and reinforcing bars of metal. The exact proportion of the walls, floor and ceilings that contain metallic structures is unknown in this situation. In an attempt to characterize the room's absorptive properties, different proportions of the materials in table 6.1 are used in the computation of the total absorption of the room.

Four cases are used in to compute the average electric field strength in the small clay-block walled room. Case 1, all four of the side walls are composed of clay blocks. The window, radiator and doorway are not included. The ceiling and floor are composed of concrete with no metallic elements. Case 2, the window with metallic screen, radiator and open doorway are included in the model. Case 3, the window with metallic screen, radiator and closed doorway with mirror on door are included. Case 4, all of the items in case 3 are used and 5% of the ceiling and floor surfaces are metal. The 5% metal is used to approximate the metallic structures present in reinforced concrete. The proportion of surface area for each of the materials in the four cases is shown in table 6.2.

The wooden door is nearly completely covered by the mirror and the remaining surface area has, at this frequency and distribution of angles, very nearly the same average reflectivity as concrete. The portion of the door not covered by the mirror was treated as wood for surface area. The total surface area of the room is 46.8 m^2 for all of the cases. The surface area composed of clay blocks is reduced from 28.8 m^2 in case 1 to 22.8 m^2 in the other cases due to the inclusion of the window, radiator and

door. The only transparent, air, section of the wall is when the doorway is kept open in case 2. Since the measurements were taken with a closed door, this case does not reproduce the actual experimental set-up. Case 3 has the door closed and the mirror introduces more metallic reflecting surface into the model. The amount of metallic surface area goes from 3.6 m^2 in case to 6.0 m^2 in case 3.

The last case introduces more metallic surface, 9.6 m^2, in an attempt to account for the reinforcing metal within the floor and ceiling. The actual electric properties of imbedded metallic structures within concrete are more complicated than the approximation made here [40], but this crude approximation was used as an initial approximation of the electrical properties of such structures. The presence of wiring and piping inside the walls, floor and ceiling is not accounted for in these cases and would require a more detailed model to be constructed in order to properly characterize the metallic conduits.

Table 6.2

Surface area composed of each material in small clay-block walled room used to compute the total absorption of the room. Details of each case are described in text

Material	Case 1	Case 2	Case 3	Case 4
Clay Block	28.8 m^2	22.8 m^2	22.8 m^2	22.8 m^2
Metal	-	3.6 m^2	6.0 m^2	9.6 m^2
Air	-	2.4 m^2	-	-
Concrete	18 m^2	18 m^2	18 m^2	14.4 m^2

The changes in the proportion of each material will change the total absorption of the room. The total absorption of the room and the average electric field for a 600 mW isotropic source for each case is shown in table 6.3.

Table 6.3

Average of the square of the reflection coefficients for entire room, total absorption and average electric field for room using 4 cases discussed above and measured and simulated field values.

Case	$\lvert\tilde{\Gamma}^2\rvert$	A_T (m^2)	Average Field (V/m)	Median Field (V/m)
1	0.651	35.51	7.14	-
2	0.693	33.72	7.33	-
3	0.743	31.16	7.60	-
4	0.797	28.24	8.01	-
Measured	0.828	26.26	8.30	5.81
Simulated	0.818	26.91	8.20	6.07

Case 1 has the lowest average field strength of 7.14 V/m and the highest total absorption of 35.51. Case 2, has a total absorption of 33.72 and the average field strength of 7.33 V/m, slightly higher field strength than in the first case. This is interesting since in the first case the room has no apertures and intuition would suggest that the average field strength is higher in volumes within closed surfaces rather than volumes within surfaces with apertures. It is most likely that the metallic

surfaces, perfect reflectors in this model, offset the lost power through the aperture. The closing of the reflective door, case 3, increases the average field strength to 7.60 V/m and decreases the absorption to 31.32. The addition of metallic panels corresponding to 5% of the floor and ceiling surface area, resulting in a total absorption of 28.24, the lowest of the four cases. With lower total absorption, the average field strength is proportionally higher at 8.01 V/m. Case 4 models the electrical properties of walls with imbedded metallic structures in an unrealistic way, but provides an illustrative example of how different electrical properties may be modeled using this method.

The average electric field strength from the measurements and simulations, 8.3 and 8.2 V/m respectively, are no more than 10% higher than the average field strengths computed using this process but the median values of the measured (5.81 V/m) and of the simulated (6.07 V/m) fields are about 12% lower than the estimates using the most realistic model (case 3).

The very high field strengths immediately around the source would account for such differences between the mean and median values. The median discounts "outliers", data that appears to be atypical within the data set. Fields immediately around the source are much higher than fields in the rest of the room and increase the mean value of the field strength within the room. The median value reduces the effect of the contributions of fields immediately around the source but the average field is a more conservative estimator of EMI risk in small rooms since the atypical field strength

values are often high field strength values. In larger rooms, these atypical values would play a less significant role in the risk of EMI and the median values should be used.

6.2.1 EMC Implications of Higher Average Field Strength.

Table 6.3 shows that the average reflection coefficients of case 3 and case 4 are in the region in figure 6.2 where the Sabine theory is expected to be useful. High average wall reflection leads to high average field strengths in table 6.3. For these cases the EMC policy based on minimal separations should not be used. The difference between the estimate of the average field strength and the average of the measured fields varies from 17%, using case 1, to 6% using case 4. The difference between the estimate of the average field strength and the average using simulations with GO_3D varies from 16%, using case 1, to 5% using case 4. The average field strength in the room for both the simulations and the measurements are higher than the average field strength in case 4, suggesting that the estimates of the reflectivity of the room are lower than the actual reflectivity of the walls, floor and ceiling. In this situation, minimal separations are even less acceptable for use in this environment.

Equation 6-19 can be used with the measurement or simulation field strengths to estimate the equivalent average reflectivity of the walls. Table 6-3 shows $\widetilde{E} = 8.3$ for measurements and 8.2 (V/m) for simulations. By solving 6-19 for the total absorption, $A_T = 26.26$ m^2 for measurements and 26.91 m^2 for simulations. With a value for the

total absorption, the average reflectivity may be estimated using equation 6-13 and by assuming all of the walls have the same reflectivity value. This assumption simplifies the relationship by making the total absorption the product of the total surface area of the room, 46.8 m^2, and the average absorption of the surfaces, $\tilde{\alpha}$=0.561 for measurements and $\tilde{\alpha}$=0.575 for simulations. The average reflectivity of the walls may be estimated using equation 6-14 to obtain $\tilde{\Gamma}$= 0.828 for measurements and $\tilde{\Gamma}$=0.818 for simulations. The average reflectivity for both the measurements and simulations are within the range (greater than $\tilde{\Gamma}$=0.55) in figure 6.2 where the Sabine theory is expected to be reasonable accurate. For such rooms the "minimal separations" EMC policy should not be used.

6.3 Summary

This chapter discussed an alternate approach to characterizing room electromagnetic fields by reducing the complex field patterns into a single number, the average electric field. Making multiple assumptions such as, uniform distribution of energy in the room, isotropic source and uniform distribution of incidence angles on all surfaces, allowed for the development of a closed form expression for the average electric field. This closed form expression works best with rooms with walls of substantial reflectivity. This closed form expression was used to compute the average electric field using reflectivity values obtained using a GO-based code.

The average field values for different room constructions were tabulated and compared with the average field values obtained from measurements and simulations. The best matches, within 6% of the values, came from models where most detail of the room structure was included. However, even a relatively primitive model provided an estimate of the field within 17% of the actual measurement and simulation values. The actual average field strength was larger than values obtained using the reflection coefficient data from the GO_3D code. This suggests that the actual average reflection coefficient was larger than the one used. A simplified model of the internal metallic structures such as metallic conduits and reinforcing material was used in one case, despite known inaccuracies, in order to illustrate the process of modeling such structures using metal panels. Observations made in chapter 5 showed that higher reflectivity walls produced interference patterns in small rooms. These interference patterns had high field strength locations that were distributed throughout the room. In this chapter, high average field strength was associated with a range of average reflectivity values. EMC policies based on minimal separations may not be effective in reducing EMI risk in rooms with very high average reflectivity.

The average electric field provides a single value to characterize the complex fields found within a room with reflective walls. This approach is an alternative characterization to the power law + residual models of chapters 3 and 5 and the distribution models of chapters 4 and 5. This form of characterization does provide an initial quick estimate of the field strength prior to investing larger amounts of time in extensive measurement and simulation studies.

Chapter 7

Discussion and Conclusions

This thesis presented a quantitative measure of EMI risk for medical institutions due to mobile wireless sources. The first step in developing this quantitative measure of EMI risk was the extensive measurement and simulation of the electromagnetic fields due to a wireless source in a typical urban hospital. This approach combined the advantages of measurement and simulation. Measurement offers the ability to discover behavior not previously known, and provides validation data for theory. Simulation allows the rapid production of data and the versatility to test different situations. The next step was the characterization of the measured and simulated electric field strength. One approach fitted a power law model to the field strength and used a cumulative distribution of the residuals to characterize the EMI risk. Another approach used the cumulative distribution of the field directly to characterize electric field strength. The EMI risk was defined as the probability of exceeding the immunity level of a given device. Both the cumulative distributions of the residuals and the cumulative distributions of field strength were used to obtain a quantitative measure of EMI risk. The development of the two methods, power law with residuals and cumulative distribution of field strength, of quantifying EMI risk within hospital corridors and rooms form the principal contribution of this thesis, and the average field concept provides a novel approach to the quick characterization of a room.

7.1 Field Strength Measurements

This thesis presented measurements of electric field strengths of a wireless source in a hospital corridor or room at 850 and 1900 MHz. This is the first time such extensive

field strength measurements have been reported in an urban hospital. The vertical component of the electric field strength was measured using a robotic system that allowed for fine spacing between measurement points along a long straight-line trajectory in a 50-meter corridor. Measuring many parallel trajectories at various heights and distances from the wall provided an exploration of the distribution of the field over the volume of the corridor shown in figure 3.5, for the first time at 1900 MHz. (pg. 84) Also this thesis presents for the first time extensive measurements of the field strength on a planar surface above the floor of a typical hospital room, figure 2.15 (pg. 39).

These measurements show that in general, the field strength near the source decreased with distance at a higher rate than field strength at locations further than a meter from the source. Very near the source the field associated with the direct ray is dominant and much larger than the fields caused by the reflected rays from the walls, floor and ceiling. Further than one meter, the net contribution of reflected rays are commensurate with the field strength of the direct ray. Field strengths at 1900 MHz generally tended to be lower near the side walls than near the mid-line of the corridor, as shown in figure 3.5 (a) and 3.5 (b). An exception were the low-strength, nearly constant, vertically polarized fields at 1900 MHz that were measured 30 cm above the floor in the corridor, shown in figure 3.5 (c). These field strengths exhibit a much slower rate of decrease in field strength with distance than the measurements taken higher levels above the floor, shown in figure 3.11 (pg. 93). This previously-unreported behavior occurred when both the source and receive antennas were vertically polarized. When the receive antenna was horizontally polarized, the measured field strength near the floor behaved in a manner similar to the measurements taken at the other heights, as shown in figure 3.6 (pg. 85).

The measurements taken in a typical the hospital room, with the source near one corner, showed a strong interference pattern, with high field strengths located near all four corners of the room. Trajectory measurements in the room, figure 2.17 (pg. 42), indicated that the initially-high field strength dropped rapidly when moving away from the source, but further than 60 cm or so away the field strength dropped much less rapidly. The field strengths along the paths were mostly above 3 V/m and below 10 V/m, except immediately adjacent to the source, where field strengths were over 10 V/m. The planar surface measurements in the room, figure 2.15 (pg. 39), showed that the structure of the fields in the room was dominated by interference patterns, with most of the highest field strengths concentrated near the source. The remaining high field regions were distributed throughout the planar surface, even at locations furthest from the source including the four corners.

7.2 Field Strength Simulations

The simulations presented in chapters 4 and 5 were based on Geometrical Optics (GO). The simulations showed, figure 3.19 (a)-(c) (pg. 108), that the field strength decreased at higher rates for distances within 1 meter from the source and decreased more slowly when further than 1 meter. This behavior was almost identical to that seen in the measurements. The simulations at 1900 MHz also showed that the rate of attenuation of the field strength was greatest near the corridor centerline and lowest near the side walls, figure 3.23 (pg. 115). Simulations performed on a planar surface above the floor at 850 (analog cell phone), 1900 (digital phone) and 2400 MHz (wireless computer networking), figure 4.4 (a)-(c)(pg. 128), explored the distribution of fields within the corridor with the source fixed at 1.2 meters from the end wall. The fields at 850 and 1900 MHz had relatively high values, above 6 dB V/m, for the first 10 meters of the corridor, and smaller values further away. Fields tended to be lower

near the side walls and higher near the centerline. At 2400 MHz the higher fields extended to the first 20 meters of the corridor. There were generally higher field strengths at 2400 MHz than at 850 and 1900 MHz. Weaker fields were found near the side walls as at 850 and 1900 MHz. The interference patterns at 2400 MHz were more structured that at 850 and 1900 MHz, but the general behavior of the fields at 2400 MHz was close to the 850 and 1900 MHz with the exception that regions of high field strength, over 3 V/m, were a bit more extensive than at 850 and 1900 MHz.

The effect of changing the location of the source relative to the end wall of the corridor was investigated using simulations, figure 4.12 (pg. 145). The source location relative to the end wall was chosen so a to produce either a minimum or a maximum along the corridor centerline. The reference location used in the previous simulations was plotted for comparison. While there is little difference between the fields for the minimum and the reference distance, the maximum produced higher fields along the corridor centerline that extended almost 30 meters along the corridor. As in the previous planar surface simulations, higher field strengths were found near the corridor centerline and weaker fields were most often found near the side walls. Further studies should be conducted in order to produce cumulative field strength distributions as a function of relative source distance from the end wall, and frequency of the source within the corridor.

The relative ease with which the simulations were able to compute the field strength on planar surfaces allowed for planar surface surveys of field strength at fixed heights to be calculated. This data, plotted in contour plot format in figure 2.24 (pg. 54), showed the behavior of the field strength with more detail than when using trajectory-based measurements or simulations. The simulations at 1900 MHz generally showed good correspondence with the measurements with the exception of the low constant

field strengths 30 cm above the corridor floor. This suggests that in addition to Geometrical Optics, another propagation mechanism would be necessary to reproduce this behavior; one suggested mechanism is surface wave propagation.

Simulations were performed at 850 MHz with a crude model of the hospital room in which the measurements were taken, figure 2.15 (pg. 39). The simulations showed a strong interference pattern that displayed radial orientation when near the source and aligned with the walls when further than 1 meter from the source. While most of the highest fields were concentrated near the source, the remaining high fields were distributed throughout the planar surface, even in the corners of the room. Despite the lack of detail in the simulation model, which did not include the window and doorway, there was good correspondence between the measurements and simulations. The simulations displayed more prominent interference patterns aligned with the walls than the measurements. This suggests that the walls of the simulation were more reflective than the actual walls. The presence of higher field strengths near all four corners of the room, even the corner furthest from the source, were even more noticeable in the simulations than in the measurements.

7.3 Characterization of Fields

This section summarizes the work presented in this thesis to characterize the behavior of the fields.

7.3.1 Corridor Characterization

The field strengths along trajectories in the 50-meter corridor displayed both slow and fast fading behavior that was characterized in the following manner. A power law

model was fitted to the data using least mean squares regression to characterize the slow fading as in figure 2.26 (pg. 62). The residual is defined as the difference between the actual field strength and that predicted by the power law model shown in figure 2.27 (pg. 64). The cumulative distribution of the residuals, shown in figure 2.28 (pg. 66), was used to characterize the fast fading behavior.

The parameter that described the rate of decrease of field strength as a function of distance between the receiver and source is the path loss exponent n using equation 2-5. The value of n was found for the trajectories at various heights above the floor and distances from the wall, figure 3.23 (pg. 115). This parameter indicated that the rate at which the field strength decreased was higher near the side walls, varying from n = 0.7 to 0.99, and lower near the centerline of the corridor, varying from n = 0.6 to 0.7. The rate at which the field strength decreases is almost always less than the free space rate of n = 1. However at 30 cm above the floor, the path loss exponent indicated that the measured field strength did not decrease very much with distance, n = 0.01 to 0.2, with almost no decrease, n = 0.01, when near the corridor centerline.

The cumulative distribution of the residuals, figures 3.8 (pg. 90) and 3.21 (pg. 111) for measurements and simulations respectively, estimated the probability of the residual exceeding a particular value. The measured and simulated volume residuals tended to have the same general shape with the exception of the measured trajectories taken at 30 cm above the floor. While most distributions had a zero mean and are "S" shaped, the trajectories at 30 cm above the floor had a zero mean and what appears to be a ramp shaped cumulative distribution, which is characteristic of a uniform probability density function. The spacing between points in the corridor volume measurements was larger than the spacing between simulation points. This caused the higher variability in the distributions of the measured residuals, as shown in figure 3.7

(pg. 88), than the simulated residuals, shown in figure 3.21 (pg.111). This can account for some of the difference between the measured and simulated residual distributions but is less likely to account for the differences in the distribution of the residuals at 30 cm height. The differences in both the path loss exponents and the distributions of the residuals again argue that the behavior of the fields near the floor is different from that at other locations in the corridor.

The second method used to characterize the fields was the cumulative distribution of the field strengths themselves, figure 4.5 (pg. 130), rather than the residuals. Simulations were used to calculate the field strength on a planar surface in the 50 m corridor. The planar surface field strength was quantized by subdividing the planar surface into a grid of squares, in this case 3.2 cm length squares, and using the field strength at the center of each square as the field strength for the entire square, as shown in figure 2.13 (pg. 38). The distribution of the field strengths was based on the fraction of the total surface area that contained a particular range of values.

The cumulative distributions for the corridor simulations at 850, 1900 and 2400 MHz, figure 4.5, indicated that for 850 and 1900 MHz the proportion different field strengths are almost identical but at 2400 MHz, there was a larger area of the planar surface with field strengths from 0.5 to 2.3 V/m than in the 850 and 1900 MHz cases. The area having field strengths from 3 to 10 V/m was very close for all three frequencies. These intermediate fields are often associated with good communication links; communication requires sufficient field strength for wireless devices operating within the corridor. These intermediate field strengths are below the immunity level of most medical devices and are not usually considered to constitute an EMI risk.

When the source location relative to the end wall of the corridor was changed in order to produce low or high field strengths along the corridor centerline, a similar pattern emerged. In one location for the source, 7.52 wavelengths away from the end wall, the field strength along the corridor was low. A second location, 7.76 wavelengths from the end wall, was chosen to produce maximum field strength along the centerline of the corridor that increased the proportion of the total planar surface area with intermediate field strengths. A third location 7.60 wavelengths from the end wall was also used. The distribution of the field strengths for the 7.56 and 7.6 wavelength distances the distributions were very close. Of all three cases, the total area with higher field strengths (3 V/m or greater) was slightly higher for 7.76 wavelength spacing

7.3.2 Room Characterization

Room fields at 850 MHz were also characterized using both trajectory data and planar surface data. The trajectory data, figure 5.2 (pg. 158), was less satisfactory in the room due to the strong interference patterns and small distances, which made the power law models poor estimators of the field strength. The field strength within the room only showed large decrease in field strength with separation from the source at locations within 70 cm of the source. Further than 70 cm form the source, the field strength tended to decrease at a much lower rate.

The cumulative distributions of the measured and simulated fields in the room at 850 MHz, figure 5.1, were very close. The agreement is interesting since the simulation model omitted the window and doorway of the room, indicating that even the crude model may provide a useful estimate of the distribution of field strengths on the planar surface. The distributions show that only around 20% of the planar surface has field strength below 3 V/m and 78% of the surface below 10 V/m. The behavior of

the field was counter intuitive since locations further from the source did not necessarily have lower field strengths than regions closer to the source. High field strengths were found in all the corners, just as with the measurements in the room.

7.4 EMI Risk Assessments

EMC policies based on minimal separations are common practices for minimizing EMI incidents. A minimal separation policy determines a minimum safe distance that must be maintained between an RF source of known power and a medical device of known immunity. The distance is typically computed using a power law model, like those given in equation 1-3 and equation 2-8. The present medical device standard IEC 60601-1-2 uses a free space power law model with a correction factor. This correction factor increases the separation to roughly 333% further than the free space power law alone. The "minimal separations" policy assumes that when a device is further than the minimum safe distance, the risk of EMI is zero. Where the risk of EMI is defined as the probability of exceeding the immunity level of the device. This thesis has demonstrated that the risk of EMI when using minimal separations based on free space or the IEC standard is small but often not zero in corridors, tables 4.1 - 4.3, and is the risk is neither small nor zero in the small clay-block room, table 5.2.

Rather than use the pass-fail criterion of minimal separations, this thesis introduced the concept of minimal separations with risk, MSR, for trajectory based data and EMI risk based on cumulative distributions of fields for planar surface data sets.

7.4.1 MSR

This thesis introduced the concept of minimal separations with risk (MSR) as an EMC policy. The MSR distance is computed using a two-segment power law model, equation 2-8, whose parameters are obtained using a least-mean square regression line fit to the measured or simulated field strength. The first segment of the power law model, used for distances within 1 meter of the source, is based on free space propagation. The second segment of the model, used for distances greater than 1 meter from the source, has a path loss exponent obtained from the linear regression fit. The variability of the field, described by the cumulative distribution of the residual dictates the risk of EMI for that particular distance. With this technique the EMC policy maker can select a minimal separation distance based on the allowable risk level, called an MSR distance or "minimal separation with risk distance".

When using the MSR policy with a 5% risk, the suggested separations were less than 5.2 meters, for a 600 mW source radiating full power for most heights. The smallest separations were for devices close to the side walls and the largest separations were for devices close to the corridor centerline. The rate at which the field strength attenuated varied within the corridor volume and as consequence, the MSR distance varied proportionally. Even though the field strengths along paths 30 cm above the floor did not attenuate much with distance from the source, the risk of EMI was mitigated by the low values of field strengths produced by a single 600 mW source and by the fact that most medical devices are not located very close to the floor in a typical hospital setting.

The inclusion of the different rates of field strength decrease and the variability of the field make the MSR an effective tool for quantifying EMI risk due to RF sources

within a hospital corridor. Using this technique, the risk of using a particular wireless system within a hospital can be estimated and used as a design parameter in the same manner as coverage and noise levels in designing the wireless system.

7.4.2 MSR and the Clay Block Room

When considering the use of MSR in the small clay-block walled room, the large interference patterns and the small distances within the room made minimal separations in general and MSR in particular less effective in reducing EMI risk within rooms. The field strength was above 3 V/m for most of the path and went above 10 V/m at a few locations including some locations more than 2 meters from the source. In rooms such as this, further from the source does not necessarily insure weaker field strength. This behavior is not only counter-intuitive but also violates an implied assumption in minimal separations that the fields are weaker as the distance from the source increases. In such environments an alternate risk assessment technique was used.

7.4.2 Distribution of Fields

For planar surfaces, the risk of exceeding the immunity level for a given minimal separation was obtained by computing the distribution of the fields only on the portion of the planar surface that was outside of the minimum safe distance from the source, shown in figures 4.7 (pg. 132) and 5.4 (pg. 165). Unlike the minimal separations with risk, this process gave the risk of exceeding the immunity for an area rather than the risk on a straight line (trajectory). The risk of exceeding immunity was directly obtained using the distribution of the field strengths on planar surfaces.

This technique has the advantage of not requiring that the power law model and residual be computed in order to determine the risk. This process is also better suited than the trajectory-based techniques to surface or volume field distributions, as there is no requirement for the data to be a function of distance from the source. The structure of the field, observed with contour plots such as figures 4.9 (pg. 138) and 5.3 (pg. 162), provided the location of high field strength and the distribution of the fields provided the proportion of the total surface area, or volume, that contained the higher field strengths.

Both the measurements and the simulations demonstrated that the electric field strength within corridors and rooms has a complicated structure. This structure can be better understood using planar surface data sets, simple trajectory data does not provide sufficient information to properly assign EMI risk to such complex environments. While the EMI risk based on the distribution of fields requires larger data sets, planar surface, when compared to MSR, trajectory, data sets, the EMI risk based on the distribution of fields provides more detailed information on where high EMI risk regions are located.

7.5 Average Electric Field

In an attempt to simplify the complex field structure within a room to a single parameter, the concept of average electric field within a room was introduced in chapter 6. The average electric for a chamber with known reflective properties and dimensions was estimated. The estimation was based on several assumptions including a uniform distribution of energy within the chamber and an isotropic source. The higher the actual reflectivity of the walls, the better the agreement between the estimate and the actual average field strength. In addition the higher the

average field within the room, the lower the likelihood minimal separations being effective.

The estimated average electric field was compared to the average of the measured and simulated fields. The more detailed model provided an agreement within 10% with the measured and simulated values. Providing a quick estimate of the "hotness" of the room using source power and average reflectivity of the walls, floor and ceiling of the room.

7.6 Conclusions

After extensive measurements and simulations of the electric field within a typical 50-meter hospital corridor, some characteristics of field strength were observed. Field strength within a corridor decreases with distance from the source at a lower rate near the centerline of the corridor than near the side walls when the source was operating near one of the corridor end walls. At 30 cm above the floor the field strength was low but remained almost constant for the entire length of the corridor. Planar surface simulations within the corridor corroborate the previous results and indicate that field strengths tend to be lower near the side walls of the corridor and higher near the corridor centerline. This behavior might be used for the development of alternate communication channels in addition to EMC policy implications.

This thesis presented two quantitative measures of EMI risk based on both simulations and measurements. By quantifying EMI risk, different EMC policies can be compared and contrasted by level of EMI risk.

The first measure of EMI risk, MSR, provides a technique that allows an institution to define separations according to the maximum allowable risk. Unlike the present standard, which assumes that the risk is zero outside of the minimal separation region, MSR uses an estimate of the risk of exceeding immunity to compute the minimal separation. This novel technique provides a flexible method for computing separations where the risk is zero, based on the variability of the field at that location.

Trajectory-based EMI risk was not effective where the field strength does not decrease with increased separation between the source and receiver, such as in small rooms with reflective walls. This is partially due to the assumption implicit in modeling the field strength with a power law model that the field strength monotonically decreases as the source distance increases, and partially due to the fact that the power law model is less effective in estimating field strength for the short, under 2 meter, distances within the room. The complex interactions of electromagnetic fields within buildings requires more extensive and detailed data sets and models to properly characterize EMI risk.

The second measure of EMI risk used the distribution of fields on planar surfaces in corridors and rooms along with contour maps of field strength on the planar surface. The contour maps of field strength on the planar surface indicated where EMI risk regions, regions with field strength above the immunity level, were located. By not placing the susceptible device in the EMI risk region, the risk of EMI can be even further reduced. While this technique requires larger data sets, planar surfaces, than MSR, trajectory data sets, this technique provides more detailed information on EMI risk and is not dependant on power law models.

Through the use of the techniques introduced in this thesis, it was shown that the risk of EMI may be reduced to nearly zero within hospital corridors by using IEC based minimal separations policy, but the risk of EMI within hospital rooms is not reduced to zero when using the same policy. In addition, the IEC based minimal separations are very restrictive in terms of permitting wireless devices within rooms. If a medical practitioner were unable to enter a patient room with an operating medical informatics link, then the system would have limited usefulness. This thesis has shown that the risk of EMI with a 600 mW wireless source is prohibitively high for small patient rooms. In order to make wireless informatics functional within a hospital setting, low power, (10 mW) sources and high immunity (10 V/m) medical devices should be employed.

These risk estimates were made assuming that the device is radiating the full 600 mW, in most practical cases the source efficiency is less than 60% for a mobile wireless system. When considering the inefficiency of the source, the risk drops accordingly and both the IEC and MSR separations would provide nearly zero risk of EMI. In general EMI risk is higher near corridor centerlines and lower near side walls, conversely communication coverage is better near corridor centerlines and worse near side walls.

The average electric field strength based on the average reflectivity of the room surfaces was computed. This preliminary estimate of the average field strength used several assumptions including uniform distribution of energy and isotropy of the source. The average field strength was used characterize the fields within a room using a single parameter. This parameter is used to classify the room fields as "hot" or "cool". A "hot" room has large average electric field strength and a higher risk of EMI, while a "cool" room has small average field strength and a lower risk of EMI.

The average value of the measured and simulated field strengths were compared with the value obtained using this approximate technique. There was good correspondence, agreement within 10%, between the actual average field and the estimate.

The ability to quantify the risk of EMI using the techniques described in this thesis provided a measure of the effectiveness of an EMC policy and allowed the comparison of different EMI reduction strategies. In addition to EMC policy evaluation, the risk of EMI at different frequencies and source locations relative to the end wall of the corridor was computed. It was shown that the judicious choice of source location and frequency might increase communication coverage within a corridor while only slightly increasing the risk of EMI.

7.6.1 Recommendations and Future Work

This thesis presented results that showed that the usage of models based trajectory-type characterization of fields within corridors and rooms were not always effective at estimating risk of EMI within a hospital. Models based on planar surface and volume measurements should be developed in order to better characterize the distribution of fields. Measurements of all three polarizations of the field within the corridor and room volume would also provide better insight into the three-dimensional behavior of electric fields.

The low field strengths that decreased very slowly with distance might provide a potential communication path for wireless devices. The development of such paths is a topic for future work in this area. If multiple sources were used, the EMI risk at this height would increase proportionally. Further work in measuring and simulating indoor fields caused by multiple sources would provide insight into the effects

multiple sources have on EMI risk. Further work on this topic is required to identify a mechanism that will reproduce such behavior and further increase the accuracy of the GO based simulations.

The simulations were performed using electrical properties obtained from the literature for 850 MHz. Future simulations should use the 1900 MHz and 2400 MHz electrical properties which could further improve the agreement with the measured results.

The large separations associated with the IEC based minimal separations, while insuring low EMI risks, are very restrictive when wireless communication systems are to be placed within a hospital. Work must also be done to develop wireless systems that can overcome the restrictions placed by the medical device standards, including lower power sources, higher immunity medical devices and alternate technologies that are less sensitive to RF EMI such as optical devices. The inclusion of wireless technology into the daily operation of a hospital will require the parallel development of medical practice and wireless technology into an efficient system where quantification of EMI risk can assist the policy makers in developing a safe, efficient wireless hospital.

References

[1] AAMI. Guidance on electromagnetic compatibility of medical devices for clinical/ biomedical engineers, Part 1: Radiated radio-frequency electromagnetic energy. TIR no. 18-1997, AAMI, 1997

[2] ANSI. Recommended practice for an on-site, ad-hoc test method for estimating radiated electromagnetic immunity of medical devices to specific radio-frequency transmitters. ANSI C63.18-1997, New York: ANSI 1997

[3] Barlow H.M., Cullen A.L., "Microwave Measurements", Constable and Co. Publishing 10-12 Orange Street, London England, W.C.2, pp.37-41

[4] Balanis C., "Antenna theory analysis and design", Wiley and Sons Publishing, 1982, ISBN: 0-471-60352-X

[5] Balanis C., "Advanced engineering electromagnetics", Wiley and Sons Publishing, 1989, ISBN: 0-471-62194-3

[6] Banik T., "Spatial fading characteristics of VHF broadcast signals in an urban environment", Master's thesis Department of Electrical Engineering, McGill University, Montreal, Quebec, Canada, March 1988

[7] Beckmann P., "Scattering of electromagnetic waves from rough surfaces", Artech House publishing 1987, ISBN: 0-89006-238-2

[8] Bertoni H., Honcharenko W., Maciel L.R., Xia H.H., "UHF propagation prediction for wireless personal communications", Proceedings of the IEEE, vol. 82, no. 9, pp. 1333-1358, September 1994

[9] Boisvert P. "The ambient electromagnetic environment in metropolitan hospitals", Master's thesis Department of Electrical Engineering, McGill University, Montreal, Quebec, Canada, March 1999

[10] Brennan C., Cullen P.J., "Application of the fast far field approximation of the computation of UHF path loss over irregular terrain", IEEE Transactions on Antennas and Propagation, vol. 46, no. 6, pp.881-889, June 1998

[11] Brown S., Lane M, Fernandez, D., " Integrating Bluetooth in the GSM phone infrastructure", RF embedded technologies, Sept. 2001, pp.22-30

[12] Cappetta L., Feo M., Fiumara V., Pierro V., Pinto I.M., "Electromagnetic chaos in mode-stirred reverberation enclosures", IEEE Transactions on Electromagnetic Compatibility, vol. 40, no. 3, pp. 185-192, Aug. 1998

[13] Chen S.H., Jeng S.K., "SBR image approach for radio wave propagation in tunnels with and without traffic", IEEE Transactions on Vehicular Technology, Vol. 45, pp. 570-578, Aug. 1996

[14] Chen S. H., Jeng S.K., "An SBR-image approach to radio wave propagation in indoor environments with metallic furniture", IEEE Trans. Antennas and Propagation, vol. 45, no. 1, pp. 98-106, Jan. 1997

[15] Cox D.C., Murray R.R., Norris A.W., "800 MHz attenuation measured in and around suburban houses", AT&T Tech. Journal vol. 63, no. 4, pp. 921-954, 1984

[16] Dalke R.A., Holloway C.L., McKenna P., Johansson M., Ali A.S., "Effects of reinforced concrete structures on RF communication", IEEE Transactions on Electromagnetic Compatibility, Vol. 42, No. 4., November 2000

[17] Davis D., Romanski J., Segal B., Lala P., Pavlasek T.J.F., "Separation does not insure electromagnetic compatibility in concrete walled hospital", Proceedings of the Canadian Medical and Biological Engineering Society pp.82-83, Edmonton, Alberta, Canada, June 28-30, 1998

[18] D. Davis, B. Segal, G. Tait, T. Pavlasek, "Evaluation of Free-Space Propagation in Hospital Corridors", Symposium on Antenna Technology and Applied Electromagnetics Conference Proceedings, pp. 25-28, Ottawa, Ontario, Canada, Aug. 1998

[19] Davis D., Segal B., Pavlasek T.J.F., "Can minimal separation criteria ensure electromagnetic compatibility in hospitals? An experimental study", Biomedical Instrumentation and Technology, vol. 33, no. 5, pp. 411-416, Sept. 1999

[20] Davis D., Segal B., Pavlasek T.J.F., "Electromagnetic interference risk: Statistical quantization when using free-space minimal-separations between wireless sources and medical devices", Proceedings of the Canadian Medical and Biological Engineering Society pp.126-127, London, Ontario, Canada, June 24-26, 1999

[21] Davis D., Segal B., Cinquino A., Hoege K., Mastrocola R., Pavlasek T.J.F., "Electromagnetic compatibility in hospital corridors", Proceedings of the IEEE International Symposium on Electromagnetic Compatibility, pp. 268-272, Seattle, Wa., USA, Aug. 3-6, 1999

[22] Davis D., Segal B., Chu D., Trueman C.W.T., Pavlasek T.J.F., "Effect of spatial-sampling resolution on electromagnetic path-loss and interference potential estimates in hospital corridors", Proceedings of the Canadian Medical and Biological Engineering Society, pp. 46-47, Halifax, N.S., Canada, Oct.26-28, 2000

[23] Davis D., Trueman C.W.T., Calzadilla R., Pavlasek T.J.F., "Measurement of indoor 0.85 and 1.9 GHz propagation in hospital corridors", Proceedings of the IEEE Conference on Antennas and Propagation for Wireless Communications, pp. 77-80, Waltham, Mass., USA, Nov.6-8, 2000

[24] Davis D., Segal B., Martucci D., Pavlasek T.J.F., " Volumetric 1.9 GHz fields in a hospital corridor: Electromagnetic compatibility implications", IEEE EMC International Symposium, pp. 1131-1134, Montreal, Quebec, Canada, Aug. 13-17, 2001

[25] Davis D., Segal B., Trueman C.W.T., Pavlasek T.J.F., "Assessment of minimal-separation criteria in a 50-m. corridor", ANTEM 2000 Proceedings of Symposium on Antenna Technology and Applied Electromagnetics, pp. 129-133, Montreal, Quebec, Canada, July 31-Aug. 2, 2000

[26] Degli-Esposti V., Lombardi G., Passerini C., Riva, G., "Wide-band measurement and ray-tracing simulation of the 1900-MHz indoor propagation channel: Comparison

criteria and results", IEEE Transactions on Antennas and Propagation, vol. 49, no. 7, July 2001

[27] Degroot M, "Probability and statistics 2nd edition", Addison-Wesley publishing, pp. 18-19, 1987, ISBN: 0-201-11366-X

[28] Dersch U., Troger J., Zollinger E., "Multiple reflections of radio waves in a corridor", IEEE Transactions on antennas and propagation, vol. 42, no. 9, pp.1571-1574, September 1994

[29] Dersch U., Zollinger E., "Physical characteristics of urban micro-cellular propagation", IEEE Transactions on Antennas and Propagation, vol.42, no. 11, pp. 1528-1539, November 1994

[30] ECRI, "Electromagnetic interference and medical devices, an update on the use of cellular telephones and radio transmitters in healthcare facilities", Guidance Article, Health Devices, vol.25, no.2-3, pp. 101-106, Feb.-Mar. 1996

[31] Emslie A.G., Lagace R.L. Strong P.F., "Theory of the propagation of UHF radio waves in coal mine tunnels", IEEE Transactions on Antennas and Propagation, vol. AP-23, pp. 192-205, Mar. 1975

[32] Fujimori K, Arai H., "Indoor propagation characteristics including radiation pattern and polarization of base station", Proceedings of the IEEE Antennas and Propagation Society International Symposium 1997, pp.2006-2009, Montreal, Canada, July 13-18, 1997

[33] Gandhi O.P., Lazzi G., Furse C.M., "Electromagnetic absorption in the human head and neck for mobile telephones at 835 and 1900 MHz", IEEE Transactions on Microwave Theory and Techniques, vol. 44, no. 10, pp. 1884-1897, Oct. 1996

[34] Hansen R.C., " Geometric Theory of Diffraction", IEEE Press publishing, 1981, ISBN: 0-87942-150-9

[35] Hatfield M.O., "Shielding effectiveness measurements using mode-stirred chambers: A comparison of two approaches", IEEE Transactions on Electromagnetic Compatibility, vol. 30, no. 3, pp. 229-238

[36] Hatfield M.O., Freyer G.J., Bean J.L., Johnson D.M. "Repeatability of mode-stirred chamber measurements", IEEE International Symposium on Electromagnetic Compatibility, pp. 485-490, Chicago, Ill, USA, Aug. 22-26 1994

[37] Hill D.A., Ma M.T., Ondrejka A.R., Riddle B.F., Crawford M.L., Jonk R.T., "Aperture excitation of electrically large lossy cavities", IEEE Transactions on Electromagnetic Compatibility, vol. 36, no. 3, pp.169-177, Aug. 1994

[38] Hill D.A., "Electronic mode stirring for reverberation chambers", IEEE Transactions on Electromagnetic Compatibility, vol. 36, no. 4, pp. 294-299 Nov. 1994

[39] Hill D.A., "Plane wave integral representation for fields in reverberation chambers", IEEE Transactions on Electromagnetic Compatibility, vol. 40, no. 3, pp. 209-217, Aug. 1998

[40] Holloway C. L., Perini P.L., DeLyser R.R., Allen K.C., "Analysis of composite walls and their effects on short-path propagation modeling", IEEE Transactions on Vehicular Technology, vol. 46, no. 3, pp.730-738, Aug. 1997

[41] Holloway C., Cotton M.G., McKenna P., " A model for predicting the power delay profile characteristics inside a room", IEEE Transactions on Vehicular Technology vol. 48, no. 4 pp. 1110-1120, 1999

[42] Holloway C., Hill D. A., Dalke R. A., Hufford G. A., "Radio wave propagation characteristics in lossy circular waveguides such as tunnels, mine shafts and boreholes", IEEE transactions on Antennas and Propagation, vol. 48, no. 9, Sept. 2000

[43] Honcharenko W., Bertoni H. L., Dailing J.I., Qian J., Yee H.D., "Mechanism governing UHF propagation on single floors in modern office buildings", IEEE Trans. Vehicular Technology, vol. 41, no. 4, pp. 496-504 Nov. 1992

[44] Honcharenko W., Bertoni H. L., Dailing J.I., " Mechanisms governing propagation between floors in buildings", IEEE Trans. Vehicular Technology, vol. 41 pp. no. 6, pp. 787-790 Nov. 1993

[45] Hwang Y., Zhang Y.P., Kouyoumjian R.G., " Ray Optical prediction of radio-wave propagation characteristics in tunnel environments- Parts 1 & 2", IEEE Transactions on Antennas and Propagation, vol. 46, no. 9, pp.1328-1345, Sept. 1998

[46] International Electrical Commission, Medical electrical equipment, Part 1: General requirements for safety. Part 2: Collateral Standard: Electromagnetic Compatibility- Requirements and Tests. IEC 606001-1-2 1998

[47] Jakes W.M.C., "Microwave mobile communications" IEEE Press publishing, 1974, ISBN: 0-7803-1069-1

[48] Kelley I.Y., Benavides G., Bhalla R., Ling H., Vogel W.J., Foltz H.D., " Urban channel propagation modeling using the shooting and bouncing ray technique", Proceedings of the IEEE Antennas and Propagation Society International Symposium 1997, pp.2018-2021, Montreal, Canada, July 13-18, 1997

[49] Kinsler L.E., Frey A.R., Coppens, A.B., Sanders J.V., "Fundamentals of Acoustics", J.Wiley and sons Publishing, ISBN: 0-471-02933-5

[50] Kivinen J., Zhao X., Vainikainen P., "Empirical Characterization of Wideband Indoor radio channel at 5.3 GHz", IEEE Trans. Antennas and Propagation, vol. 49, no. 8, Aug. 2001

[51] Knickerbocker, G.G., Barbell A.S., "Medical device malfunction caused by electromagnetic interference: The ECRI perspective", Proceedings of a workshop on elelectromagnetics in healthcare and health, IEEE Engineering in Medicine and Biology annual meeting, pp.24-28, Montreal, Quebec, Canada 1995

[52] Lee W.C.Y., "Mobile communications engineering theory and applications 2nd edition", McGraw Hill publishing 1998, ISBN: 0-07-037103-2

[53] Liang G., Bertoni H.L., "A new approach to 3-D ray tracing for propagation prediction in cities, IEEE Transactions on Antennas and Propagation, vol. 46, no. 6, pp.853-863, June 1998

[54] Lienard M., Degauque P., "Natural wave propagation in mine environments", IEEE Transactions on Antennas and Propagation, vol. 48, no. 9, pp. 1326-1339, Sept. 2000

[55] Liu-Hinz C., Segal B., Pavlasek T., "Etimates of EMC requirements in health care environments", Proceedings of the International Symposium on Antenna Technology and Applied Electromagnetics, pp. 437-441, 1996

[56] Mazar R., Bronshein A., Lu I.T., "Theoretical analysis of UHF propagation in a city street modeled as a random multi-slit waveguide", IEEE Transaction on Antennas and Propagation, vol. 46, no.6, pp. 864-869, June 1998

[57] McNamara D.A., Pistorius C.W.I., Malherbe J.A.G., "Introduction to the uniform geometrical theory of diffraction" Artech house publishing, 1990, ISBN: 0-89006-301-X

[58] Mishra, S.R. "Analysis and design of enclosures for electromagnetic susceptibility measurements over a wide frequency range (20 MHz – 30 GHz)" PhD Thesis McGill University, Montreal Quebec, Canada, May 1982

[59] Newman E.H., "Plane multi-layer reflection code", Technical Report 712978-1, Electroscience Laboratory, Ohio State University, July 1980.

[60] Ott H.W., "Noise reduction techniques in electronic systems 2nd edition", Wiley Interscience publishing, 1988, ISBN: 0-471-85068-3

[61] Paul C.R., Nasar, S.A., "Introduction to electromagnetic fields 2nd edition", McGraw Hill publishing, 1987, ISBN: 0-07-045908-8

[62] Paul C.R., "Introduction to electromagnetic compatibility" Wiley Interscience publishing, 1992, ISBN: 0-471-54927-4

[63] Perini P.L., Holloway C.L., "Angle and space diversity comparisons in different mobile radio environments", IEEE Transactions on Antennas and Propagation , vol. 46, no.6, pp. 764-775, June1998

[64] Popov A., Zhu N. Y., "Modeling radio wave propagation in tunnels with a vectorial parabolic equation", IEEE transactions on Antennas and Propagation, vol. 48, no. 9, Sept. 2000

[65] Rappaport T. S., "Characterization of UHF multipath radio channels in factory buildings", IEEE Trans. Antennas and Propagation, vol. 37, pp. 1058-1069 Aug. 1989

[66] Rappaport T.S. "The wireless revolution", IEEE Communications Magazine, pp. 52-71, November 1991.

[67] Rappaport T.S., Milstein L.B., "Effect of radio propagation path loss on DS-CDMA cellular frequency reuse efficiency for reverse channel", IEEE Trans. Vehicular Technology Vol. 41, no. 3, pp. 231-242 Aug. 1992

[67] Rappaport T.S., " Wireless communications principles and practice", Prentice Hall publishing, 1996, ISBN: 0-13-375536-3

[68] Rice O. S., "Statistical properties of a sine wave plus random noise", Bell Systems Technical Journal, vol. 27 pp. 109-157, Jan. 1948

[69] Sabine W.C., "Collected Papers on Acoustics", Harvard University Press 1922

[70] Schuster J.W., Luebbers R.J., "Comparison of GTD and FDTD predictions for UHF radio wave propagation in a simple outdoor urban environment", Proceedings of the IEEE Antennas and Propagation Society International Symposium 1997, pp.2022-2025, Montreal, Canada, July 13-18, 1997

[71] Seidel S. Y., Rappaport T. S., "914 MHz path-loss prediction models for indoor wireless communications in multi-floored buildings" IEEE Transactions on Antennas and Propagation, vol. 40, no. 2, pp. 207-217, Feb. 1992

[72] Seidel S. Y., Rappaport T.S., " Site-specific propagation prediction for wireless in-building personal communication system design", IEEE Trans. Vehicular Technology, vol. 43, pp. 879-891, Nov. 1994

[73] Segal B., Retfalvi S., Townsend S., Pavlasek T.J.F., "Recommendations for electromagnetic compatibility in health care", Proceedings Canadian Medical and Biological Engineering Society 1996 conference, Charlottetown, PEI, Canada, June 27, 1996

[74] Segal B., Retflavi S., Townsend D., Tan K.S., "A workshop on electromagnetic compatibility in health care and cardiac pacemakers", Workshop sponsored by Canadian Wireless Telecommunication Association for Administrators, Risk Managers, Biomedical Engineering personnel and Health Professionals, Montreal, Quebec, Canada, Jan. 30 1997

[75] Segal B., Davis D., Pavlasek T.J.F., " Hospital electromagnetic compatibility: Needs, recommendations and implementation", Invited presentation: Proceedings of the 26th General Assembly of the International Union of Radio Science, p. 870, Toronto, Ontario, Canada, Aug. 20 1999

[76] Segal B., Davis D., Trueman C.W.T., Pavlasek, T.J.F., "Risk of patient injury due to electromagnetic-interference malfunctions: Estimation and minimization", Peer reviewed special session organized and chaired by B. Segal, 90 page, IEEE International Symposium on Electromagnetic Compatibility, Montreal, Quebec, Canada, Aug. 2001

[77] Shaw A., "New wireless systems speed up access to clinical information and boost patient care", Canadian Healthcare Technology, vol. 6, no. 3, pp.18-23, April 2001.

[78] Silverberg J., "Performance degradation of electronic medical devices due to EMI", Compliance Engineering, vol. 10 pp.25-39, 1993

[79] Sklar B., "Rayleigh fading channels in mobile digital communication systems parts 1: & 2", IEEE Communications Magazine, pp. 136-155, September 1997

[80] Skomal E.N., Smith A.A., "Measuring the radio frequency environment", Van Nostrand Reinhold Company, ISBN: 0-442-28184-6

[81] Tan K.S., Hinberg I., "Investigation of electromagnetic interference with medical devices in Canadian hospitals", Proceedings of a workshop on electromagnetics in healthcare and health, IEEE Engineering in Medicine and Biology annual meeting, pp.20-23, Montreal, Quebec, Canada 1995

[82] Tang Y., Sobol H., "Measurements of PCS microwave propagation in buildings", Applied Microwave and Wireless, pp.38-60, winter 1995

[83] Talbi L., Delisle G.Y., "Measurement results of indoor radio channel at 37.2 GHz", Proceedings of ANTEM94: Symposium on Antenna Technology and Applied Electromagnetics 1994 Conference Proceedings, Ottawa, Canada, pp. 19-23, Aug. 3-5 1994

[84] Torrico S.A., Bertoni H.L., Lang R.H., "Modeling tree effects on path loss in a residential environment", IEEE Transactions on Antennas and Propagation, vol. 46, no. 6, pp.872-879, June 1998

[85] Townsend D. A., " Risk analysis and EMI risk abatement strategies for hospitals: Scientific and legal approaches", Proceedings of the IEEE International Symposium on Electromagnetic Compatibility, Montreal, Quebec, Canada, Aug. 2001, pp. 1304-1307

[86] Trueman C.W.T., Paknys R., Zhao J., Davis D., Segal B., "Ray tracing algorithm for indoor propagation", Proceedings of 16th Annual Review of Progress in Applied

Computational Electromagnetics Society, pp. 493-500, Monterey, California, USA, March 20-24 2000

[87] Trueman, C.W.T., Davis D., Segal B., "Specifying zones for cellular telephone operating in hospital hallways", ANTEM 2000 Proceedings of Symposium on Antenna Technology and Applied Electromagnetics, pp. 381-386, Winnipeg, Man., Canada, July 30-Aug. 2, 2000

[88] Trueman C.W.T. Davis D., Segal B., "Ray optical simulation of indoor corridor propagation at 850 and 1900 MHz", Proceedings of the IEEE Conference on Antennas and Propagation for Wireless Communications, pp. 81-84, Waltham, Mass., USA, Nov.6-8, 2000

[89] Vlach P., Segal B., Lebel J., Pavlasek T.J.F., "Cross-floor signal propagation inside a contemporary ferro-concrete building at 434, 862 and 1705 MHz", IEEE Transactions on Antennas and Propagation, vol. 47, no.7, pp.1230-1232 July 1999

[90] Walfisch J., Bertoni H.L., "A theoretical model of UHF propagation in urban environments", IEEE Transactions on Antennas and Propagation, vol. 36, no. 12, pp. 1788-1796, Dec. 1989

[91] Xia H., Bertoni H.L., Maciel L.R., Lindsay-Stewart A., Rowe R., "Radio propagation characteristics for line of sight microcellular and personal communications" IEEE Trans. On Antennas and Propagation, Vol. 41, No. 10, October 1993, pp. 1439-1447

[91] Zhang W.X, Yun Z.Q., Tsang K.F., "Path loss characteristics in the OOS regions of urban microcellular environments", Proceedings of the IEEE Antennas and Propagation Society International Symposium 1997, pp.2002-2005, Montreal, Canada, July 13-18, 1997

[92] Zhang Y.P., Zheng G. X., Sheng J.H., "Radio propagation at 900 MHz in underground coal mines", IEEE Transactions on Antennas and Propagation, vol. 49, no. 5, pp. 757-762, May 2001

[93] Kohn L. T., "To Err is human", National Academy Press, ISBN: 0-309-06837-1